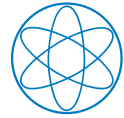


Chair of Molecular Nanoscience  
& Chemical Physics of Interfaces (E20)  
Department of Physics  
Technical University of Munich



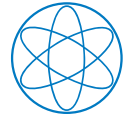
Technische Universität München

Atomistic Investigations and Control of Novel Quantum  
Materials: Lanthanide-Organic Nano-Architectures at  
Well-Defined Substrates and the Iron Silicide (110)  
Facet

Martin Uphoff

PhD Thesis  
July 2019





Technische Universität München

# Atomistic Investigations and Control of Novel Quantum Materials: Lanthanide-Organic Nano-Architectures at Well-Defined Substrates and the Iron Silicide (110) Facet

Martin Uphoff

Vollständiger Abdruck der von der Fakultät für Physik der Technischen Universität  
München zur Erlangung des akademischen Grades eines

**Doktors der Naturwissenschaften (Dr. rer. nat.)**

genehmigten Dissertation.

Vorsitzender: Prof. Dr. Frank Pollmann

Prüfer der Dissertation: 1. Prof. Dr. Joahannes Barth

2. Prof. Dr. Christian Back

Die Dissertation wurde am 04.07.2019 bei der Technischen Universität München  
eingereicht und durch die Fakultät für Physik am 16.07.2019 angenommen.



# Abstract

This thesis presents an atomistic study of novel quantum materials by means of scanning tunneling microscopy and spectroscopy. The experiments are accompanied by complementary X-ray photoelectron and low-energy electron diffraction experiments, as well as *ab initio* density functional theory calculations. By utilizing holmium and carboxylate linker species, surface supported lanthanide coordinated metal-organic structures on Ag(100) and MgO/Ag(100) are fabricated *via* bottom-up approach. With the aid of computational modeling efforts structural features are rationalized. Furthermore, we succeeded in preparing a well-defined FeSi(110) surface. We find an electronic state inside the narrow band-gap accompanied by an unusually small width and asymmetric shape of the gap compared to bulk measurements. By means of density functional theory calculations new insights to the surface termination and relaxation are given.



# Zusammenfassung

Die vorliegende Dissertation stellt eine Studie neuer Quantenmaterialien auf atomarer Ebene mittels Rastertunnelmikroskopie und Rastertunnelspektroskopie dar. Die Experimente werden von komplementären Messungen durch Röntgenphotoelektronenspektroskopie und der Beugung langsamer Elektronen sowie von *Ab-initio* Rechnungen mittels Dichtefunktionaltheorie begleitet. Durch die Verwendung von Holmium und Carboxylaten als molekulare Verbindungbausteine werden oberflächengestützte metallorganische Strukturen auf Ag(100) und MgO/Ag(100) mittels Bottom-up Synthese hergestellt. Mithilfe von rechengestützter Modellierung werden strukturelle Details offen gelegt. Außerdem gelingt die Präparation einer wohldefinierten FeSi(110) Oberfläche. Wir finden einen elektronischen Zustands innerhalb der schmalen Bandlücke, sowie eine ungewöhnlich kleine und asymmetrische Bandlücke im Vergleich zu früheren Messungen im Festkörper. Mittels Dichtefunktionaltheorierechnungen werden entscheidene Hinweise zur Oberflächenterminierung und -relaxation geliefert.





# Contents

<b>Abstract</b>	<b>I</b>
<b>Zusammenfassung</b>	<b>III</b>
<b>Contents</b>	<b>V</b>
<b>1. Introduction</b>	<b>1</b>
<b>2. Experimental Methods</b>	<b>7</b>
2.1. Scanning Tunneling Microscopy . . . . .	9
2.1.1. Fundamental Theory . . . . .	10
2.1.2. The Tersoff-Hamann Model . . . . .	12
2.1.3. Scanning Tunneling Spectroscopy . . . . .	13
2.2. Low Energy Electron Diffraction . . . . .	17
<b>3. Instrumentation</b>	<b>21</b>
3.1. UHV Chamber . . . . .	23
3.2. Joule-Thomson Scanning Tunneling Microscope . . . . .	24
<b>4. Holmium-Directed 2D Metal-Organic Coordination on Ag(100)</b>	<b>27</b>
4.1. Introduction . . . . .	29
4.2. Results and Discussion . . . . .	30
4.2.1. Ho-directed assembly . . . . .	33
4.2.2. DFT analysis of Ho-TPA networks . . . . .	40
4.3. Conclusions . . . . .	43
<b>5. TPA-Ho Complexes on MgO/Ag(100)</b>	<b>45</b>
5.1. Introduction . . . . .	47
5.2. Results and Discussion . . . . .	47
5.2.1. Magnesium Oxide Growth on Ag(100) . . . . .	47

5.2.2.	TPA Deposition on Ag(100)/MgO . . . . .	52
5.2.3.	Ho-TPA complexes on Ag(100)/MgO . . . . .	56
5.3.	Conclusions . . . . .	60
<b>6.</b>	<b>Structural and Electronic Properties of the FeSi(110) Surface</b>	<b>63</b>
6.1.	Introduction . . . . .	65
6.2.	The B20 crystal structure . . . . .	66
6.3.	FeSi(110) surface . . . . .	68
6.3.1.	STM measurements . . . . .	68
6.3.2.	DFT calculations . . . . .	75
6.4.	Scanning tunneling spectroscopy investigation of FeSi(110) . . . . .	81
6.4.1.	Tip characterization on Ag(111) . . . . .	81
6.4.2.	Pseudo-gap and in-gap state . . . . .	82
6.5.	Conclusions . . . . .	87
<b>7.</b>	<b>Conclusions and Outlook</b>	<b>89</b>
<b>A.</b>	<b>TPA-Ho on Ag(110)</b>	<b>95</b>
A.1.	Organic transition phase . . . . .	97
A.2.	Chirality of Ho-TPA <sub>4</sub> complexes . . . . .	97
A.3.	Ho-evaporator . . . . .	97
A.4.	Holmium coverage definition . . . . .	99
A.5.	Drift correction . . . . .	99
A.6.	Determination of the U-value . . . . .	99
A.7.	Structural relaxation details . . . . .	99
A.8.	Node bonding environment . . . . .	100
<b>B.</b>	<b>TPA-Ho on MgO/Ag(110)</b>	<b>103</b>
B.1.	Single monolayer of MgO . . . . .	105
<b>C.</b>	<b>FeSi</b>	<b>107</b>
C.1.	Additional STM data . . . . .	109
C.2.	XPS . . . . .	111
C.3.	Structural models . . . . .	113
	<b>Bibliography</b>	<b>117</b>

<b>List of Publications</b>	<b>143</b>
<b>Acknowledgements</b>	<b>145</b>



# 1



## Introduction



---

In the late 1960s, condensed matter physics evolved the new scientific field of surface science emerging from the confluence of three factors: ultra-high vacuum technology, the ability to grow single crystals and make them commercially available and the new insights to the interaction of electrons with solids [1]. Different electron spectroscopic techniques were widely used to investigate surfaces under controlled conditions. Taniguchi and Drexler later followed with introducing the probably more famous name "Nano-Technology" and defined it as the manipulation of individual atoms and molecules [2, 3]. Though the two terms are not describing identical fields of research, they always shared a big overlap. While the early days of surface science were limited to spectroscopy and diffraction experiments, a crucial milestone was achieved in 1982 [4]: The invention of the scanning tunneling microscope (STM) by Binnig and Rohrer [5] enabled the imaging of individual molecules and atoms on surfaces. Additional sensing and manipulation power was gained by the subsequent development of the atomic force microscope in 1986 [6].

In 1965 Moore had stated his prediction that the circuit density in electronics would double every two years [7]. His hypothesis was indisputable for a long time, for history proved him right. Surface and nano science were always strongly correlated to the revolution of microelectronics. The new technologies enabled scientists to conduct complex experiments and findings in nano science influenced the evolution of electronics [1]. For the past decades, and up to now, classical top-down engineered semiconductor electronics govern the world of information technology. However, currently the miniaturization of top-down fabricated integrated circuits seems to approach its limits [8] and the extensive possibilities offered by modern surface and nano science techniques return to the limelight of modern technology. The search for new quantum materials is one of the major challenges in modern condensed matter physics and influential in nano science [9]. Although fundamental research on model systems is the focus of most nanoscale science investigations, there are plenty of applications that already made it into production, *e.g.* organic light emitting diodes [10] or organic solar cells [11]. Especially considering the issue of down-scaling of electronic devices, the engineering of quantum materials is requested more than ever.

In general, applications for these materials can be found in the fields of catalysis [12–18], energy technology [19, 20], light emission [10, 21, 22], chemical sensors [23, 24] and molecular electronics [25, 26]. Here, the major steps in molecular nanotechnology and the fabrication of nano materials have been the manipulation of individual atoms [27] and the fabrication of carbon nano-architectures, such as bucky balls [28] and carbon nanotubes

## 1. Introduction

---

[29]. Specifically in the context of surface science, numerous approaches were conducted in the bottom-up fabrication of molecular architectures on surfaces [30, 31] as well as the surface-supported fabrication of 2D materials, such as graphene [32], h-BN [33] and their applications [34] and derivatives, *e.g.* graphene nanoribbons [35] or graphdiyne nanowires [36], representing major steps in the field of band structure engineering.

The general concept of molecular engineering on surfaces is to utilize specifically designed molecular building blocks on atomically well-defined surfaces to build molecular nano- architectures via self-assembly and surface assisted reactions. To ensure a well defined, contamination free environment, corresponding experiments are usually carried out under ultra-high vacuum conditions. For the formation of structures *via* self-assembly on surfaces, a variety of different interactions, such as van der Waals interaction, H-bonding and metal-ligand interactions have to be taken into account [37]. In recent years, especially the incorporation of lanthanides into metal-organic nano-architectures gained substantial interest in the community. Motivated by the special coordination capabilities of lanthanides with their high coordination numbers [38] and taking into account their exceptional magnetic properties they are highly relevant for molecular magnetic devices and spintronics [39–41]. The fabrication of single-molecule magnetic complexes involving lanthanides was achieved [42] and 4f elements were incorporated into interfacial nano-architectures [43].

Recently, evidence was given that holmium atoms can serve as single atom magnets on surfaces, rendering the ultimate smallest magnetic memory unit [44]. A crucial point for the magnetic properties of such single atoms on surfaces is the chemical environment, which can either be tuned by organic ligands [45] or by the introduction of an insulating decoupling layer [44]. The high surface mobility of the single atoms on the surface, however, is a major issue and results in clustering at low and ambient temperatures.

Another promising approach to novel pathways for interfacial quantum materials is the field of topological insulators (TI) and related materials, such as heavy fermion systems [46] and Kondo insulators [47]. They offer a wide range of applications, *e.g.* in photo detectors, magnetic devices, field-effect transistors and lasers [48]. In particular, the (110) surface of the putative Kondo insulator iron silicide (FeSi) [49] showed a highly unusual conductivity behavior and may offer undiscovered conduction channels exclusively present on the surface [50]. However, in-depth studies of the surface structure and the electronic properties of this system are still lacking at the current stage.

The outline of the presented thesis is as follows: In chapter 2 the physical background of the experimental techniques is briefly addressed, followed by a short presentation of the



---

used instrumentation in chapter 3. Chapter 4 presents the STM based study of holmium-based metal-organic compounds and networks on the Ag(100) surface, which overcomes the diffusion problems of single holmium atoms mentioned above. Structural models have been developed by *ab initio* density functional theory calculations (DFT), as well as models for the charge transfer mechanisms to the surface. As already stated by Donati *et al.*, the exceptional magnetic properties become accessible by the introduction of an insulating decoupling layer, namely MgO [44]. Hence, as a consecutive goal similar nano-architectures are employed on layers of MgO on Ag(100), addressed as a proof of principle study in chapter 5. Detailed information on the growth of MgO on Ag(100), as well as the formation of metal-organic structures on this substrate is reported.

While chapters 4 and 5 deal with the synthesis of metal-organic structures on surfaces, chapter 6 provides new insight to the structural and electronic properties of the FeSi(110) surface. Inspired by the intriguing results from Wagner *et al.* [50], we investigated the structural and electronic properties of the surface by means of STM and scanning tunneling spectroscopy (STS) measurements, as well as DFT calculations. The preparation of a well-defined (110) surface is reported and spectroscopic insight to the electronic structure is given. The studies are supported by low-energy electron diffraction (LEED) and X-ray photoelectron spectroscopy (XPS) measurements. Finally, a summary of the thesis and an outlook to future research projects on the discussed topics are given in chapter 7.



# 2

## Experimental Methods



The development of scanning probe microscopy (SPM) made exceptional additions to the experimental techniques of surface science. Before, the insight to interfacial systems on the nanoscale was mostly limited to methods in the fields of spectroscopy and diffraction experiments, which integrate over a large area of the sample. Though semi-atomic resolution measurements with field ion microscopy [51] and transmission electron microscopy [52] were achieved before, SPM offers real space information down to the atomic scale. The start of SPM was the invention of the scanning tunneling microscope (STM) by Binnig and Rohrer in 1981 [5]. They produced a series of astonishing results, from the imaging of monoatomic steps [53] to resolving the Si( $7 \times 7$ ) reconstruction [54], finally receiving the Nobel Prize in physics in 1986. The STM was followed by series of other techniques, such as the scanning nearfield optical microscope (SNOM) [55], the atomic force microscope (AFM) [6] and numerous derivatives of these. They all share the basic idea of a microscopic probe (often simply called tip) that is being utilized to confine the investigated interaction between probe and sample to a very small space. In the case of STM and AFM this can be down to the subatomic scale. Because the information can only be recorded for a specific point at a time, the probe is moved along a grid of data points and scanning the sample. This results in a 2D matrix of data points, hence the term scanning probe microscopy.

## 2.1. Scanning Tunneling Microscopy

The STM uses the quantum mechanical tunneling effect. Initially, the phenomenon was theoretically derived to explain the processes in the  $\alpha$ -decay of nuclei [56], later experimentally observed for planar tunneling junctions in 1930 [57] and in 1960 for superconducting metals separated by an insulating film [58]. While field emission into the vacuum was already explained in 1928 [59], Binnig and Rohrer in 1982 showed tunneling through a controlled vacuum gap [5].

When two conducting electrodes are brought closely together and a voltage is applied between them, a current can be measured. In the case of STM, the two electrodes consist of an atomically sharp tip and a rather flat sample, which are both conducting. The tip can be moved with a piezo tube in x-, y- and z-direction. It is scanned along the surface (x- and y-direction) in either constant height or constant current mode. The latter is more widely used and incorporates a feedback loop that will keep the tunneling current constant. The z-displacement of the tip is recorded, producing a three dimensional image of the surface.

## 2. Experimental Methods

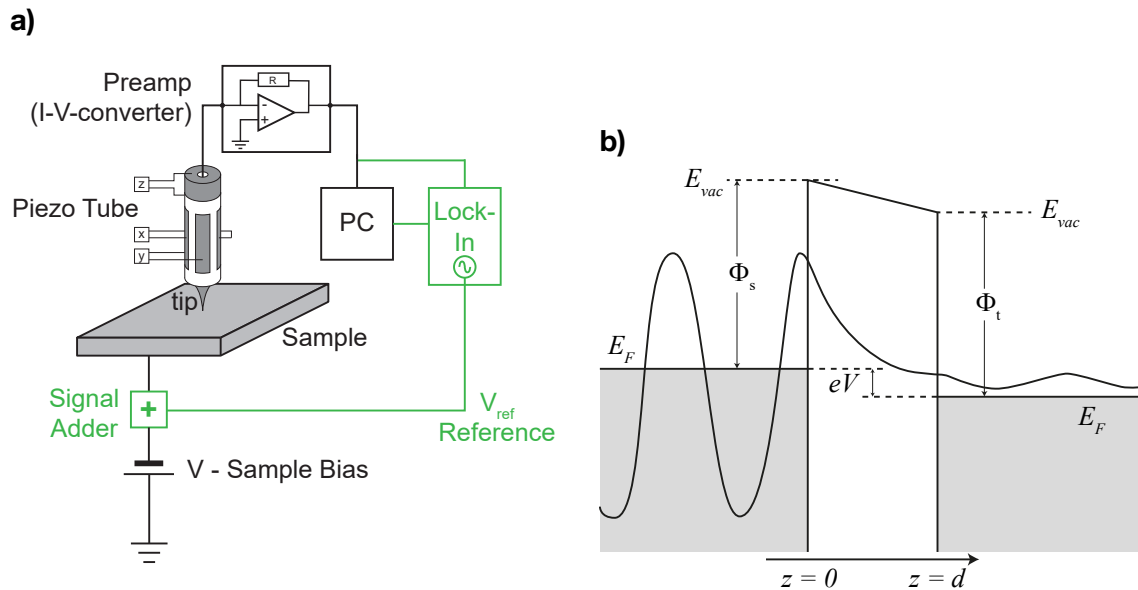


**Figure 2.1.:** **a)** STM setup, the green components are only used in STS (see section 2.1.3) **b)** Schematic sketch of energies and wave functions when tunneling through a vacuum gap (adapted from ref. [60]). The applied voltage causes a shift in energy levels of tip and sample. For simplicity, the special case of identical work for tip and sample is shown. Though classically forbidden, the particle can penetrate the barrier and tunnel through it. While tunneling through the gap, the amplitude of the corresponding wave function decays exponentially and travels on after the gap with decreased amplitude.

Figure 2.1a shows the basic components of a typical STM setup.

### 2.1.1. Fundamental Theory

The sketch in Figure 2.1b shows the situation for a simplified one dimensional tunneling barrier. Although the vacuum gap between the two electrodes classically forbids this, the electrons will tunnel through the potential barrier. Quantum mechanics predict that a particle (described as a traveling wave) can travel through a potential barrier, even when it classically would not. This effect is based on the boundary conditions for the probability density which states that a traveling wave can not fall off to zero instantaneously (disregarding the case of an infinite high potential barrier). Therefore, the probability density decays exponentially while the wave travels through the gap and after the barrier travels on with decreased amplitude. There will be tunneling in both directions, but the applied voltage will make one direction much more probable than the other.

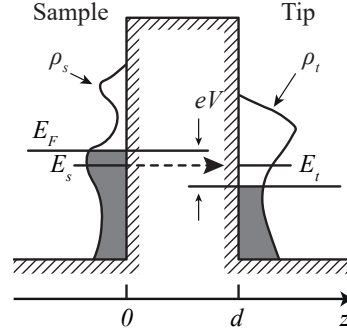


**Figure 2.2.:** Density of states of tip and sample as modelled in the Bardeen approach to tunneling theory (adapted from ref. [60]). The Schrödinger equations are solved independently for tip and sample and linked by introducing a transfer Hamiltonian. The line linking  $E_s$  and  $E_t$  indicates that tunneling is only allowed between states of equal energy. Grey surfaces indicate occupied states.

Quantum mechanically, we can describe the system in a simplified one dimensional model, with different solutions for the Schrödinger equation in front of, inside and behind the barrier. From elemental quantum mechanics and by appliance of the Wentzel-Kramers-Brillouin approximation we can deduce the transmission coefficient [61]:

$$T = \exp \left[ -2 \int_{z_1}^{z_2} \kappa(z) dz \right], \quad (1)$$

where  $\kappa$  is the decay constant inside the classically forbidden region:

$$\kappa(z) = \frac{\sqrt{2m(U(z) - E)}}{\hbar}. \quad (2)$$

$U(z)$  is the potential height of the barrier and  $E$  is the energy of the electron. When a voltage is applied to the sample, the Fermi level shifts by  $eV$ , as depicted in Figure 2.1b. This will make tunneling from the sample to the tip much more probable and hence results in a net current from sample to tip. By reversing the voltage, the tunneling direction can be reversed. The case in Figure 2.1b represents electrons tunneling from the sample to the tip. Here, the transmission coefficient becomes:

$$T(E) = \exp \left[ -\frac{2}{\hbar} \sqrt{m(\Phi_s + \Phi_t - eV)} \cdot d \right] \quad (3)$$

## 2. Experimental Methods

---

Equation 3 clearly shows that the tunneling current is exponentially connected to the barrier width  $d$ , which is the reason for the high effectiveness of the feedback loop in STM. Tunneling always occurs from an occupied state of one electrode to an unoccupied state of the other of equal energy. Therefore, the tunneling current strongly depends on the local density of states (LDOS) of tip and sample (see Figure 2.2). Introducing the concept of a transfer Hamiltonian and describing the system with separate wave functions for tip and sample, Bardeen deduced [62] that the tunneling current equals [60]:

$$I = \frac{4\pi e}{\hbar} \int_{-\infty}^{\infty} [f(E_F - eV + \epsilon) - f(E_F + \epsilon)] \times \rho_s(E_F - eV + \epsilon)\rho_t(E_F + \epsilon)|M|^2 d\epsilon. \quad (4)$$

Here, the first term of the integral is the Fermi distribution function, accounting for the thermal broadening of occupied and unoccupied states around the Fermi level at higher temperatures. For simplicity and because this work focuses on low temperature measurements we can neglect this in first approximation. By specifying the energy interval with the bias voltage  $V$  we get

$$I = \frac{4\pi e}{\hbar} \int_0^{eV} \rho_s(E_F - eV + \epsilon)\rho_t(E_F + \epsilon)|M|^2 d\epsilon, \quad (5)$$

where  $\rho_s$  and  $\rho_t$  are the LDOS of sample and tip, respectively.  $|M|$  is the tunneling matrix element, which is however, generally unknown. Since only states close to the Fermi level are of interest, Bardeen assumed that  $|M|$  does not change significantly around the Fermi level and can be treated as a constant. Then, the tunneling current is proportional to the convolution of the density of states of tip and sample:

$$I \propto \int_0^{eV} \rho_s(E_F - eV + \epsilon)\rho_t(E_F + \epsilon) d\epsilon. \quad (6)$$

This equation and the fundamental meaning of it are important, when interpreting STM images: The measured tunneling current is not only giving information of the electronic structure of the sample, but also of the tip.

### 2.1.2. The Tersoff-Hamann Model

Tersoff and Hamann [63, 64] developed a simple model to overcome the problem of an unknown LDOS of the tip and the unknown tunneling matrix element. They assumed the



tip to have a spherical apex of a defined radius, hence modeling it as an atomically sharp tip with a single atom at the apex. This modeling is *de facto* assuming s-orbitals for the tip. The tunneling matrix element in the Tersoff-Hamann model is

$$M_{ts} = \frac{2\pi\hbar}{m} \sqrt{\Omega_t} R e^{\kappa R} \psi_s(\vec{r}_0). \quad (7)$$

Here,  $\Omega_t$  is the probe volume (*i.e.* the tip),  $R$  is the curvature radius of the apex,  $\kappa$  the decay constant from equation 2,  $\psi_s$  is the wavefunction of the state from or where to the electron tunnels and  $r_0$  denotes the position of the apex center. Because the model treats the LDOS of the tip as a constant, sets the temperature of the junction to zero and disregards inelastic tunneling, we can put this expression into equation 5 and get an analytic expression for the tunneling current, only depending on the density of states of sample and the decay constant discussed above (equation 2). By applying this to equation 6 and again applying the principle of density of states rather than discrete individual wave function we get

$$I = \frac{32\pi^3 e^2 V \phi^2(E_F) R^2 e^{2\kappa R}}{\hbar \kappa^4} \rho_t \int_0^{eV} \rho_s(\epsilon) d\epsilon. \quad (8)$$

Though it is a very simplified interpretation of the electronic structure of the tip, the model has proven to be very valuable for the interpretation of STM images and is also used for the simulation of STM data in this work.

### 2.1.3. Scanning Tunneling Spectroscopy

As discussed above, the STM can be used to scan the sample and probe the electronic structure and thereby give insight to the topography. Another very useful operational mode is scanning tunneling spectroscopy (STS), which can be used to investigate the LDOS of the sample. Selloni *et al.* were the first to propose the use of STM to probe the LDOS of the sample being especially sensitive to surface states [65], rather than bulk electronic states. The first measurements were taken by Binnig *et al.* on Ni(100) [66]. Ever since, STS has widely been used in surface science to probe the energy landscape around the Fermi level on metal surfaces [67–69] and molecular architectures [70–73]. Furthermore, the investigation of vibrational modes via inelastic tunneling spectroscopy (IETS, partly used before the invention of SPM) [74–77] and even spin sensitive measurements giving insight into the magnetic properties of the sample system were achieved [44, 78–80].

Typically for STS, the tip is approached to the sample and held at a constant height and

## 2. Experimental Methods

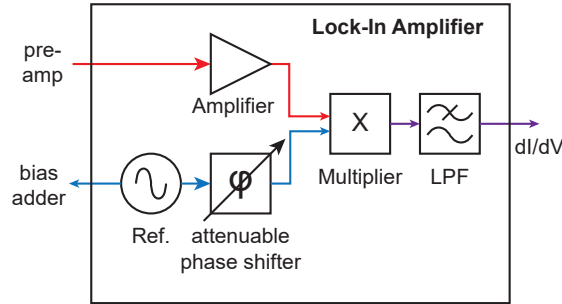


**Figure 2.3.:** Basic principle of a lock-in amplifier used in STS.

the bias voltage is ramped. Assuming the temperature of the tunneling junction is still (very near to) zero, we can again neglect the Fermi distribution of states and equation 6 is still valid. Taking the LDOS of the tip as a constant (which is fairly realistic for a metal tip around  $E_F$ ), the derivative of the tunneling current gives:

$$\frac{\partial I}{\partial V} \propto \rho_t \rho_s (eV). \quad (9)$$

Equation 9 shows that the derivative of the tunneling signal  $I(V)$  is directly proportional to the density of states of the tip and can be used to determine the LDOS of the sample around  $E_F$ . Taking the numerical derivative is possible (and sometimes done), though it involves a lot of noise in the final spectra and is therefore seldom the method of choice. Much cleaner spectra can be obtained by using a lock-in amplifier, which will be briefly discussed in the following.

### STS using a lock-in amplifier

As mentioned before, numerical derivatives of tunneling signals feature very high noise. To overcome this, a lock-in amplifier is used. The incorporation of the lock-in amplifier to the STM setup is shown in Figure 2.1a (green components). The bias voltage is modulated by a small AC voltage  $V_{ref}$  of a specific frequency  $\omega_m$  and amplitude  $V_m$ . This results in a modulation of the tunneling signal  $I_T$ . Note that though the signal of interest is the tunneling current signal, it is actually a voltage signal that is passed into the lock-in amplifier, because the preamplifier converts the current into a corresponding voltage. The lock-in amplifier will only detect signals corresponding to the modulation frequency and of specific phase, acting as a very narrow width band-pass filter. The basic operational

principle is schematically shown in Figure 2.3. The lock-in amplifiers core elements are the multiplier and the low-pass filter. First, the signal is amplified and then multiplied with the reference signal  $V_{ref}$ . Afterwards, the signal is passed through a low-pass filter with a much smaller cut-off frequency than  $\omega_m$ . This produces the first derivative of the original signal. The derivation below was partly printed elsewhere [81].

From equation 8 we know that

$$I_T \propto \int_0^{eV + eV_m \sin(\omega_m t)} \rho_s(\epsilon) d\epsilon \quad (10)$$

This expression can be expanded into a Taylor series around the point of energy  $eV$ , whereas the new variable of the Taylor expression will be  $[eV + eV_m \sin(\omega_m t)]$ :

$$\begin{aligned} I_T \propto & \int_0^{\overbrace{eV + eV_m \sin(\omega_m t)}^{\approx eV}} \rho_s(\epsilon) d\epsilon + \underbrace{\rho_s(eV + eV_m \sin(\omega_m t))}_{\approx \rho_s(eV)} eV_m \sin(\omega_m t) \\ & + \underbrace{\rho'_s(eV + eV_m \sin(\omega_m t))}_{\approx \rho'_s(eV)} \frac{e^2 V_m^2 \sin^2(\omega_m t)}{2} + \dots \end{aligned} \quad (11)$$

Because the modulation amplitude  $V_m$  is small against the DC bias  $V$ , we can make the simplifications as indicated by the braces above:

$$I_t \propto \underbrace{\int_0^{eV} \rho_s d\epsilon}_{\propto I_t(V)} + \underbrace{\rho_s(eV) eV_m \sin(\omega t)}_{\propto I'_t(V)} + \underbrace{\rho'_s(eV) \frac{e^2 V_m^2 \sin(\omega t)}{2}}_{\propto I''_t(V)} + \dots \quad (12)$$

The multiplier of the lock-in amplifier will now form the product  $V_{mult}$  of this signal  $V_S$  and the internal reference  $V_{ref,int}$ . Also, the signal contains noise  $V_N$ , which in this case will be modeled as ideally white.

$$\begin{aligned} V_{mult} &= V_{ref,int} \times (V_S + V_N) \\ &= \sin(\omega_m t + \varphi) \end{aligned} \quad (13)$$

$$\times \left( \int_0^{eV} \rho_s(\epsilon) d\epsilon + \rho_s(eV) eV_m \sin(\omega_m t + \varphi_0) + \dots + \int_{-\infty}^{\infty} a_\omega \sin(\omega t) d\omega \right) \quad (14)$$

## 2. Experimental Methods

---

The adjustable phase shifter of the lock-in introduces a phase shift  $\varphi$  of the reference, while the tunneling signal will pick up an intrinsic phase shift of  $\varphi_0$ . All terms (including the noise) but the second of equation 12 will be proportional to an oscillating part of frequency  $\omega_m$  and its higher harmonics. Therefore, we can write

$$V_{mult} = \frac{\rho_s e V_m}{2} [\cos(\varphi - \varphi_0) - \cos(2\omega_m t + \varphi + \varphi_0)] + \sin(\omega_m t) \times \dots \quad (15)$$

The lowpass filter of the lock-in will reject all the oscillating parts, leaving us with an output of

$$V_{out} = \frac{\rho_s e V_m}{2} \cos(\varphi - \varphi_0). \quad (16)$$

By choosing a suitable phase  $\varphi$ , the signal can be maximized and is directly proportional to the first derivative and hence, the LDOS of the sample. Simultaneously the noise is rejected. Lock-in amplifiers can also give higher derivatives of the signal (*e.g.* for inelastic tunneling spectroscopy [74] (IETS), simply by multiplying it with higher harmonics of the reference.

### Other Sources of Noise

The assumptions above infer a temperature of 0 K, but in real experiments even a very small temperature has a non-neglectable influence on the energy resolution due to thermal broadening of the LDOS around  $E_F$ . If we take equation 4, but still assume a constant  $|M|$ , taking the derivative of the tunneling signal becomes more complicated. It then involves a convolution of the LDOS of the sample with the derivative of the Fermi function, which has the form of a  $\text{sech}^2(x)$ . For practical purposes it is sufficient to know that the thermal broadening function has a full width half maximum (FWHM) of  $3.2k_B T$  [74]. For the experiments in this work, the temperature was either 4.6 K or 1.15 K. This results in a thermal outsmearing of the states of 1.3 meV and 0.3 meV, respectively.

Another source of noise is the capacitance between tip and sample, when the bias voltage is modulated, as in STS. The tip-sample system acts as a capacitor that is connected in parallel to the tunneling junction (which can be treated ohmic). The capacitive signal has a phase shift by  $90^\circ$  to the actual tunneling signal. The usage of a lock-in amplifier enables us to lock onto the capacitive signal and then rotate the phase by  $90^\circ$ . This allows one to only detect the signal of the tunneling junction.

When using the lock-in technique, the modulation amplitude also influences the energy resolution[74]. Obviously, the higher the modulation amplitude, the higher the energy window recorded is. This is oftentimes called the instrumental function and amounts to[82]

$$\chi_m = \begin{cases} \frac{2\sqrt{V_m^2 - V^2}}{\pi V_m^2} & \text{for } |V| \leq V_m, \\ 0 & \text{for } |V| > V_m \end{cases}. \quad (17)$$

The FWHM of this function is  $1.7 V_m$ . While increasing the modulation amplitude increases the signal to noise ratio, it simultaneously lowers the resolution. Therefore, successful spectroscopy of small energy features always entail a well-considered modulation voltage. The electronic components of the measurement system (*e.g.* pre-amp) will also induce noise to the measurement and mechanic vibrations from the vacuum chamber are omnipresent and have to be reduced to a minimum.

## 2.2. Low Energy Electron Diffraction

Low energy electron diffraction (LEED) is a widely used diffraction method for structural surface analysis. In 1927 the first diffraction experiments with electrons of low energy were conducted by Davisson *et al.* [83, 84] and Thomson *et al.* [85]. Though the technique was not called "LEED" by that time, the experiments showed the wave character of electrons, as predicted by de Broglie in 1924 [86]. Because metal surfaces of high periodicity and suitable vacuum chambers became available much later, LEED encountered a renaissance in the 1960s. Since LEED is only used as a cross-reference in this work for the *in situ* treatment of the crystal, the following description will only focus on the basic operation principles.

It utilizes the scattering of electrons by the periodic lattice of the surface as well as superstructures, such as molecular assemblies. A typical LEED setup is shown in Figure 2.4a. Electrons are accelerated by an electron gun, consisting of cathode, anode and ion optics. After hitting the sample, electrons will be scattered back and form a diffraction pattern on a fluorescent screen. To make sure that only electrons coming from elastic scattering events will reach the screen, grids are mounted in front of the screen to repel electrons of lower energy. After passing the last grid, they are accelerated by a high voltage applied to the screen to produce visible fluorescence.

## 2. Experimental Methods

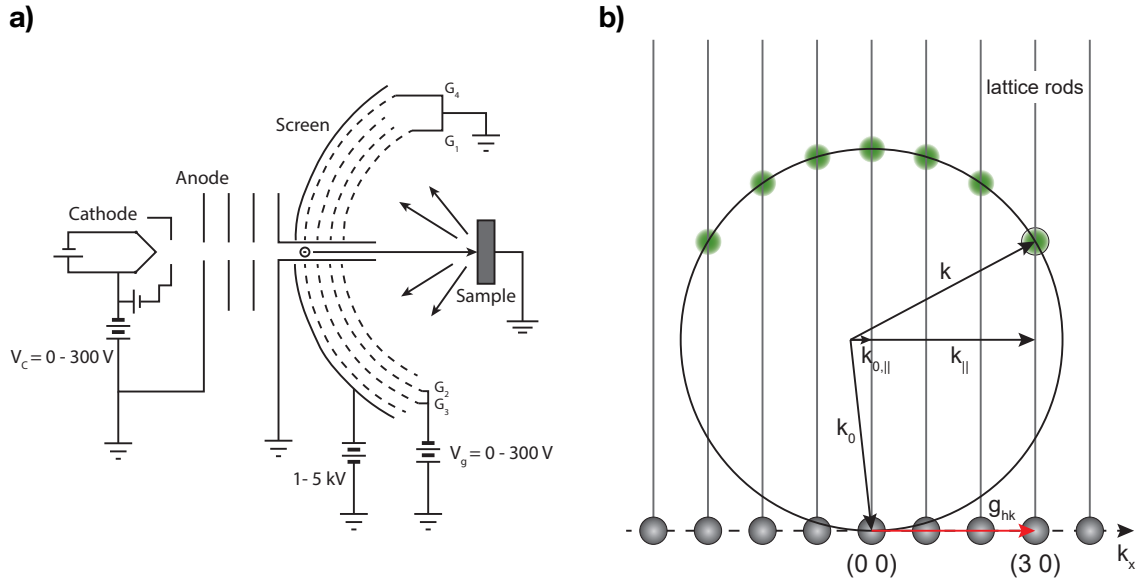


**Figure 2.4:** **a)** Schematic sketch of a typical LEED setup (adapted from [87, p. 81]). **b)** Ewald sphere construction for 2D reciprocal lattice, view along the surface (Loosely adapted from [88, p. 140]).

There is a direct connection between the the diffraction pattern and the reciprocal lattice [89, p.47]:

$$\vec{k} - \vec{k}_0 = g_{hkl}, \quad |\vec{k}| = |\vec{k}_0|. \quad (18)$$

Here,  $\vec{k}$  and  $\vec{k}_0$  are the wave vectors of the scattered and incident beam, respectively. The second equation arises from the conservation of energy and momentum in elastic scattering. The equations are the equivalent to the Bragg condition in reciprocal space.  $\vec{g}_{hkl}$  is the reciprocal lattice vector with the well known identity [90, p. 24]:

$$\vec{g}_{hkl} = h\vec{a}^* + k\vec{b}^* + l\vec{c}^*, \quad (19)$$

where  $\vec{a}^*$ ,  $\vec{b}^*$  and  $\vec{c}^*$  are the primitive translation vectors of the reciprocal lattice and connected to their real space pendants by

$$\vec{a}^* = 2\pi \frac{\vec{b} \times \vec{c}}{\vec{a} \cdot \vec{b} \times \vec{c}}, \quad \vec{b}^* = 2\pi \frac{\vec{c} \times \vec{a}}{\vec{a} \cdot \vec{b} \times \vec{c}}, \quad \vec{c}^* = 2\pi \frac{\vec{a} \times \vec{b}}{\vec{a} \cdot \vec{b} \times \vec{c}}. \quad (20)$$

The wavelength of the electrons is

$$\lambda = \frac{h}{\sqrt{2mE}}. \quad (21)$$

The electrons in LEED have an energy of roughly 30 - 300 V, so their wavelengths are of the order of 0.5 - 2 Å and can therefore resolve interatomic distances. The technique is very surface sensitive, because elastic scattering will only occur in the very first few layers of atoms. Hence, the LEED pattern originates mainly from the 2D surface lattice and only the parallel components of equation 18 need to be conserved:

$$\vec{k}^{\parallel} - \vec{k}_0^{\parallel} = \vec{g}_{hk}. \quad (22)$$

As a result, the scattering vector component parallel to the surface equals a reciprocal lattice vector [89]. To understand this in a more intuitive way, the Ewald sphere construction [91] can be used. For a 2D lattice it is shown in Figure 2.4b. There are no atoms in the direction normal to the surface, which can be understood as an infinite lattice constant in that direction. This means an infinitely small reciprocal lattice vector, which results in the appearance of lattice rods, rather than individual lattice points. The construction shows the view along the surface, with  $k_x$  lying in the paper plane. The incident beam momentum is again represented by  $\vec{k}_0$  and the scattered beams are determined by intersections of the Ewald sphere with the lattice rods. It can be clearly seen that equation 22 is true in this case. These spots represent the LEED pattern seen on the screen (as indicated by green spots in the figure). For example, the spot determined by the k-vectors shown in Figure 2.4b (black contour line) corresponds to the (30) reflex of the reciprocal lattice, as indicated by the red vector.





# 3



## Instrumentation



### 3.1. UHV Chamber

To ensure a well defined, contamination free environment, all experiments were performed under ultra high vacuum (UHV) conditions. The majority of the experiments were carried out using a Joule-Thomson Scanning Tunneling Microscope (JT-STM). The system consists of a preparation chamber and the STM chamber, which is housing the cryostat and microscope. The two chamber are separated by a gate valve. Samples can be transferred from one chamber to the other with a manipulator.

The home-built preparation chamber is equipped with a sputter gun, to clean the samples using  $\text{Ar}^+$ -ion bombardment. The device is a commercial IQE-11 from *SPECS* and is typically operated at an acceleration voltage of 0.9 kV and an Ar-pressure of  $3 \times 10^{-6}$  mbar. Metal surfaces were cleaned using grazing incidence, whereas FeSi samples showed to be cleaner using normal incidence. To anneal the samples, the manipulator is equipped with a filament, lying directly under the sample holder. For temperatures up to 500 °C strictly radiative heating is used, but electron bombardment is also employed to reach higher temperatures (*i.e.* 600 °C for FeSi). The temperature is measured by a thermocouple (TC) directly contacted to the crystal. A copper beryllium spring is pressing the two TC wires against one side of the crystal ensuring a good electrical contact and hence a precise measurement. The manipulator has two sample positions, where the lower one can be used with the TC. To minimize sample pollution by sputtering material from the manipulator onto the crystal, the upper position is used for sputtering and the lower one for annealing.

For the deposition of organic molecules as well as metals, different home-built evaporators are mounted to the chamber. Two of them are used for (organic) molecular beam epitaxy (OMBE) and comprise of two individually heatable Knudsen cells. The temperature is controlled by either resistivity measurements of a PT1000 wire or by a TC below the quartz crucible. These evaporators are used to deposit organic molecules as well as magnesium.

To deposit lanthanides, *e.g.* holmium, the required high temperatures can not be reached with the above OMBEs, so a home-built metal evaporator is used<sup>1</sup>. The metal is mounted as a thin strip between two cooled copper electrodes and heated up by applying a high-current ( $\approx 20\text{A}$ ) and high-frequency (5 kHz) voltage. Due to the cooling only the center part of the strip is heated to the evaporation temperature, which ensures a contamination free deposition. To monitor the deposition rate, a quartz crystal microbalance (QCM) is mounted at the other side of the strip with the same distance as the sample has to the strip.

<sup>1</sup>Original design by Prof. Peter Feulner, Department of Physics (E20), Technical University of Munich.

### 3. Instrumentation

---

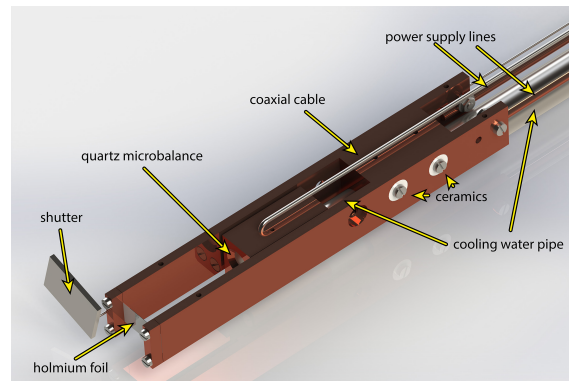


**Figure 3.1.:** 3D model of the strip evaporator used for Ho. A high-current, high-frequency voltage heats up the strip. The deposition rate can be monitored with a QCM.

Figure 3.1 shows a model of the evaporator.

Furthermore, different gases such as oxygen or carbon monoxide can be dosed to the chamber. Each gas line is equipped with an individual leak valve.

## 3.2. Joule-Thomson Scanning Tunneling Microscope

The JT-STM is mounted in an individual chamber. It is a commercial *SPECS* JT-STM (Wulfhekel Design [92]) with a cryostat from *Cryovac*. It comprises of three main components: The cryostat, the Joule-Thomson (JT) cooler and the actual STM.

**Cryostat** To achieve liquid helium (LHe) temperatures ( $\sim 4.6$  K), the system is cooled with a bath cryostat filled with LHe. Around the LHe tank, a liquid nitrogen (LN<sub>2</sub>) tank reduces radiation losses and precools the surroundings to  $\sim 80$  K. At the bottom of the tanks, thermal shields are mounted around the JT-cooler and the STM. They can be opened to insert samples to the STM. The microscope can be operated for two days without refilling in JT mode and three days in "normal" low temperature mode at 4.6 K.

**JT-cooler** In order to cool down to temperatures below LHe, a Joule-Thomson cooler is used. He gas is being liquified in a very fine capillary at the bottom of the LHe tank and brought into the superfluid state. On one side of the capillary, He gas is applied with an

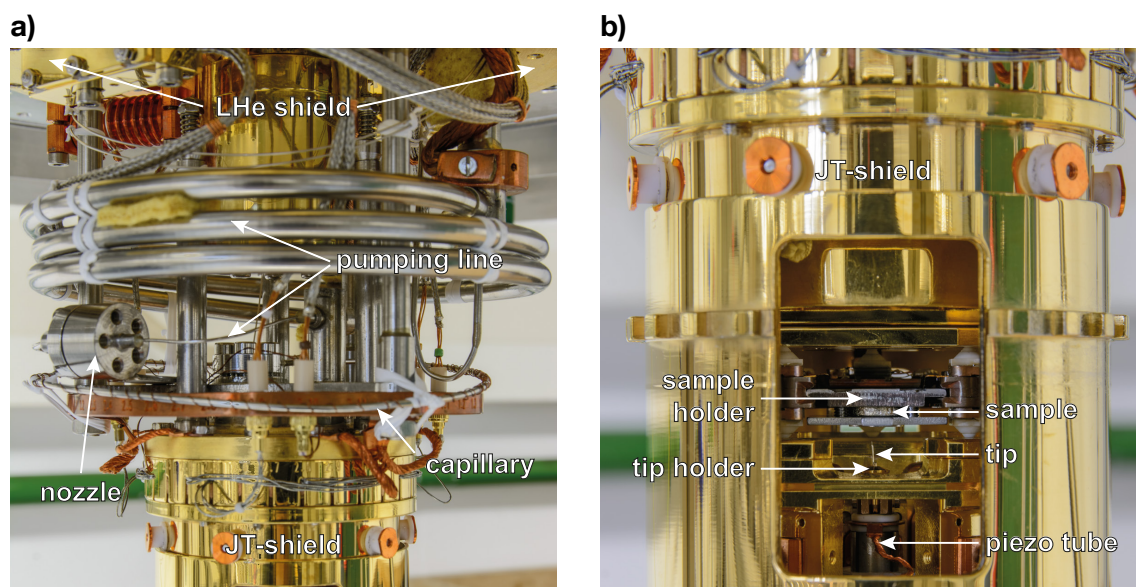


**Figure 3.2.:** a) JT-cooler of the JT-STM. b) STM inside the JT-shield. The tip is approaching the sample from below. The sample holder is 18 mm wide.

over-pressure of  $\approx 1.5$  bar. The capillary ends into a nozzle, causing the gas to expand into a larger volume. This volume is pumped from the rear-side using a rotary vane pump. On the isenthalpic expansion, namely the Joule-Thomson effect, the He cools down further and brings the JT cooler to ( $\sim 1.2$  K). The JT-stage is thermally isolated with a third JT-shield from the rest of the cryostat, but for pre-cooling the gaseous He a thermal shortcut between JT-shield and LHe shield can be closed. The different components can be seen in Figure 3.2a.

**STM** The actual microscope is placed inside the JT-shield. In the used setup, the sample is placed above the tip. The samples are mounted with a sandwich sample holder, consisting of two molybdenum plates. For coarse movement, the sample can be moved left and right using a stick-slip motor. The STM tip is a electrochemically etched tungsten tip and placed into a golden tip holder, which is mounted on top of the piezo tube (see section 2.1). To transfer samples (and tips) in and out of the microscope and to open and close the shields a wobble stick is employed.

The tunneling current is converted into a voltage by preamplifier (*FEMTO*) just after the vacuum feedthrough. It is then passed into the electronics (*Nanonis SPM system*). For differential conductance measurements, an *Ametek* digital lock-in amplifier (model 7270) is used.



# 4

## Holmium-Directed 2D Metal-Organic Coordination on Ag(100)





Adapted with permission from

Uphoff, M.; Michelitsch, G. S.; Hellwig, R.; Reuter, K.; Brune, H.; Klappenberger, F.; Barth, J. V.

Assembly of Robust Holmium-Directed 2D Metal–Organic Coordination Complexes and Networks on the Ag(100) Surface

*ACS Nano*, American Chemical Society (ACS), 2018, 12, 11552-11560

Copyright 2018 American Chemical Society

*Computational tasks were performed by G. S. Michelitsch.*

---

## 4.1. Introduction

In recent years the use of lanthanides in molecular architectures has been a burgeoning field of research, exploiting the high coordination numbers lanthanides offer in comparison to other metals. Inspired by the potential revealed in three-dimensional compounds and networks [38, 94–99], recent studies focus on the development and control of interfacial nanosystems [100–103] and architectures [43, 104–107]. Additionally, their magnetic properties are of high interest to the scientific community and major steps were done in the fabrication of lanthanide-based magnetic devices including single-molecule magnetic complexes [42, 108–113]. Recent experiments reveal prospects towards single-atom memory for single Ho atoms on a surface [44, 114]. They offer the ultimate smallest memory unit of magnetic storage devices, but are so far unstable in their confinement on the surface and exhibit loss of their magnetic hysteresis above 50 K [115].

In order to stabilize single Ho atoms from diffusion on the surface we utilize on-surface metal-organic self-assembly. As previously shown, the formation of coordination superlattices and networks permits to create and preserve stable magnetic quantum states, whereby the embedding of metal atoms in specific coordination configurations with organic ligands can greatly influence the electronic structure of the metal centers and hence their spin states [42, 111, 112, 116]. Moreover, through changing the environment by such measures, the lifetime of the spin states can be greatly increased [45].

In this work, we explore the potential of organic linker molecules combined with Ho atoms at a well-defined metal surface towards the formation of robust metal-organic nanostructures. We employ a simple, prototypical linker species, namely 1,4-benzenedicar-

## 4. Holmium-Directed 2D Metal-Organic Coordination on Ag(100)

---

boxylic acid (TPA). It is a versatile building block for the creation of supramolecular architectures on noble metal surfaces and semiconductors [37, 117, 118] and has also been employed for lanthanide-based metal-organic coordination [119]. On reactive surfaces, thermal excitation can transform the functional groups into carboxylate species whereby the deprotonation can drive phase transformations [120] and enable the formation of metal-organic coordination motifs [45]. Utilizing scanning tunneling microscopy (STM), we investigate the self-assembly behavior on Ag(100), *i.e.*, a weakly reactive surface with square symmetry. Although there is a relatively high activation barrier for deprotonation on this substrate, it was chosen because it provides the possibility to afford magnesium oxide layers, thus creating interfaces with exceptional properties regarding lanthanide-based nanomagnetism [44, 121].

Through first characterizing purely organic adlayers we show that heating-induced deprotonation generates a carboxylate precursor phase before significant loss of molecules through desorption sets in. This enables the subsequent creation of Ho-directed nanostructures. *Via* controlling the preparation conditions (*i.e.* Ho-molecule ratio, deposition and annealing temperatures), we can steer the formation of two distinct Ho-TPA phases consisting of metal-organic complexes and coordination networks, respectively. By means of density functional theory (DFT) calculations we developed structural models for the supramolecular assemblies explaining the experimental findings in great detail. Furthermore, through the DFT analysis we gain insight into the Ho coordination chemistry including the charge redistribution of the coordination nodes and the influence of the surface. We give an explanation for the chirality of the structures and a detailed analysis of strain effects, which are of general relevance in the field of surface-confined metallo-supramolecular engineering. Our work highlights the potential of Ho for the construction of surface-supported large-scale nanoarchitectures that bear prospect for nanomagnetism. Simultaneously, we lay a foundation to further exploit the exceptional magnetic properties of Ho on surfaces that arise from the occurrence as single confined entities.

### 4.2. Results and Discussion

Before we investigated Ho-directed structure formation we characterized samples with purely organic adlayers aiming at the preparation of a reactive precursor layer featuring functional groups in the carboxylate state, thus ready to coordinate to lanthanide atoms. In a first attempt, TPA molecules were deposited onto a freshly cleaned Ag(100) surface

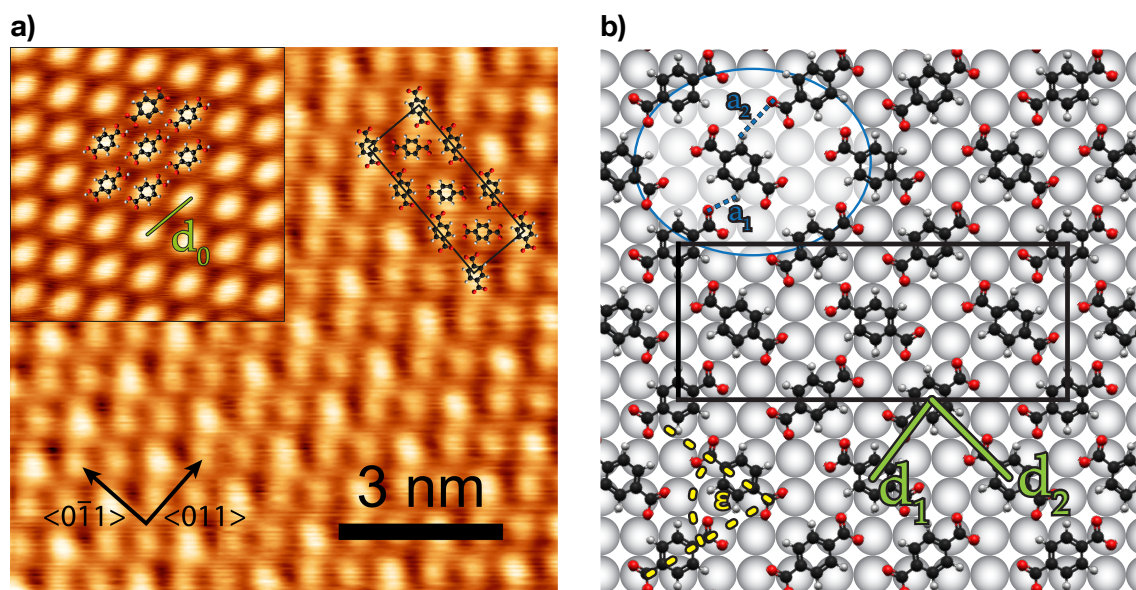


**Figure 4.1.:** Precursor phase **a)** STM image of the organic precursor layer consisting of TPA molecules with deprotonated end groups on the Ag(100) surface obtained upon adsorption at 450 K. A regular pattern of molecules appearing to be higher in topography is visible, Inset: TPA deposited at RT on Ag(100). Tunneling current  $I_T = 1.1$  nA, bias voltage  $V_B = 3$  mV. **b)** Tentative model of the organic precursor layer. The heterogeneous topography distribution of the molecules is due to higher lying TPA molecules on the bridge sites of the silver substrate. The unit cell of the organic network is marked as a black rectangle, identifying it as a  $p(10 \times 4)$  structure with respect to the underlying lattice.

held at room temperature *via* organic molecular beam epitaxy (OMBE,  $T_{OMBE} = 160$  °C).

The preparation resulted in long-range ordered domains where all molecules exhibited the same apparent height (Figure 4.1a, inset, note that all presented STM images were recorded at 4.5 K). The intermolecular distance along the molecular chains,  $d_0 = 9.7$  Å, is consistent with previous reports on hydrogen-bonded assemblies of intact TPA, as suggested by the superimposed molecular models. Subsequent annealing of the sample resulted in strong desorption losses, disqualifying this approach as a starting point. The comparison to previous results on Cu(100) [30, 45, 122, 123] and Ag(111) [124] indicates that the adhesion of TPA to the Ag(100) surface is quite limited and more similar to the close-packed Ag(111) than to the Cu(100).

Then, we developed a so-called hot deposition approach, where TPA is deposited onto a hot substrate, *i.e* the sample is held at 450 K during the 10 min deposition time. STM data obtained on that sample reveals that this preparation protocol results in a purely or-

#### 4. Holmium-Directed 2D Metal-Organic Coordination on Ag(100)

---

ganic phase with a coverage near to one monolayer (ML). The molecules form a regular adsorption pattern (Figure 4.1a), in which they appear as oval protrusions exhibiting either one of two relative brightness levels. A brighter species is surrounded by six darker ones, while each darker species is surrounded by three brighter and three darker ones. Thus, the unit cell outlined in the figure now contains six molecules. The prominent differences regarding relative brightness, unit cell size and orientation of the molecules in comparison to the previous phase of intact TPA (Figure 4.1a, inset) indicate that the adsorbates should now exhibit a different chemical state.

The small overlay in the top right corner of Figure 4.1a depicts the orientation of the molecules and a tentative adsorption model is presented in Figure 4.1b. Following previous NEXAFS studies of TPA on Cu(100) [120], we assume a flat adsorption geometry of the phenyl ring on the surface. The model describes the adlayer as a  $p(10 \times 4)$  superstructure with a density of 0.15 molecules per Ag atom and consists of doubly deprotonated TPA, *i.e.*, where both functional groups are in the carboxylate state and the phenyl ring still contains its 4 H atoms. It rationalizes the relative brightness pattern through associating the dimmer and brighter species with molecules adsorbed with their phenyl ring centered on hollow and bridge sites of the Ag lattice, respectively. Additionally, the model shows a slight rotation of the hollow site molecules around the normal vector of the phenyl ring plane. This results in a distorted T-shaped binding motif, where the carboxylates do not face the hydrogen atoms of the phenyl rings in an exactly perpendicular fashion, but rather at an angle of  $\varepsilon = 73^\circ$ , as depicted in Figure 4.1b. We suggest that the center positions of the molecules are determined by molecule-substrate interaction, whereas weak, non-covalent lateral interactions between the molecules, presumably dominated by proton acceptor ring interaction [125] induce the rotation of the molecules. The occurring intermolecular distances of nearby atoms are situated between a minimum of  $a_1 = 2.1 \text{ \AA}$  and a maximum of  $a_2 = 3.5 \text{ \AA}$  (blue circle in Figure 4.1b), thus exhibiting typical values for non-covalent interaction [126].

By a detailed analysis of the distances between molecules, we obtain indirect evidence on their chemical state. The two nearest neighbor distances of the precursor phase are labeled as  $d_1$  and  $d_2$  in Figure 4.1b. Considering the substrate registry, the distance between bridge and hollow site molecules ( $d_1$ ) is  $7.2 \text{ \AA}$  and between two hollow site molecules ( $d_2$ ) is  $8.2 \text{ \AA}$ . The layer is denser than the previous assembly of intact TPA (*cf.* Figure 4.1a inset), where the corresponding distances amount to  $7.2 \text{ \AA}$  and  $9.7 \text{ \AA}$  ( $d_0$ ). Previous studies revealed consistent values. Assemblies of doubly deprotonated TPA on Cu(100) exhibited  $d_1 = d_2 = 7.65 \text{ \AA}$  [123]. Similar distances ( $d_1 = d_2 = 7.4 \text{ \AA}$ ) were also found

on Pd(111) [127]. By contrast, packing schemes of intact TPA on Au(111) [128] showed  $d_1 = 8.5 \text{ \AA}$  and  $d_2 = 9.9 \text{ \AA}$ , consistent with our values for the intact phase and with the case of intact TPA on Cu(100), where  $d_1 = 8.1 \text{ \AA}$  and  $d_2 = 12.8 \text{ \AA}$  [120]. This comparison strongly indicates that the precursor phase on Ag(100) contains predominantly doubly deprotonated TPA.

We thus conclude that the described hot deposition method enables us to obtain a full ML of ditopic carboxylate precursor molecules with very few impurities and defects. This is a favorable outcome, since later annealing steps for the preparation of metal-organic coordination networks (MOCNs) always result in a slight loss of molecules due to thermal desorption. For coverages below a full ML (using hot deposition) two organic phases are present. Besides the precursor phase discussed above, small islands of a less dense phase form between the big islands of the precursor phase. Details on this "transition phase" are given in the Appendix (*cf.* A.1a).

### 4.2.1. Ho-directed assembly

For investigating the potential of surface-supported Ho as coordination centers we prepared a series of samples systematically varying the preparation parameters. We obtained the best results for dosing Ho at room temperature onto a full monolayer of the precursor phase followed by annealing the sample at 450 K for 10 minutes. Depending on the Ho dosage two different types of metal-organic structures were observed. Ho dosages refer to fractions of monolayers of the close-packed Ho(0001) surface (hcp crystal lattice, see Appendix A.4).

#### Cloverleaf phase

An STM image of a TPA/Ag(100)- $p(10 \times 4)$  precursor sample exposed to a very low dosage of Ho ( $\approx 0.015 \text{ ML}$ ) is depicted in Figure 4.2a.

The essential binding motif is composed of four bright features pointing towards a medium bright center interpreted as cloverleaf shape (red outline). Similar cloverleaf phases have been reported on Cu(100), involving iron or gadolinium [107] as coordination centers and multitopic carboxylate linkers [129, 130] including TPA [123]. Analogously, we suggest that here four linker species coordinate to one Ho atom, as depicted by the model overlay, making it an eight-fold coordination to oxygen. According to STM data, the unit cell vectors of this metal-organic superstructure enclose an angle of  $22.2(18)^\circ$

#### 4. Holmium-Directed 2D Metal-Organic Coordination on Ag(100)

---

with the primitive lattice vectors of the Ag(100) surface (shown in the bottom left corner of Figure 4.2a). STM data produces a quadratic unit cell of 15.60(8) Å.

With our DFT-based geometry optimization we obtained the adsorption model shown in Figure 4.2b, where the unit cell is highlighted by a black rectangle. It confirms that four carboxyl-groups are coordinated to one Ho atom. More specifically, the involved carboxylates are concertedly rotated by an angle of 53° around the C-C axis, rendering a chiral coordination scheme. This behavior of the linker groups was weakly implied in a previous study [107] and can now be confirmed by our calculations. The chirality is better visualized in Figure 4.4a and b, showing the two enantiomers side-by-side. It has been shown that the adsorption of achiral molecules can show surface-induced chirality along with chiral recognition on the formation of extended islands, greatly influencing the electronic structure [131]. This could be utilized to steer the systems nano-magnetic properties. The arrangement of the metal-organic complexes is forming a fully commensurate pattern. The top-left part of Figure 4.2a depicts an overlay of a simulated STM image calculated from the model and demonstrates the excellent agreement with the observed features in the STM data.

In our DFT calculations Ho atoms preferentially reside at the energetically favorable [132] hollow positions of the silver lattice and the lower O atoms of the carboxylates assume positions close to the Ag atop sites. With respect to the primitive crystal directions the unit cell constitutes a square  $p(\sqrt{29} \times \sqrt{29})R 21.8^\circ$  superstructure with a size of 15.56 Å × 15.56 Å, agreeing nicely with the experimental value of 15.6 Å for the length of a side. The molecule density is 0.14 molecules per silver atom. The cloverleaf phase exhibits organizational chirality and both enantiomorphic arrangements have been observed on the same sample (see Appendix Figure A.2).

The TPA molecules appear as bright oval protrusions in the STM image, whereas the Ho atoms appear transparent. The fact that the metal centers are not producing visible features in STM data is a commonly observed for metal-organic coordination motifs [107, 133, 134]. Through translating the theoretical model with respect to the STM data, it can be inferred that the linkers reside with their phenyl rings on the hollow site of the Ag(100) surface and their long axis parallel to the  $\langle 011 \rangle$  directions. This positioning is equivalent to that of TPA coordinated by Fe on Cu(100) [45]. Assuming the hollow site for the phenyl ring is in accordance with previous findings of aromatic molecules on metal surfaces [135–138]. We substantiate this with our DFT calculations, as shown in Figure 4.2b.

The Ho atoms in the cloverleaf phase are eight-fold coordinated to the carboxylate lig-

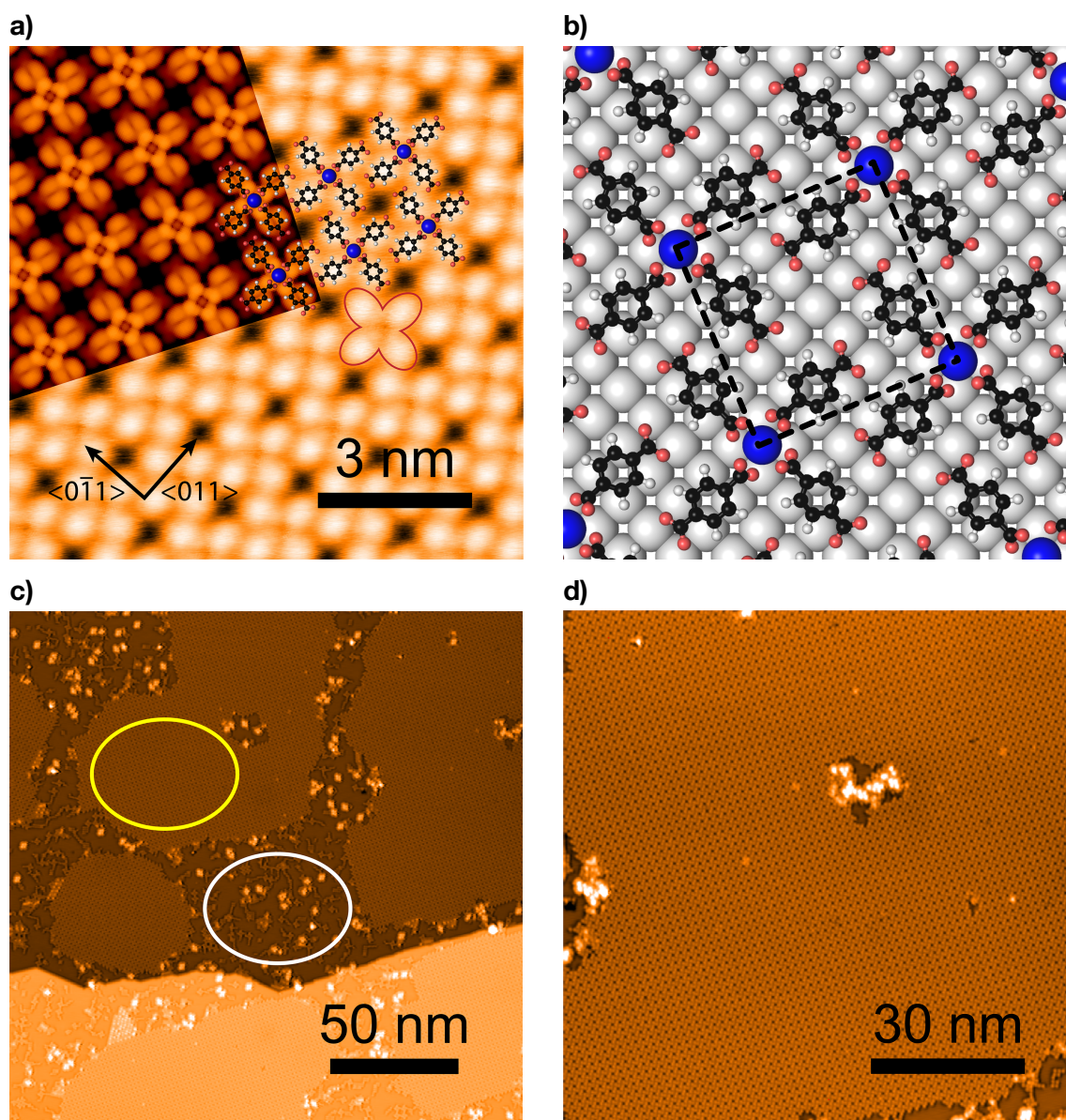


**Figure 4.2.:** **a)** High-resolution constant-current STM image of the  $\text{Ho}(\text{TPA})_4/\text{Ag}(100)-p(\sqrt{29} \times \sqrt{29})R21.8^\circ$  cloverleaf phase, superimposed by a simulated STM image. Molecules and Ho atoms are superimposed to mark their positions ( $I_T = 500 \text{ pA}$ ,  $V_B = -2 \text{ mV}$ ). **b)** DFT model for the cloverleaf phase. The unit cell is marked by the dashed square. **c)** 200 nm  $\times$  200 nm STM image showing the extent of islands on the silver surface. There are some clusters and molecules in the organic transition phase present, partly decorated by Ho adatoms (example area indicated by white ellipsoid). **d)** 100 nm  $\times$  100 nm excerpt from c) showing the quality of the islands.

#### 4. Holmium-Directed 2D Metal-Organic Coordination on Ag(100)

---

ands. This is a key difference to the cloverleaf phase of TPA-Fe on Cu(100), where the iron is fourfold coordinated to the ligands. We assign this behavior to the rather ionic character of lanthanide-organic compounds featuring higher coordination numbers [139] and the increased surface area available for coordination in the case of Ho as compared to iron. A similar eight-fold coordination motif was reported for Gd atoms and TPA on Cu(111) [107]. The rare earth atoms do not differ significantly in their chemical properties since the 4f-shell is located below the 6s<sup>2</sup> orbitals. The TPA molecules face the Ho atoms with one of their carboxylate groups, which must rotate out of the substrate plane for steric reasons. Studies of Dy-TPA architectures not involving DFT calculations were presented in terms of a coplanar orientation of the carboxylates [119]. However, our DFT calculations clearly reveal a concerted rotation of the functional groups in those structures, in agreement with Urgel *et al.* [107]. DFT simulations of the proposed bonding model (more details for DFT calculations given below) yield a Ho-O distance of 2.3 - 2.4 Å and a Ho-C distance of 2.7 Å. These distances are in accordance with previous findings for gadolinium-carboxylate molecular assemblies, where the Gd-O distance was found to be 2.6 Å and 2.4 - 2.7 Å, as deduced from the experimental model and DFT calculations, respectively [107].

As mentioned above, we propose an adsorption of the molecules at the hollow positions of the silver lattice and along the  $\langle 011 \rangle$  directions. This results in a distance of 3.0 - 3.2 Å between the oxygen atoms of the uncoordinated carboxylate group, with the hydrogen atoms of the molecule facing each other in a T-shape fashion. This distance suggests comparably weak lateral bonding. Thus molecule-substrate interaction should dominate the forces on the functional group. Consistently, our DFT calculations demonstrate that the uncoordinated carboxylate groups act as anchors to the surface, as evident from the charge transfer analysis below.

More interesting are the possibilities for binding between neighboring molecules arranged next to each other in the same orientation and slightly shifted along their axis. Here, two hydrogen atoms are very close to each other (2.1 Å) and cause a repulsive force between the molecules. On the other hand, one of the free carboxylate oxygen atoms is close to one of the ortho-hydrogen atoms and their distance of 3.0 Å would result in an attractive force caused by hydrogen bonding. These effects seem to balance each other out, leading to a configuration of the molecules as described above. Nonetheless, a slight shift and turn of the molecules would be compatible with our STM observations and would increase the H-H distance. In fact, the DFT calculations show a slight shift of the phenyl ring away from the hollow position and thereby the H-H distance is increased to 2.2 Å.



When examining islands on a larger scale we observed that the cloverleaf phase forms extended regular domains up to 200 nm in diameter. The limitation is presumably given by the size of the substrate terraces. Figure 4.2c depicts an overview image of a typical sample with an island of the cloverleaf phase highlighted by the yellow ellipsoid. We were able to get up to  $\approx 70\%$  of the silver surface covered with the cloverleaf phase. This filling factor refers to the area fraction of the substrate covered with the cloverleaf phase, determined by STM topography images and averaged over several frames. Albeit the molecule density is lower than in the precursor phase, it was not possible to obtain a saturated monolayer. We associate this behavior with the desorption of molecules during the annealing step. The islands show a high regularity and nearly no defects. This indicates an effective self-correcting mechanism during the assembly of the metal-organic structure. Also after annealing the sample again to 450 K the islands persist and no significant desorption took place. However, since all measurements were done at low temperatures, it is not possible to determine whether the islands are stable up to that temperature or whether they dissolve and reform upon cooldown. The rest of the surface is bare silver or covered by a small amount of molecules ( $\approx 2.5\%$  of the entire surface), partly decorated by Ho clusters. In Figure 4.2c, the white ellipsoid indicates an area of the surface where these molecules can be seen. The molecules not participating in the cloverleaf phase are arranged in the purely organic transition phase described in the Appendix (darker protrusions in the white ellipsoid in Figure 4.2c). Some of these molecules have a Ho adatom adsorbed on their center (bright protrusions), presumably on the phenyl ring. Upon higher Ho dosage all additional molecules can be incorporated in Ho-adatom complexes, mostly consisting of four TPA molecules in a quadratic arrangement with four Ho atoms on top.

### Checkerboard phase

Increasing the Ho dosage to a precursor sample by a factor of 10 ( $\approx 0.15$  ML) leads to the formation of a different metal-organic phase. An exemplary STM image is shown in Figure 4.3a. The TPA molecules now interlink Ho centers, making the phase a MOCN which we henceforth call checkerboard phase. Opposing molecules adsorb collinearly and show isotropic contrast, so an eight-fold coordination is present with all oxygen atoms orientated towards the Ho atoms. This results in a stoichiometry of 1 : 2 of Ho:TPA. The close-up STM topography in Figure 4.3a clearly resolves the orientation of the molecules, as indicated by the overlaid TPA models. The phenyl ring appears as a round protrusion in the middle of two oval protrusions marking the positions of the carboxylate groups.

#### 4. Holmium-Directed 2D Metal-Organic Coordination on Ag(100)

---

Again, the Ho atoms do not produce visible features in STM, for the same reasons as discussed above for the cloverleaf phase. However, the positioning of the molecules can only be reconciled by the presence of Ho coordination centers.

A model of the checkerboard phase is reproduced in Figure 4.3b. Similar to the cloverleaf phase, the vectors of the unit cell are rotated with respect to those of the substrate. An analysis of the model reveals a  $p(\sqrt{17} \times \sqrt{17})R 14.04^\circ$  superstructure with a local molecule density of 0.12 molecules per silver atom. Its domains can be rotated both clockwise and counter-clockwise with respect to the silver substrate. The endgroups of the carboxylates can be concertedly rotated in both directions, similar to the cloverleaf phase, as evident from the DFT calculations. Figure 4.3c shows both enantiomorphic structures in the bottom part of the image, where the two domain orientations are indicated by yellow lines. DFT simulations for Ho at hollow positions revealed appreciable strain which is understood as the reason why the Ho atoms are now moved to bridge-sites. Also, the phenyl rings of the TPA molecules reside on the bridge positions of the Ag(100) surface.

As can be seen in Figure 4.3c, the island size is very small (strips of  $\approx 5$  nm width) compared to the cloverleaf phase. A possible explanation is that due to the larger unit cell the silver substrate enforces upon the MOCN, the bond formation capability with the interconnecting nodes is impaired. This theory is strongly corroborated by the DFT simulation. We were not able to obtain coverages beyond approximately 15 % of the surface with this phase, although we started off with a full monolayer of the precursor phase. The small islands always come with additional Ho atoms adsorbed on some of the molecules and show an anisotropic, ribbon-like growth. Again, the networks remain after reheating the sample to 450 K and subsequent cool down.

A simulated STM image is shown in Figure 4.3d. The anisotropic differences in contrast could not be resolved *via* STM, probably due to unknown tip effects at such low bias voltages.

It has to be noted here that although the Ho dosage onto the surface is ten times higher as with the cloverleaf phase, the amount of anticipated Ho on the surface inferred from STM data (*cf.* Figure 4.3c) does not match the preparation stoichiometry. We propose a higher desorption of Ho-carboxylate complexes and clusters with Ho acting as an enhancing agent in the mechanism, though this is just a hypothesis and we can not support this by other experiments or calculations. Adsorption at step edges could also be a factor.

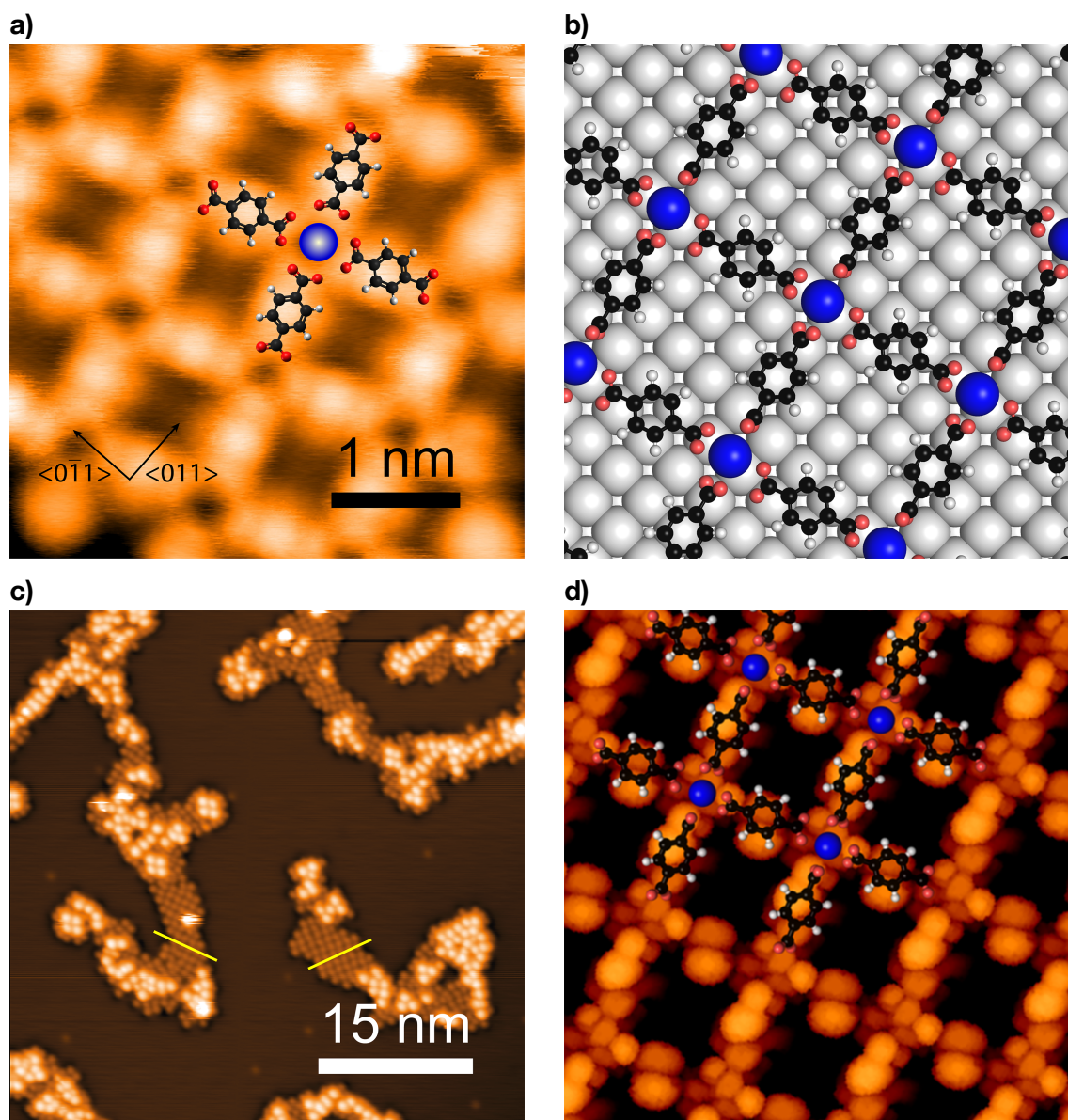


**Figure 4.3.:** **a)** High-resolution constant-current STM image of the  $\text{Ho}(\text{TPA})_2/\text{Ag}(100)-p(\sqrt{17} \times \sqrt{17})R 14.04^\circ$  checkerboard phase. Molecules and Ho atoms are superimposed to mark their positions. **b)** DFT model for the checkerboard phase. **c)** 200 nm  $\times$  200 nm STM image showing the extent of islands on the silver surface. The islands are rather small and decorated on the edges by excess Ho atoms. The yellow lines indicate the two domain orientations **d)** Simulated STM signature of the checkerboard structure.

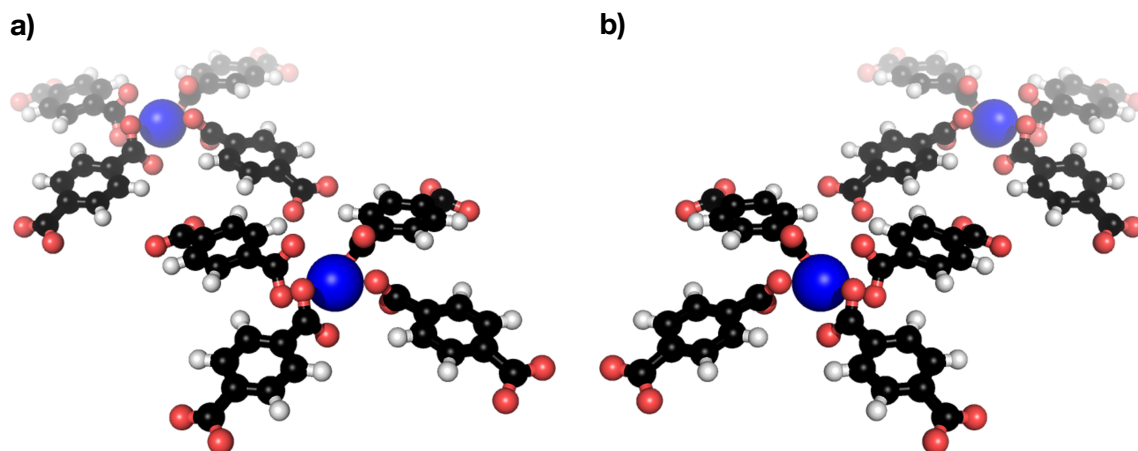


**Figure 4.4.:** a), b) Bonding environment in the mononuclear cloverleaf-structure with the carboxylate linkers tilted by approximately  $53^\circ$  with respect to the molecular plane. As can be seen the complex is chiral due to the concerted rotation of the carboxyl-groups.

#### 4.2.2. DFT analysis of Ho-TPA networks

Dispersion-corrected DFT calculations were performed for periodic supercells of both structures. A free-standing overlayer of the checkerboard phase was allowed to freely adsorb on the metal slab to find the equilibrium adsorption geometry. This approach is similar to previous calculations on metal-carboxylate architectures on metal surfaces [133, 140]. The calculations reveal a severe strain of the checkerboard structure, when stacked commensurably onto the Ag(100) surface. The silver lattice then imposes a Ho-Ho distance of 11.9 Å on the entire structure, while a free-standing layer of the structure would have a lattice periodicity of 11.4 Å. If the initial  $C_4$ -symmetric geometry with the Ho-atom centered on the Ag(100)-hollow site is optimized towards an equilibrium structure, the geometry relaxation will always break the linker-Ho-bond on one end of the TPA molecule (*cf.* Figures 4.4 and A.4 in the Appendix). Figure 4.5 shows an intermediate 8-fold coordinated MOCN structure with the Ho atom adsorbed on the hollow site and the directions of the forces acting on the respective atoms. The structure does not represent a global minimum of the potential energy surface and the forces acting on the molecule would require to break open one of both carboxyl-holmium bonds to relieve the strain.

A closed 2-dimensional metal-organic framework could only be stabilized by allowing this symmetry-breaking from the initially assumed  $C_4$  to a  $C_2$  symmetry axis centered on the Ho-atom. The reduction in symmetry is accompanied by the Ho-atom leaving the Ag(100) hollow sites. This removes a part of the strain in the structure, since the TPA

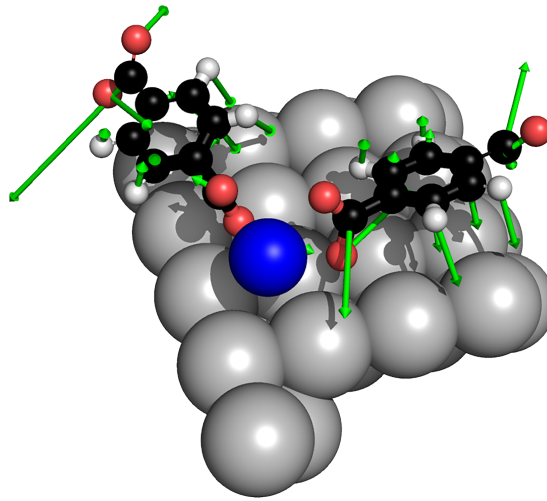


**Figure 4.5.:** Forces (green vectors) acting on the linker molecules in the unreaxed checkerboard structure where the Ho is still positioned in the hollow place (*cf.* Figure A.4, **H2**). Magnitude of vectors not to scale.

charge	cloverleaf				checkerboard		
	O <sup>surf</sup>	O <sup>Ho</sup>	Ho	Ag	O	Ho	Ag
e/atom	-0,32	-0,37	+1,17	+0,05	-0,36	+1,12	+0,01
e/cell	-2,54	-2,95	+1,17	+1,47	-2,90	+1,12	+0,46

**Table 4.1.:** Mulliken charges of the cloverleaf and checkerboard-structures per atom and per unit cell. In the cloverleaf structure, two distinct species of oxygen atoms are present, the Ho-bonded O<sup>Ho</sup> and the surface-anchored O<sup>surf</sup>.

molecule does not need to bend from one hollow-site towards the next one. We assign this observed strain as primary reason why the checkerboard pattern could only be observed in small band-shaped islands of less than 10 observable subunits in the shorter dimension, as opposed to MOCNs with commensurable registry [104, 123, 134]. A symmetry reduction is also discernible in the STM data, in the shape of the framework hollow-sites, where either cushion-shaped  $C_4$ - ( $\square$ ),  $C_2$ - ( $\square$ ), or  $C_1$ -symmetric squares with concave arched edges are observed. This symmetry-breaking due to substrate-induced stress is also reflected in the simulation. A Mulliken population analysis (as listed in Table 4.1 for Ho, Ag, and O) suggests charge transfer from the Ho-atom towards the carboxylate linker atoms. Further electron density is depleted from the surface in the vicinity of the bonding node (*cf.* Figure 4.6).

The  $C_4$ -symmetric arrangement of the cloverleaf deduced from the experimental data is fully consistent with our calculations. The optimized geometries obtained for both the

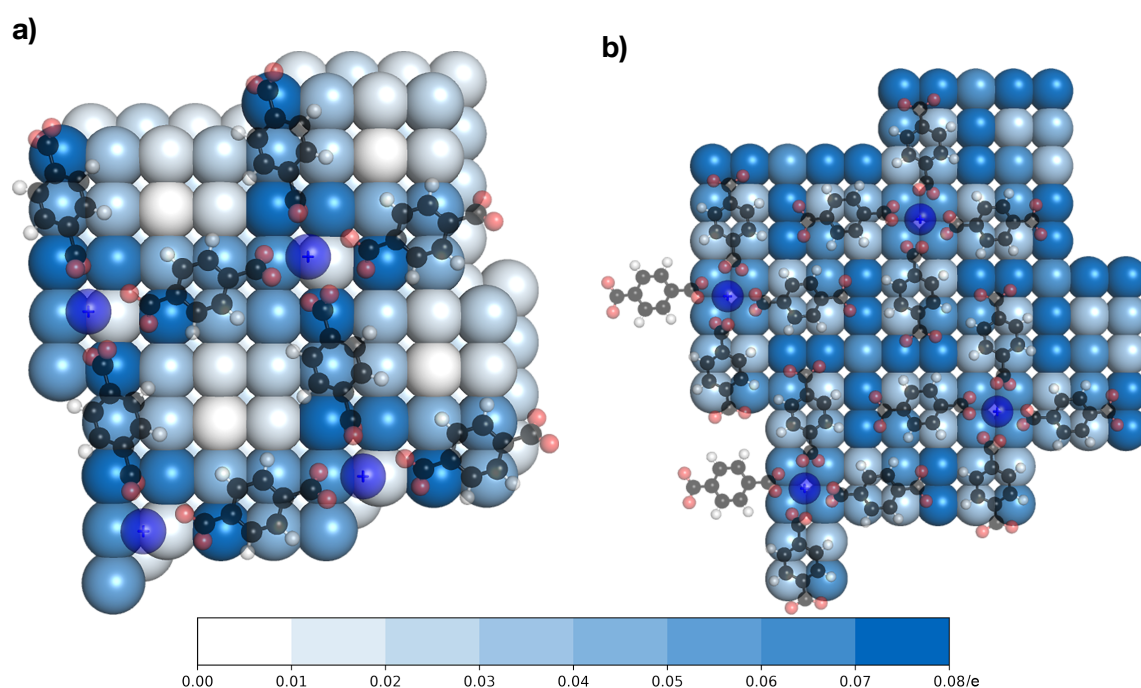


**Figure 4.6.:** Hotspots of the charge transfer between the substrate and the adsorbate. Highlighted in blue are the areas of high electron depletion compared to white (no electron charge depletion) in fractions of  $e$ . Adsorbate shown without color coding for reference purposes.

high-symmetry cloverleaf and the broken-symmetry checkerboard phase are stable minima of the potential energy surface with relaxed bond distances fully consistent with those derived from the STM measurements, thereby strongly supporting the structural models derived from the experimental data. The simulated STM images in Figures 4.2a and 4.3d indicate that the Ho-site is transparent at the employed tunneling conditions, since the 4f eigenstates in both bonding environments lie at far too high and low energies with respect to  $E_F$ . Indeed, there is a local minimum seen at the interconnecting Ho-nodes in the experimental data. Similar observations for different lanthanide atoms have already been reported elsewhere [107]. The smaller, yet bright protrusions around the central depression (Ho-center) are clearly unoccupied states of the neighboring carboxylic oxygens, in our simulations presumably over-delocalized by the employed semi-local DFT functional [141]. To a much smaller extent the same signatures are also visible in some of the experimentally recorded images as shown in Figures 4.2a and 4.3a. The Mulliken population analysis shown in Table 4.1 for Ho, Ag, and two species of non-equivalent oxygen atoms suggests very similar values for the charge transfer from Ho and the substrate towards the carboxylate linkers. The charge transfer from the substrate occurs primarily at two points: the anchor-points of the dangling carboxylate linkers and at the Ho-node (*cf.* Figure 4.6). In contrast to the cloverleaf structure, all carboxylate groups in the checkerboard pattern are rotated out of plane to accommodate the bonding environment and effectively reduce the charge transfer. The charges do not add up to zero, because only atoms with charge transfer to the surface are listed here.

### 4.3. Conclusions

In conclusion, two different types of thermally robust molecular architectures of TPA and Ho on the Ag(100) surface were fabricated by finely tuning the deposition parameters. We were able to build up enantiomorphic islands of mononuclear lanthanide-carboxylate compounds with  $\text{Ho}(\text{TPA})_4/\text{Ag}(100)-p(\sqrt{29} \times \sqrt{29})R 21.8^\circ$  structure, high lateral extent, surface coverage, and low defect density. Reticulated MOCNs have a  $\text{Ho}(\text{TPA})_2/\text{Ag}(100)-p(\sqrt{17} \times \sqrt{17})R 14.04^\circ$  structure and feature reduced island sizes due to interfacial strain effects. The two observed metal-organic architectures are both chiral, due to a rotation of the superstructure with respect to the silver lattice and a concerted rotation of the carboxylates. In the case of the cloverleaf phase conformational chirality is also present. These structural models receive further support by DFT calculations, which identified high strain

#### 4. Holmium-Directed 2D Metal-Organic Coordination on Ag(100)

---

as potential reason for the limited extent to which the checkerboard phase could be grown experimentally. The chiral signature of the Ho coordination sphere could afford intriguing new magnetic features.

Additionally, our DFT calculations give insight into the charge redistribution within the molecular architectures. Stabilization of single Ho atoms with 8-fold coordination in the cloverleaf structure is a particularly promising approach to exploit the recently found magnetic properties of Ho atoms on surfaces without being hampered by the onset of Ho diffusion at low temperatures. This work shows that Ho can be stably deployed as single atoms on surfaces, which opens up the possibility to investigate the nanomagnetic properties of Ho in a well-defined molecular environment, *e.g.* by means of X-ray magnetic circular dichroism (XMCD). The possibility to grow insulating decoupling layers such as NaCl or MgO on Ag(100) provides prospects to tune their magnetic properties *via* supramolecular on-surface engineering and a comparison of Ho-carboxylates both on MgO and Ag will give further insight into this intriguing field of research.



# 5

## TPA-Ho Complexes on MgO/Ag(100)



## 5.1. Introduction

As the introduction of chapter 4 already states, the utilization of single Ho atoms as magnetic storage units [44, 114] offers the ultimate smallest memory unit. We already showed that terephthalic acid (TPA) can serve as a molecular linker to inhibit diffusion at higher temperatures on the Ag(100) surface and that well-defined coordination environments bear the potential of tuning the spin states of the Ho atoms [93]. The study also showed a possible pathway to influence the spin states of the metal centers by changing their chemical environment. However, the use of magnesium oxide layers as platforms to electronically isolate the metal-organic structures and their spin states from influences of the metal surface remains unachieved. In this work, we introduce a 2 ML isolation layer of MgO between the silver surface and Ho-TPA complexes.

## 5.2. Results and Discussion

### 5.2.1. Magnesium Oxide Growth on Ag(100)

The growth of magnesium oxide layers on metal surfaces has been investigated in numerous studies with low energy electron diffraction (LEED), auger electron spectroscopy (AES), X-ray and ultraviolet photoelectron spectroscopy (XPS/UPS), scanning tunneling microscopy (STM). Typical substrates are Mo(100) [142, 143], Fe(100) [144] and Ag(100) [145–151]. MgO crystallizes in the rocksalt structure, *i.e.* it has a cubic unit cell and is an ionic crystal. Opposed to NaCl, the atoms are double charged ( $\text{Mg}^{2+}\text{O}^{2-}$ ). It has a bulk lattice constant of 4.2 Å [152], which makes the Ag(100) (lattice constant 4.079 Å [153]) surface an ideal candidate to grow MgO(100) layers with an epitaxial fit.

In previous studies, the MgO layers frequently show an inhomogeneous thickness distribution and inhibit the growth of extended islands [150]. The surface would then show areas of pure Ag, as well as MgO stacked up to multilayer pyramids. This behavior is disadvantageous, if one is aiming at the formation of ordered molecular architectures. Significant improvements were made using slow cooling rates [150], though the MgO patches on the surfaces were still limited to a few nanometers in size. Following this route, we finely tuned the growth parameters to achieve MgO surfaces of > 50 nm width. It has to be noted here that even bigger islands could be grown, but the presence of bare silver patches was required to perform tip forming with the STM tip.

Prior to the MgO growth, the surface was cleaned with repeated Ar-ion sputtering

## 5. TPA-Ho Complexes on MgO/Ag(100)

---

( $E = 900 \text{ V}$ ) and annealing at  $500 \text{ }^\circ\text{C}$ . The preparation is performed through the evaporation of pure Mg under oxygen atmosphere. The Mg was purchased as a solid rod from *Sigma-Aldrich*,  $\geq 99.9\%$ . After generously removing the oxide layer with a knife, small Mg chips were peeled off the rod and directly transferred into UHV. Before evaporation the Mg was degassed at a temperature well above the final evaporation temperature to get rid of residual oxides on the surface of the chips. The Mg is evaporated out of a Knudsen cell at an evaporation temperature of  $430 \text{ }^\circ\text{C}$ . The sample is held at a temperature of  $500 \text{ }^\circ\text{C}$ . The oxygen introduced to the chamber (purity 5.0) is kept at a partial pressure of  $1 \times 10^{-6} \text{ mBar}$ . For a coverage of  $\approx 70\%$  the Mg is evaporated for 15 min onto the sample. After stopping the Mg evaporation, the sample is kept at the same temperature and under oxygen atmosphere for one minute. This post-annealing ensures the incorporation of all Mg clusters and atoms into MgO on the surface. Subsequently, the sample is slowly cooled down to  $100 \text{ }^\circ\text{C}$  with a cooling rate of  $-10 \text{ K/min}$ . After the sample reaches  $100 \text{ }^\circ\text{C}$ , cooling is performed faster. Our experiments show that the crucial part of the cool-down lies at the higher temperatures, quenching the sample at  $100 \text{ }^\circ\text{C}$  does not affect the quality of the MgO.

A constant current STM image of a typical MgO preparation can be seen in Figure 5.1a. The MgO areas are visible as  $\approx 100 \text{ nm}$  wide islands with numerous ramifications on the edges. Figure 5.1a and 5.1b show the same area of the sample at  $1 \text{ V}$  and  $3 \text{ V}$ , respectively. The appearance in b) is strikingly different to a). While the bare silver shows the same contrast, the MgO islands seem to be nearly inverted in apparent height. Also, the MgO island in the top part appears flat at  $3 \text{ V}$ , but not so in the  $1 \text{ V}$  image. The explanation for this behavior lies in the electronic structure of the MgO film. There are two distinct states above the Fermi level for MgO on Ag(100): The Ag/MgO interface state at  $1.7 \text{ eV}$  and a MgO surface state at  $2.5 \text{ eV}$  [146]. Therefore these states are not available for tunneling at lower bias voltages [143, 147, 149]. While Figure 5.1a shows the topography of the sample including the MgO, 5.1b shows mainly the topography of the silver substrate underneath. By comparing the two images, the number of layers of the MgO film can be deduced. The two big islands in the bottom part show the same apparent height in both images, whereas the top island has three different apparent heights in the  $1 \text{ V}$  image. Therefore, the island consists of MgO films with thickness modulations of 1 - 3 ML.

This becomes even more evident, when calculating the difference between the two images, as shown in Figure 5.2a. By subtracting the  $1 \text{ V}$  topography, *i.e.* the silver substrate, the homogeneous structure of the bottom islands and the heterogeneous thickness distribution of the top island is clearly visible. While it seems to be evident that the bottom islands

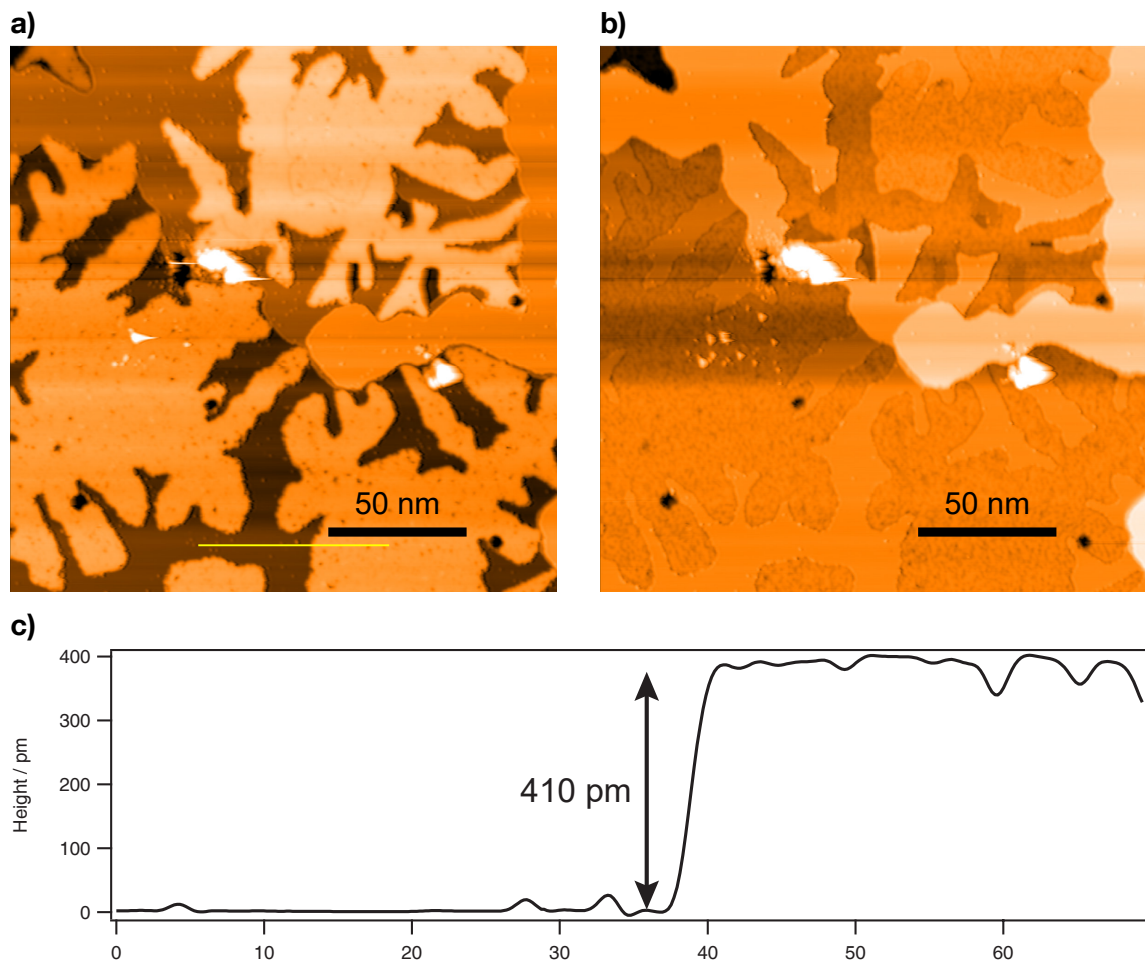


**Figure 5.1.:** STM images of MgO on Ag(100) taken at different bias voltages. At higher voltages, tunneling occurs into the MgO surface state, whereas lower voltages mainly access the silver states. **a)**  $V_B = 3$  V **b)**  $V_B = 1$  V. **c)** Line profile along the yellow line in a) identifying the island as 2 ML thick. The profile was extracted from the data in a) ( $V_B = 3$  V).

## 5. TPA-Ho Complexes on MgO/Ag(100)

---

are of the same thickness, the actual thickness remains to be determined. There are two different monolayer definitions in literature. We follow the definition, where 1 ML is defined as half a MgO(100) unit cell [147, 154], but most publications [44, 155, 156] refer to 1 ML as full unit cell of the MgO(100). Nevertheless, since we also found MgO terraces with a height of half the MgO unit cell, we deem that definition more appropriate. When discussing findings of papers that use the other ML definition, the units will be converted. Figure 5.2c shows an atomistic model of our MgO thickness definition as a side view.

A line profile of the bottom island (as indicated by the yellow line in Figure 5.1a) is shown in Figure 5.1c. It shows an apparent height of the island of 410 pm with respect to the silver, identifying it as 2 ML MgO film. More line profiles were taken at different positions of the sample and show a height difference of  $4.06(16) \text{ \AA}$ , which is in good agreement with the assumption of 2 ML MgO. The relatively big standard deviation of this value is caused by the varying height differences at different Ag/MgO interfaces. For example, the difference is bigger when Ag is next to 3 ML of MgO rather than 2 ML and one Ag layer, all with respect to the same base Ag layer. It is also possible to grow single monolayers of MgO, though they occur rarely with the used preparation parameters and appear as small patches between 2 ML islands and Ag(100). A STM image of an island including a monolayer of MgO can be seen in the appendix in Figure B.1a.

The thickness of the MgO can also be determined by tunneling spectroscopy. "Classical" STS experiments with open feedback loop and using the lock-in technique (*cf.* section 2.1.3) on MgO showed that the Ag/MgO interface state at 1.7 eV is strongly quenched when going from two to three ML and completely vanishes for 4 ML [149]. However,  $dz/dV$  spectra can resolve it also at higher film thicknesses [151]. The numerically calculated spectra give a higher weighting to low energy states, while also causing a slight shift in the peak positions. Moreover, the distance in energy between the Ag/MgO interface state and the MgO surface state gets smaller with increasing film thickness and can therefore be used to determine the MgO thickness directly. To measure a  $dz/dV$  spectrum, the feedback loop is closed and the voltage will be ramped over the energy interval of interest. Afterwards, the derivative of the recorded z-signal is calculated. Much longer acquisition times are needed for clear spectra with this method, though for single point spectra this disadvantage is not critical. Figure 5.2b shows three spectra from 0.5 - 3 V taken at different positions on the surface, as indicated by the colored crosses in Figure 5.2a. While the bare silver has no distinct features (black curve), the two MgO spectra show two clearly resolved peaks at around 1.9 V and 2.6 V, respectively. While the magnitude of the interface state is similar in both curves, the MgO surface state features double

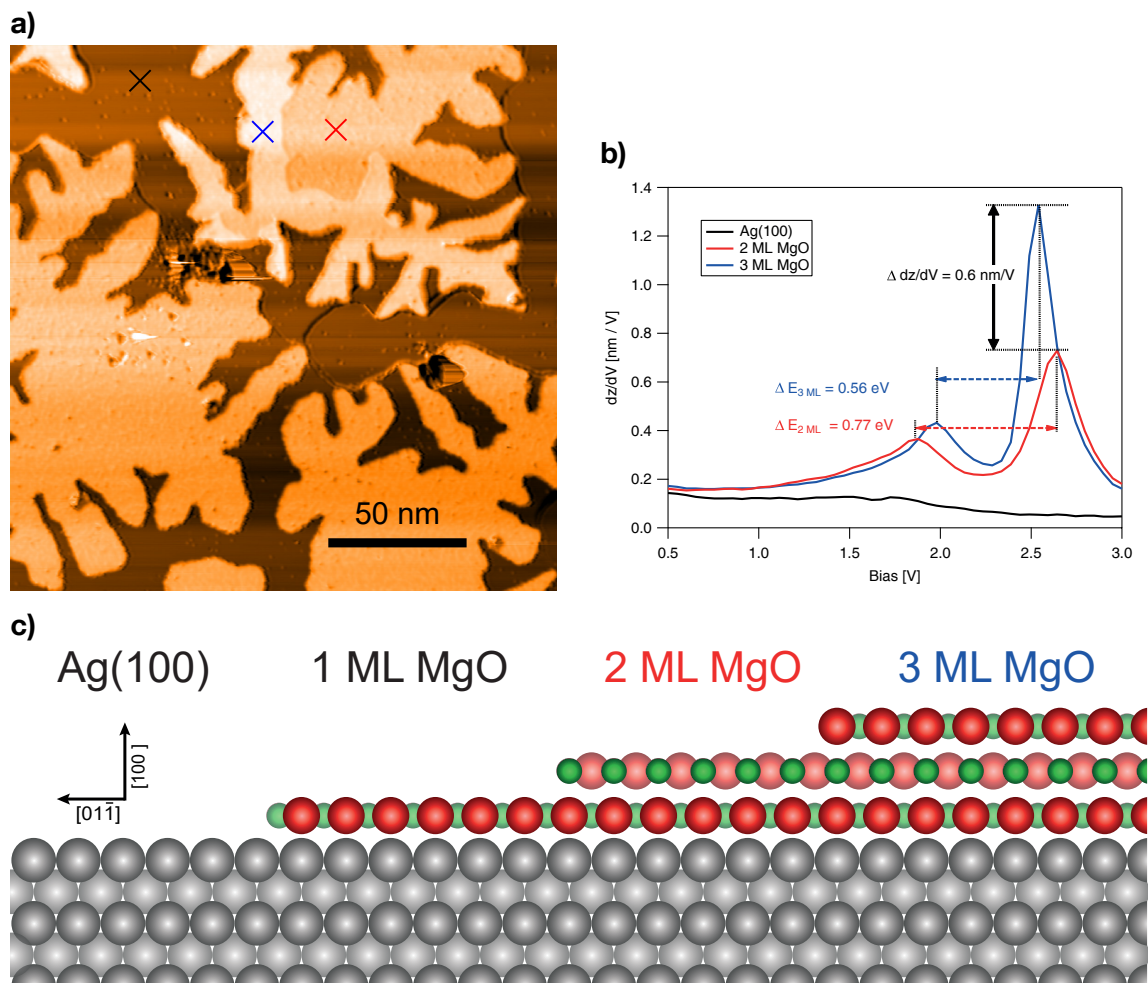


**Figure 5.2.:** **a)** Difference image of Figure 5.1 **b)** Numerical  $dz/dV$  spectra on different positions of the sample. The positions are marked as colored crosses in **a)**. The thicker the MgO is, the closer are the peaks of the interface and surface state together. **c)** Atomistic model of the different MgO thicknesses. Shaded atoms lie in a deeper plane along the viewing direction.

## 5. TPA-Ho Complexes on MgO/Ag(100)

---

the intensity in the blue curve. Additionally, the blue peaks are closer in energy to each other as the red peaks. We observe a separation of 0.77 eV for the red and 0.56 eV for the blue spectrum. This energy gap of the states confirms the assumption of a bilayer and a trilayer at the different points and has been used before for the characterization of MgO film thicknesses [154, 156]. A single monolayer only shows the peak at 2.6 V, as can be seen in the appendix in Figure B.1b. It has to be noted here that the separations measured in these studies all differ slightly due to different spectroscopy techniques, since the use of numerical  $dI/dV$ , numerical  $dz/dV$ , lock-in  $dI/dV$  with the feedback loop opened and  $dI/dV$  with a closed feedback produce different peak positions [151], similar to the behavior of  $dI/dV$  maps acquired in different modes [73]. However, the general trend is for the peaks to get closer together on increasing film thickness.

### 5.2.2. TPA Deposition on Ag(100)/MgO

Similar to the preparation process described in chapter 4, an organic precursor layer is prepared. We again used 1,4-benzenedicarboxylic acid (terephthalic acid, TPA) as the organic linker species and aimed for a full monolayer on the MgO. To fully activate the organic adlayer for lanthanide coordination, the solely presence of their functional groups in the carboxylate state is desired. To gain a better understanding of the adsorption and deprotonation behavior of TPA on MgO(100) different deposition rates were used. Whereas on Ag(100) the TPA molecules show a high desorption rate upon annealing, they are quite temperature stable on MgO. We deposited the TPA on 2 ML MgO. Note that the surface also features bare Ag(100) to perform tip forming (*cf.* section 5.2.1).

After extensive degasing the purity was checked by evaporating onto a clean Ag(100) surface and comparing the molecular self-assembly to previous preparations. Then, TPA was evaporated at room temperature onto the Ag(100)/MgO surface. To gather a first understanding of the adsorption behavior on MgO, a low dosage was used ( $T_{OMBE} = 170\text{ }^\circ\text{C}$ ,  $t = 2.5\text{ min}$ ) and the sample was directly transferred to the STM without annealing. An image of the sample can be seen in Figure 5.3a. On the one hand, stable scanning is challenging, because a low bias ( $< 500\text{ mV}$ ) is required to image the TPA molecules. On the other hand, no MgO states are available for tunneling at that bias (*cf.* section 5.2.1). Therefore, the molecules appear as oval shaped bright spots with dark halos and the surrounding surface having roughly the same apparent height as them. The height difference between the MgO surface and the top of a TPA molecule in a 300 mV constant current STM image is  $-10$  to  $10\text{ pm}$ . This causes the tip to crash occasionally and makes the



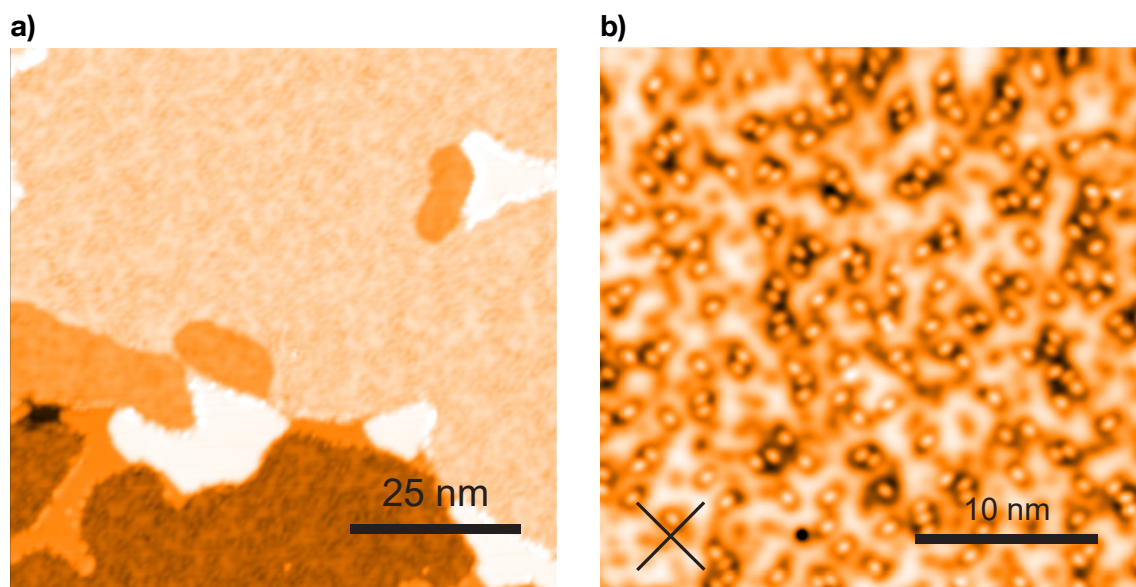


**Figure 5.3.:** **a)** STM image of TPA deposited at room temperature on Ag(100)/MgO, no annealing. Deposition parameters:  $T_{OMBE} = 170\text{ }^{\circ}\text{C}$ ,  $t = 2.5\text{ min}$ . The TPA only adsorbs on the MgO. **b)** Closeup STM image of a). The TPA molecules align themselves parallel to the  $\langle 110 \rangle$  directions (black cross). Both images taken at  $V_B = 300\text{ mV}$ .

presence of the clean silver surfaces essential for tip conditioning.

The TPA molecules seem to exclusively adsorb on MgO. The closeup image in Figure 5.3b shows that the majority of the molecules align themselves along the primitive lattice vectors (black lines) of the substrate. Moreover, there are many isolated single molecules. This is opposed to the behavior on bare Ag(100), where TPA is arranging itself in stripes along the  $\langle 110 \rangle$  directions, as indicated in Figure 5.4a. It is hard to tell, if the molecules are deprotonated or not, because the absence of the stripe formation makes it difficult to measure their length. The carboxylic acid groups feature a high electronegativity, while the  $\text{Mg}^{2+}$  ions of the substrate offer an attractive adsorption spot for them. The strong Coulomb interaction between the oxygen atoms of the molecules and the cations of the substrate seems to fix the molecules on their positions, inhibiting the formation of islands.

Increasing the evaporation dosage ( $T_{OMBE} = 170\text{ }^{\circ}\text{C}$ ,  $t = 5\text{ min}$ ) results in a fully covered MgO substrate and the formation of the well known stripe-shaped molecular self-assembly on the bare Ag(100). An STM image of such a sample can be seen in Figure 5.4a. The MgO films are fully covered with molecules, as the closeup image in 5.4b shows. The silver is partly covered with stripes of TPA molecules. The stripes feature the same prop-

## 5. TPA-Ho Complexes on MgO/Ag(100)

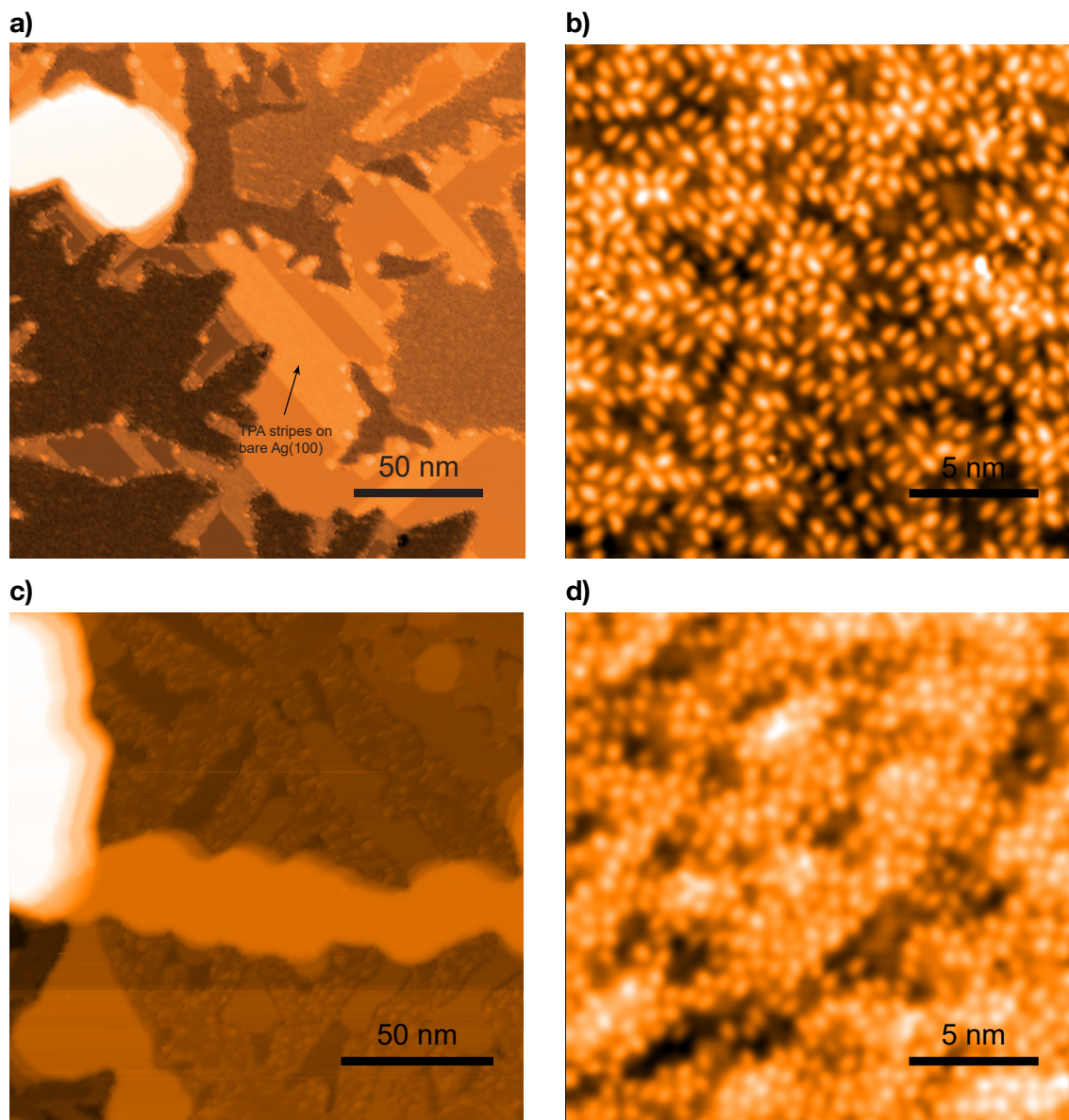


**Figure 5.4.:** **a)** STM image of TPA on Ag(100)/MgO, no annealing. Deposition parameters:  $T_{OMBE} = 170\text{ }^{\circ}\text{C}$ ,  $t = 5\text{ min}$ . The TPA fully covers the MgO and begins to form stripes on the Ag(100).  $V_B = 500\text{ mV}$ . **b)** Closeup STM image of **a)**. Some of the molecules are slightly rotated out of the primitive lattice directions of the substrate.  $V_B = 100\text{ mV}$ . **c), d)** The same sample after 10 min annealing at 450 K. The silver is empty but the MgO remains decorated. **c)** and **d)** taken  $V_B = 500\text{ mV}$ .

erties as the TPA self-assembly on a clean Ag(100) surface. The molecules on the MgO occasionally show a deviation in their orientation from the crystal directions. We propose two complementary explanations for that. Firstly, the MgO surface has some defects that introduce an electrostatic impurity to the ionic MgO film and might influence the exact orientation of molecules in the vicinity. Secondly, the high density of molecules paired with low diffusion rate of TPA molecules on MgO can cause steric hindrance effects, because the molecules seem to be unable to rearrange themselves on the MgO. Measuring the center to center distances of nearest neighbors produced values of 9.5 - 10.4 Å. These distances are similar to intact TPA molecules on other surfaces [120, 128] and also on Ag(100), as discussed in chapter 4. Therefore, we assume the molecules to be pristine on the MgO when the sample is not being annealed after deposition.

To ensure that metal-organic coordination will only take place on the MgO, the bare silver should be kept free of molecules. Otherwise the formation of structures as described in chapter 4 could occur. While it is quite difficult to dose the TPA exactly in the required amount, a post-deposition desorption of the undesired molecules proved to be quite straight-forward: Upon annealing the sample to a temperature of 450 K for 10 min all molecules on the Ag(100) surfaces desorb, while the molecules on the MgO show no signs of loss in coverage. On the contrary, the molecule density on MgO has slightly increased and nearest neighbor distances were reduced to 8.4 Å. STM images of the surface after annealing are shown in Figure 5.4c and 5.4d. We interpret this higher coverage and the smaller distances with two processes: The TPA gets deprotonated and consumes less space on the surface. Additionally, some of the molecules that were adsorbed on the bare silver diffuse onto the MgO and occupy the free space that was cleared via deprotonation. Again, due to defects on the MgO, no long-range ordering is visible.

In summary, the adsorption behavior of TPA on Ag(100)/MgO surfaces can be described as follows: TPA shows a strong interaction with MgO, resulting in strongly bound molecules. At low dosages of TPA, only the MgO will have molecules on it. This is because of a high diffusion of TPA on Ag(100) and a very low (or inhibited one) on MgO due to the higher binding energy of TPA on MgO. Once a molecule is on the MgO, it strongly binds and stays there. Higher coverages that result in completely filled MgO terraces, show the formation of stripe-shaped molecular self-assembly on the Ag(100) parts of the surface. These islands are equivalent to those on pure Ag(100)/TPA samples. Annealing the sample results in the loss of the molecules on the silver, whereas the ones on MgO stay on the surface. Furthermore, the TPA gets deprotonated during annealing and the coverage on the MgO slightly increases, because the blanks get filled by molecules that

## 5. TPA-Ho Complexes on MgO/Ag(100)

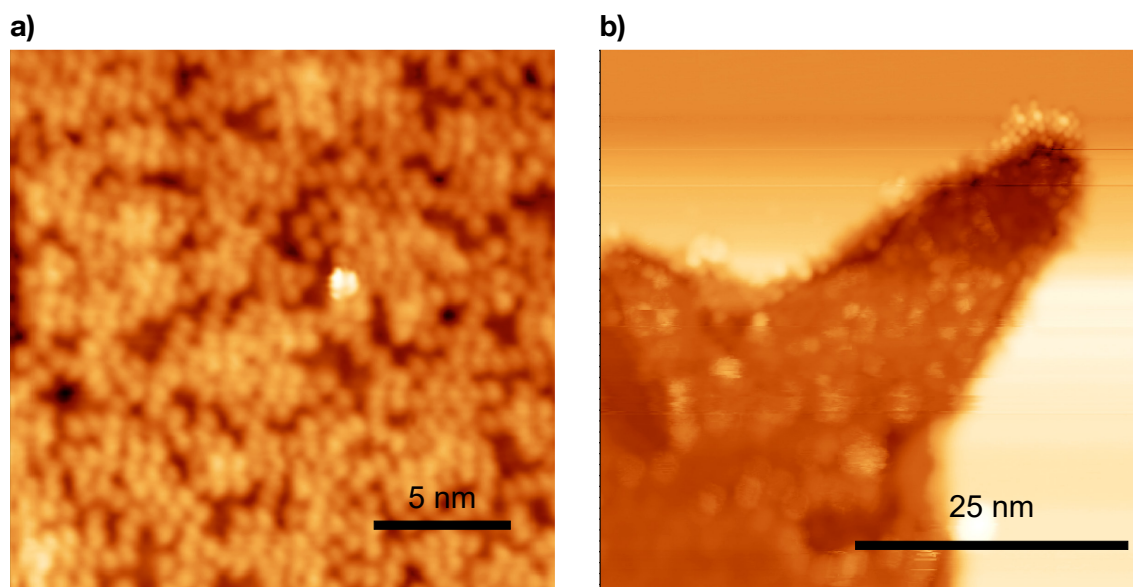


**Figure 5.5.:** a) Ho deposited on 1 ML TPA on 2 ML MgO. No complex formation. Ho dosage:  $\approx 0.015$  ML. The bright protrusion is a Ho cluster.  $V_B = 300$  mV. b) Same sample as in a), but showing more Ho clusters that predominantly adsorb near step edges.  $V_B = 500$  mV.

were formerly adsorbed on the Ag(100).

### 5.2.3. Ho-TPA complexes on Ag(100)/MgO

Once the precursor layer described in section 5.2.2 is prepared, Ho is deposited onto the surface. We chose the same dosage as for the open porous cloverleaf-phase described in section 4.2.1, namely  $\approx 0.015$  ML of Ho. The Ho is deposited at room temperature and the sample is subsequently annealed. Using the same annealing temperature as on the Ag(100) surface (450 K) did not result in any complex formation, as can be seen in Figure 5.5a. The surface sample looks the same as in Figure 5.4d, with the addition of Ho clusters on top (bright protrusions). Note that the Ho was more prominently adsorbed close to step edges and that the image does not show the full extent of Ho coverage. Figure 5.5b shows such a place on the sample, though due to the high Ho concentration on that spot, stable scanning was hardly possible and hence the image quality is rather poor.

The annealing temperature was increased step-wise and the sample was checked for complex formation in the STM after every annealing step. Significant changes in the surface morphology occurred after annealing the sample to 650 K. Figure 5.6a shows a MgO surface covered with TPA and Ho. In contrast to the 450 K sample, the Ho clusters are now

distributed more equally. For better visibility, some of the clusters are marked by dashed circles. Also some complexes are formed, as can be seen in Figure 5.6b. The majority of them shows a contrast similar to the cloverleaf complexes described in section 4.2.1. We will focus on these in the following structural analysis. We assume an 8-fold coordinated bonding motif, with four TPA linkers coordinated to one Ho atom. The molecular linkers are visible as bright spots, the Ho atom in the center does not produce a visible feature, probably for the same reasons as discussed in chapter 4. The STM data was analyzed to measure the center to center distances of the molecules as well as the orientation of the complexes. For measuring the distances, line profiles along the complexes were fitted with gaussians, one for each molecule in the profile. Taking the average over 12 molecules produces a TPA center to center distance of 11.55(50) Å (*cf.* Figure 5.7b). The complexes are slightly rotated with respect to the primitive lattice vector by an angle of 15.18(95)°.

Based on this information and taking the STM images as a template, a tentative adsorption model was deduced. The model is shown in Figure 5.7a. The adsorption site of the Ho was assumed to be on top of an oxygen atom, which is in accordance with DFT calculations of single Ho atoms on MgO [44]. However it has to be noted here that our DFT calculations for the Ho-TPA system on Ag(100) described in section 4.2.2 showed that the coordination of TPA by Ho can push the Ho atom away from its assumed equilibrium position. On the other hand, for the cloverleaf complexes on Ag(100) (which are very similar to the complexes on MgO) the Ho stayed in the same position as assumed for single Ho on the surface. Therefore, we consider the assumption of Ho adsorption on top of oxygen as reasonable for this case.

In the model, the carboxylates adsorb on the bridge site between two oxygen atoms. As mentioned above, Ho is assumed to be adsorbed on top O-sites and therefore the centers of the TPA molecules are separated by four oxygen sites in the [110] and one oxygen site in the  $[1\bar{1}0]$  direction. This is equivalent to a turn of the complex around the Ho atom by an angle of  $\sqrt{17}^\circ \approx 14.04^\circ$ , which is in good agreement with the experimentally determined value of 15.18(95)°. Similar to the observations on Ag(100) in chapter 4, the slight rotation renders a chiral adsorption scheme, being present in both rotation directions. The two enantiomers are shown side-by-side in the model. Both are imaged in the STM data, as can be seen in Figure 5.6b, where the two enantiomers are visible in the yellow ellipsoid and red lines marking their axes. The black arrow is parallel to the [001] direction and represents the mirror axis of the two axes of the complexes. Figure 5.6c shows a close-up of them. The model predicts a TPA center to center distance of 11.90 Å, which is slightly larger than most of the measured distances, as indicated by the dashed line in Figure 5.7b.

## 5. TPA-Ho Complexes on MgO/Ag(100)

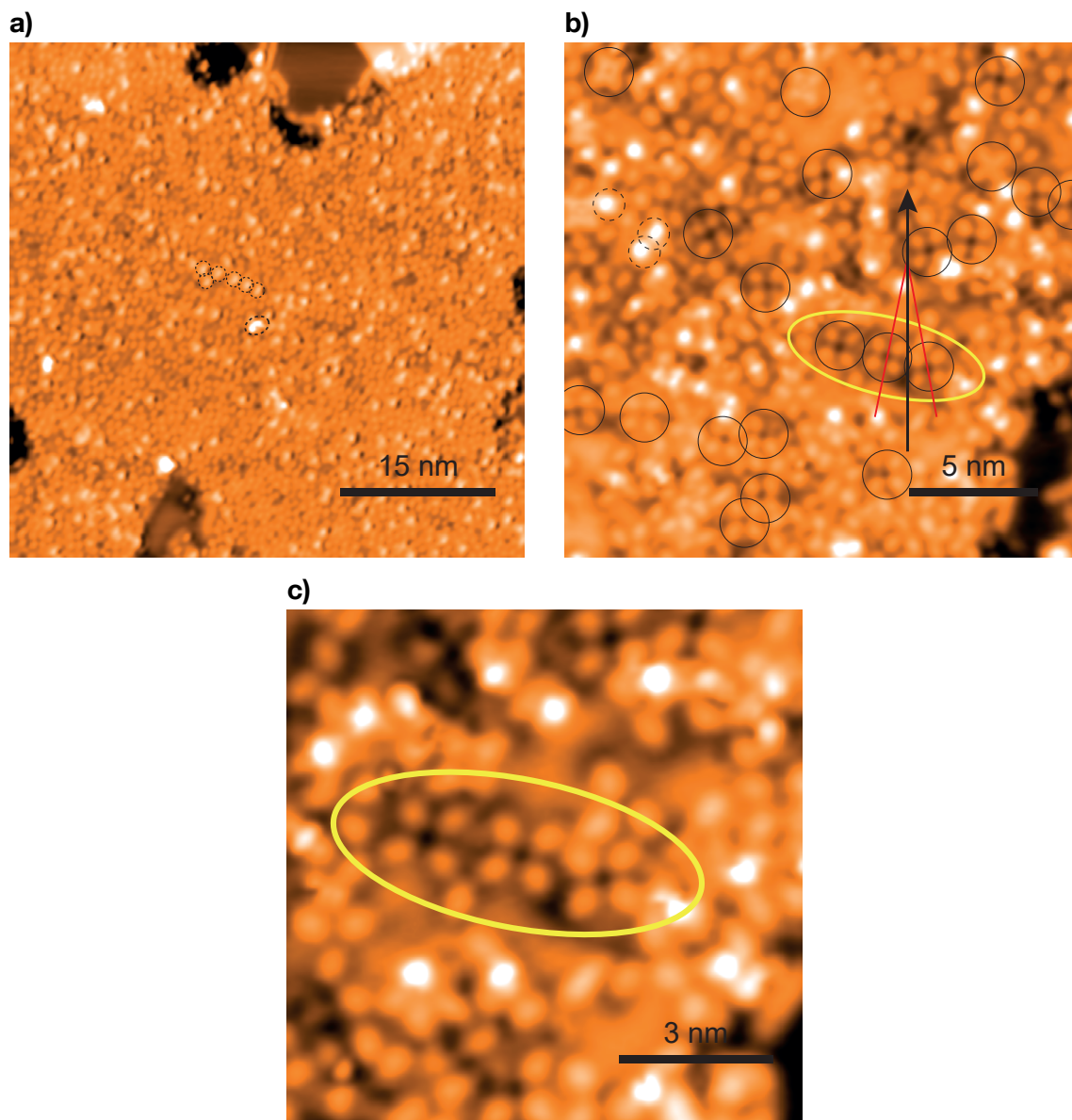


**Figure 5.6.:** **a)** Sample of Figure 5.5a after annealing to 650 K. The Ho clusters are distributed more equally on the TPA layer and complex formation occurs. For better visibility, some clusters are marked by dashed circles. **b)** Close-up of a), showing the local formation of cloverleaf complexes, marked with black circles. Red lines mark the complex axes of the two enantiomers. The [001] direction is marked by the black arrow. **c)** Close-up of the complexes marked by the yellow ellipsoid in b). All images acquired at  $V_B = 300$  mV.

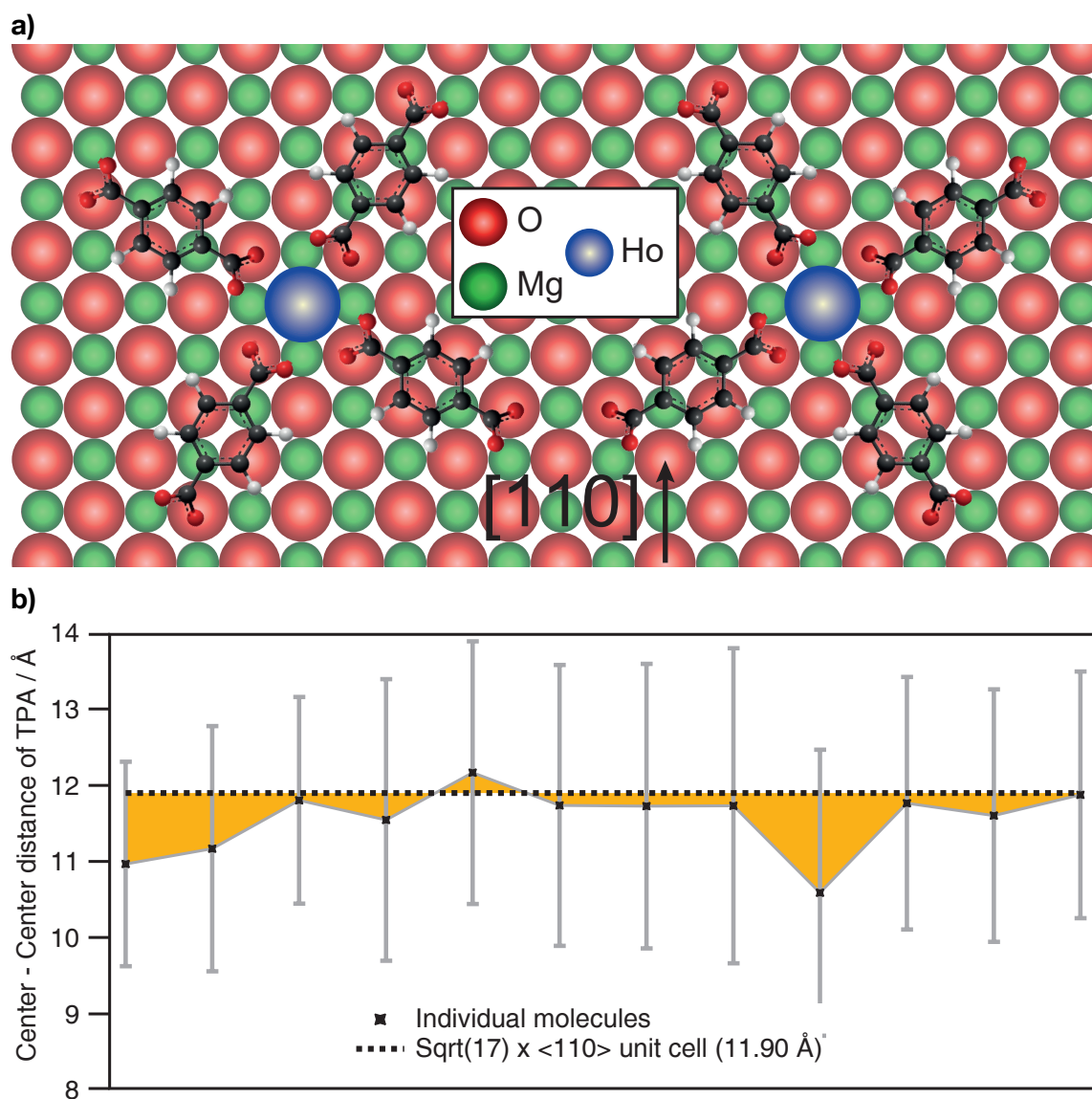


**Figure 5.7.:** a) Tentative model of the Ho-TPA complexes on MgO. The long axis of the molecules is rotated by  $14.04^\circ$  with respect to the  $[110]$  direction b) Center to center distances of individual TPA-Ho complexes. The dashed line shows the theoretical distance deduced from the model in a).

## 5. TPA-Ho Complexes on MgO/Ag(100)

---

The uncertainties for the distances are quite large, because they were calculated from the full widths at half maxima of the protrusions in the STM images, so the actual uncertainty is probably significantly smaller. Figure 5.6c shows the typical resolution of an image used for distance measurements.

A slight translation of the molecular linkers away from the exact bridge position towards the Ho atom could serve as an alternative explanation for the deviation of the experiment from the model. This behavior fits the case in Ag(100), as our DFT calculations showed for that system (*cf.* section 4.2.2). Furthermore, the translation vectors between individual molecules are the same as those for individual Ho atoms in the checkerboard phase on Ag(100) (*cf.* section 4.2.1). The functional groups of the carboxylates are rotated out of plane by  $45^\circ$ , since all our calculations for TPA-Ho complexes on Ag(100) showed that 8-fold coordination requires this rotation to accommodate the bonding environment and reduce charge transfers to the surface. The value of  $45^\circ$  is chosen rather arbitrary, however, and signals the groups are very likely to be rotated. Because the complexes did not form islands, it is not possible to determine a regular superstructure.

### 5.3. Conclusions

In conclusion, MgO films with high homogeneity in thickness were grown on the Ag(100) surface. By finely tuning the preparation parameters, a surface morphology consisting mainly of 2 ML MgO and pure silver was engineered and confirmed by scanning tunneling spectroscopy experiments. While MgO serves as the designated experimental platform for on-surface metal-organic architectures, the silver surfaces offered the possibility to perform tip conditioning, which is essential due to the low corrugation of adsorbents on MgO and hence the delicate tip stability during scanning.

After the fabrication of the MgO/Ag(100) surface template the adsorption behavior of TPA was investigated. Deposition at room temperature resulted in the adsorption of pristine TPA along the  $\langle 110 \rangle$  directions. At coverages close to 1 ML the orientation of some molecules was distorted by defects in the MgO film. The molecules show a strong preference to adsorb on the polar films. The silver surface stays clear until all MgO surfaces are covered. Subsequently, exceeding molecules grow islands in the well known stripe pattern on Ag(100). Annealing of these highly covered samples results in a deprotonation of the TPA molecules on the MgO, as well as a desorption of all molecules occupying silver surfaces. This sample serves as an organic precursor layer for metal-organic architectures



on MgO.

For the fabrication of lanthanide-coordinated metal-organic structures 0.015 ML of Ho were dosed onto the surface at room temperature. Subsequent annealing was used to trigger the formation of complexes. While the formation of complexes already occurred at 450 K on Ag(100), MgO proved to require significantly higher temperatures. Notable complex formation took place at an annealing temperature of 650 K. The complexes show high resemblance to the cloverleaf complexes on Ag(100). They consist of four TPA molecules being 8-fold coordinated by one Ho atom in the center. Structural analysis of the STM data led to a tentative adsorption model, showing that the complexes are rotated by an angle of  $14.04^\circ$  with respect to the  $\langle 110 \rangle$  directions. The Ho atom was assumed to adsorb on top of oxygen, in accordance with previous findings in literature. Due to the absence of island formation, the identity of a possible superstructure remains unknown, though further improvement of the preparation procedure remains on the agenda and could yield results of higher regularity.

It was shown that Ho-directed metal-organic complexes can be fabricated on MgO films on Ag(100). Though further tuning of the fabrication process is required, this proof of principle study lays the basis to further investigate the system in terms of its magnetic properties, *e.g.* by means of XMCD. The separation of Ho atoms by molecular linkers overcomes the problem of clustering at higher temperatures. Also, it combines the astonishing properties of Ho on MgO films with the intriguing possibilities of spin state tuning by changing their chemical environment.



# 6

## Structural and Electronic Properties of the FeSi(110) Surface



## 6.1. Introduction

For several decades, studies on iron silicide (FeSi) and its B20 relatives (*e.g.* MnSi, CoSi, CrSi) unraveled the exceptional properties of these compounds and made them an intriguing field of research ever since. The unusual behavior of susceptibility and conductivity [157] in FeSi at low and elevated temperatures raised the question of classifying it as a so called Kondo-insulator, despite the lack of f-elements [47]. Surface conductivity may play a role in the unusual conduction characteristics. Whereas surface conduction due to reconstructions shows a very low conductivity compared to the bulk due to scattering effects [158–161], topologically protected surface states show a bulk-exceeding conductivity, because scattering effects are suppressed [162–165].

Studies on this material class of Kondo-insulators - a member of the class of "heavy fermion" systems [166] - predicted that some materials that feature a small band gap as well as strong electron correlation, may exhibit topologically protected surface states [46, 47, 167]. A recent example is samarium hexaboride ( $\text{SmB}_6$ ), where a finite resistivity at low temperatures was associated with topological protected surface states [168–175], though even very recent studies remain contradictory on the exact mechanism [49, 176–182]. In  $\text{SmB}_6$ , an exemplary mystery is the presence of spatially extended quantum oscillations and simultaneous absence of long range charge transport [183, 184]. The search for protected surface states in other Kondo-insulator candidates to explain their anomalous conduction behavior [185–189] clearly stresses how narrow band-gap insulators with strong electron correlation are promising candidates to further elucidate the effects responsible for the conduction mechanism in heavy fermion systems.

FeSi, as a strongly correlated d-electron narrow band-gap semiconductor [46, 157, 190–196] is such a promising candidate. At elevated temperatures, it resembles a paramagnetic metal above room temperature while being a narrow band-gap  $\approx 60$  meV semiconductor below  $\approx 150$  K [157, 190–196]. Recently it was proposed that electron correlations may be responsible for the two different regimes [197], while the semiconductor state was oftentimes explained in terms of classical band theory [46, 157, 190–196].

Recently, the Pfleiderer group performed low temperature transport measurements [198] and reported evidence pointing to the existence of a low temperature surface conduction channel in FeSi(110), which could be caused by topologically protected surface states [50]. While the general behavior of conductivity and susceptibility matched previous studies [194, 199, 200], they give a new possible explanation for the saturating conductivity, which was previously explained with an impurity band [194–196]. They showed the im-

## 6. Structural and Electronic Properties of the FeSi(110) Surface

---

munity of this new conduction channel to magnetic impurities and hence rise the suspicion of topologically protected surface state. The goal of this work is to gain a deeper insight into the FeSi(110) system by investigating the structural and resulting electronic properties of the (110) surface by means of scanning tunneling microscopy (STM), scanning tunneling spectroscopy (STS) and density functional theory (DFT) and possibly to resolve unknown surface states and other electronic features of the narrow band-gap in FeSi.

### 6.2. The B20 crystal structure

FeSi crystallizes in the moderately complex B20 crystal structure, which was firstly identified by Phragmen in 1923 [201]. Since FeSi was the first compound it was assigned to, it is also known as the FeSi structure. It was identified as the crystal structure of several Si-(CrSi, MnSi, FeSi and CoSi), Ge- (CrGe, MnGe, FeGe, and CoGe) and Al/Ga-based alloys (AlPd, AlPt, GaPd, GaPt) [202]. The interatomic distances in the B20 structure are significantly smaller than one would expect from the covalent radii of the involved elements. The reason the structure is preferred over the much simpler B1 (NaCl) or B2 (CsCl) or even B8<sub>1</sub> (NiAs) structure is the covalent bond character of the structure. The 7-fold coordination involves the orbitals to resonate between closest neighbors and neighbors in vicinity. The too high or too low coordination numbers of the other crystal structures do not allow for this behavior and are hence ruled out for FeSi and its relatives [203].

The B20 crystal structure can be seen in Figure 6.1a. The simple cubic (SC) unit cell consists of 8 atoms. The atoms lie at the positions  $(u, u, u)$ ,  $(0.5 + u, 0.5 - u, \bar{u})$ ,  $(\bar{u}, 0.5 + u, 0.5 - u)$  and  $(0.5 - u, \bar{u}, 0.5 + u)$ , where  $u$  is a material specific value for each elemental species. Hence, the two individual  $u$ -values for a material determine the eight atom positions. The B20 structure can be interpreted as a distorted variant of the rock-salt structure (B1), as for  $u = \{0.25, 0.75\}$  the B20 becomes the B1 structure [206]. The lattice parameters given for FeSi in the following are based on the neutron diffraction measurements from Watanabe *et al.* [205], inter-atomic distances and their errors are calculated from these values [204]. At liquid nitrogen temperatures, the unit cell has a size of 4.493(50) Å and the displacement factors of the Fe and Si atom on the (111) space diagonal are  $u_{Fe} = 0.1358$  and  $u_{Si} = 0.844$ , respectively. Note that none of the atoms lie on the planes of the cubic unit cell. This makes the structure rather difficult to understand. The B20 structure has the space group  $P2_13$  (number 198), so whilst the unit cell is cubic, the point symmetry is tetrahedral due to the 3-fold rotational axes along the  $\langle 111 \rangle$  direc-

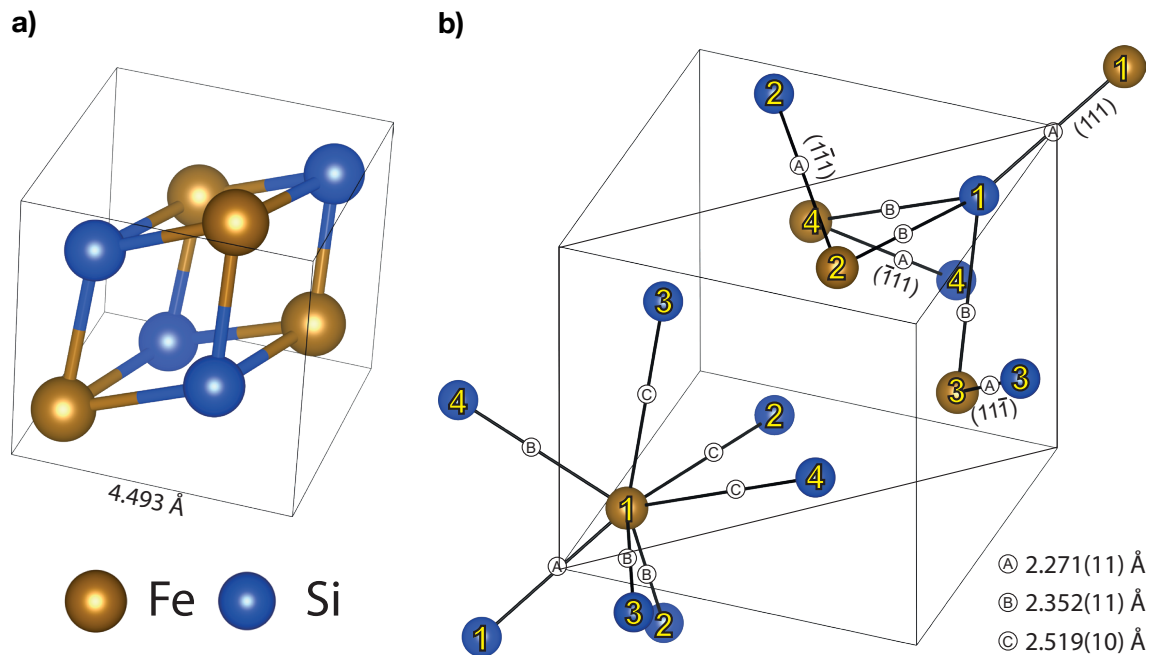


**Figure 6.1.:** a) Unit cell of FeSi. The cubic unit cell contains eight atoms. b) Distances of the individual atoms to their nearest neighbors, also those outside the unit cell. The angle of view is the same as in a). Identical distances are marked by letters A-C. All "bonds" with the letter A point along the  $\langle 111 \rangle$  directions. The (110) plane is indicated by the black rectangle and atoms #1 lie in that plane. Produced with *VESTA* [204] and partly adapted from [205].

tions [206]. These vectors are marked in Figure 6.1b. The two-fold screw axis causes the Fe-Si-Si-Si and Si-Fe-Fe-Fe tetrahedrons to be rotated by  $180^\circ$  with respect to each other.

Figure 6.1b also shows all relevant distances to nearest neighbors and are denoted by the letters A, B and C. Atoms with the same number are at equivalent positions regarding to the crystal symmetry. The Fe and Si atoms along the  $\langle 111 \rangle$  directions (Fe(1)Si(1)) show a separation of  $A = 2.271(11) \text{ \AA}$ . There are two tetrahedrons in the unit cell, containing one Fe and three Si atoms (Fe(1)Si(2,3,4)) and vice versa (Si(1)(Fe(2,3,4))). The single species is always the tip of the tetrahedron lying on the space diagonal ( $[111]$  direction). These atoms are labeled with #1 in the figure and lie in the (110) plane (black rectangle), which is the orientation of the crystal used in this work (see below). The (Si(1)(Fe(2,3,4))) distance is  $B = 2.352(11) \text{ \AA}$  while the opposing tetrahedron shows an edge length of  $C = 2.519(10) \text{ \AA}$ . The crystal structure is chiral, because it does not show inversion symmetry, but both enantiomorphic representations are energetically the same. The other variant can be realized by replacing every Fe atom with Si and vice versa. Following previous

## 6. Structural and Electronic Properties of the FeSi(110) Surface

nomenclature the enantiomer with Fe in the corner closest to the origin ( $u \approx 0.14$ ) is labeled form A [207, 208]. It has to be noted here that the form present in the crystal used in this work was not determined.

### 6.3. FeSi(110) surface

#### 6.3.1. STM measurements

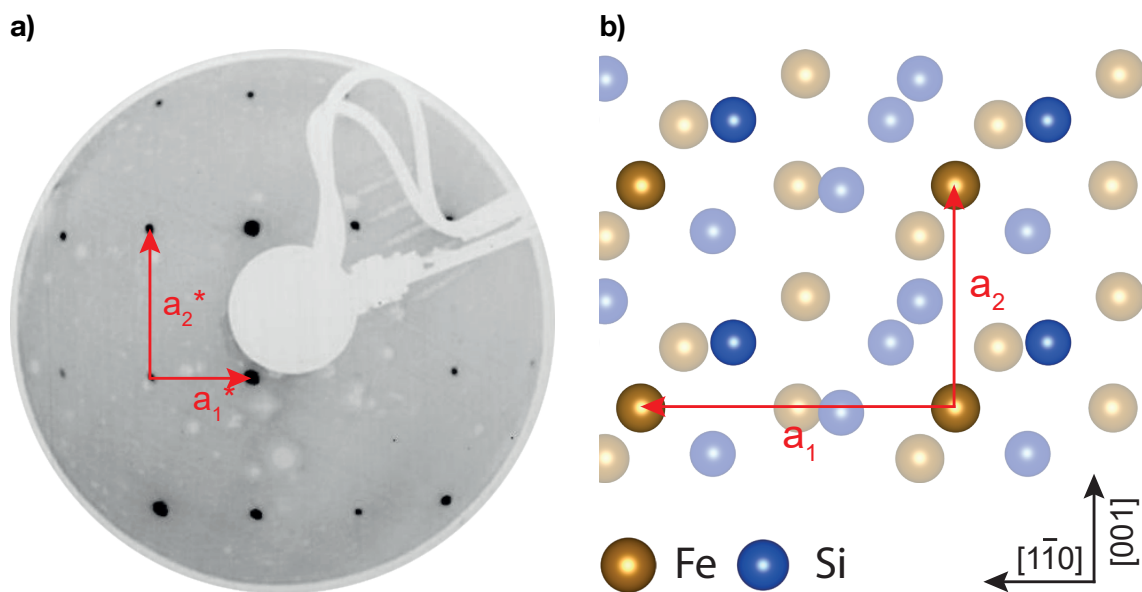


**Figure 6.2:** a) LEED image of the FeSi(110) surface. The reciprocal lattice vectors are indicated by red arrows. Electron energy  $E_{el} = 102.6$  eV b) Possible surface structure for the (110) surface, consisting of type 2 atoms (*cf.* Fig. 6.1). The shaded atoms are located in deeper planes. More planes are shown in Figure 6.5. The arrows show the primitive lattice vectors and are labeled in accordance with their reciprocal counterparts in a). The bulk unit cell is marked in black.

The crystal used in this work was grown with the optical floating-zone method under UHV conditions [209] and subsequently cut and mechanically polished. The crystal was then transferred UHV and treated with Ar-ion sputtering and annealing, similar to ref. [210]. To confirm an atomically well-defined surface, low energy electron diffraction (LEED) experiments were performed. A LEED pattern of the surface after several cleaning cycles and annealing the sample to 600 °C can be seen in Figure 6.2a. The rectangular unit cell of the (110) surface is clearly resolved and the length ratio of the reciprocal lattice



vectors shows the expected value of  $1 : \sqrt{2}$ . For additional evidence, we extracted the lattice constant from the LEED image by calculating the length of  $\vec{a}_2$ . Therefore we took the average value deduced from the first three diffraction orders and using a Ru(111) crystal as reference. This produced a value of  $a_2 = 4.4(1) \text{ \AA}$ , which is in good agreement with the value given in literature [205]. Both the measurements on FeSi as well as Ru were done at a sample temperature of  $\approx 110 \text{ K}$ . The uncertainty originates from the not fully identical mounting arrangements of the crystals in front of the LEED. The rectangular LEED pattern and its correct length ratio combined with the matching lattice constant gives evidence for the absence of a surface reconstruction. The real-space lattice vectors that correspond to the reciprocal ones in the LEED pattern are marked in Figure 6.2b. The model shows only one possible surface structure of the (110) surface, further information on that is given below. The shaded atoms are lying in deeper layers. The primitive cubic unit cell is marked by the black lines. Additionally, we investigated the chemical composition of the surface with X-ray photoelectron spectroscopy (XPS) to ensure a contamination free surface, especially free of carbon and oxygen. XP spectra can be seen in the appendix in Figures C.3 and C.4. We noticed a substantial loss of carbon contamination after annealing the sample to  $600 \text{ }^\circ\text{C}$  rather than  $500 \text{ }^\circ\text{C}$ .

After the characterization with LEED and XPS, the crystal was transferred to the JT-STM. Employing the cleaning process in the same manner as before, the crystal was investigated by STM. Figure 6.3a and 6.3c show constant current images of the FeSi(110) surface. While a) shows a large scale image with some of the vacancies and adatoms<sup>1</sup>, c) shows a closeup with a perfectly intact surface and atomic resolution. To analyze the lattice parameters from the STM images the fast Fourier transform (FFT) of several different STM images was calculated and the lattice vectors  $\vec{a}$  and  $\vec{b}$  were deduced from their reciprocal counterparts  $\vec{a}^*$  and  $\vec{b}^*$ . For the image in a) the FFT is shown in b) with square root weighting and a 2D-Gauss background subtraction to highlight weaker features. The main reciprocal lattice vectors are clearly visible (indicated by arrows). The analysis produced values of  $a_1 = 6.44(3) \text{ \AA}$  and  $a_2 = 4.56(3) \text{ \AA}$ , where the uncertainty is the standard deviation. This is in good agreement with bulk measurements of the lattice constant [205, 211]. Slight deviation from the previously reported values arise from minor piezo calibration errors as well as drift, especially along the slow scanning axis.

When looking at the shape of the protrusions in c) one can see that they exhibit a slightly oval shape. Furthermore, a unit cell contains only one protrusion, while the unit cell

<sup>1</sup>An additional STM image of the vacancies and adatoms can be seen in the appendix in Figure C.1b

## 6. Structural and Electronic Properties of the FeSi(110) Surface

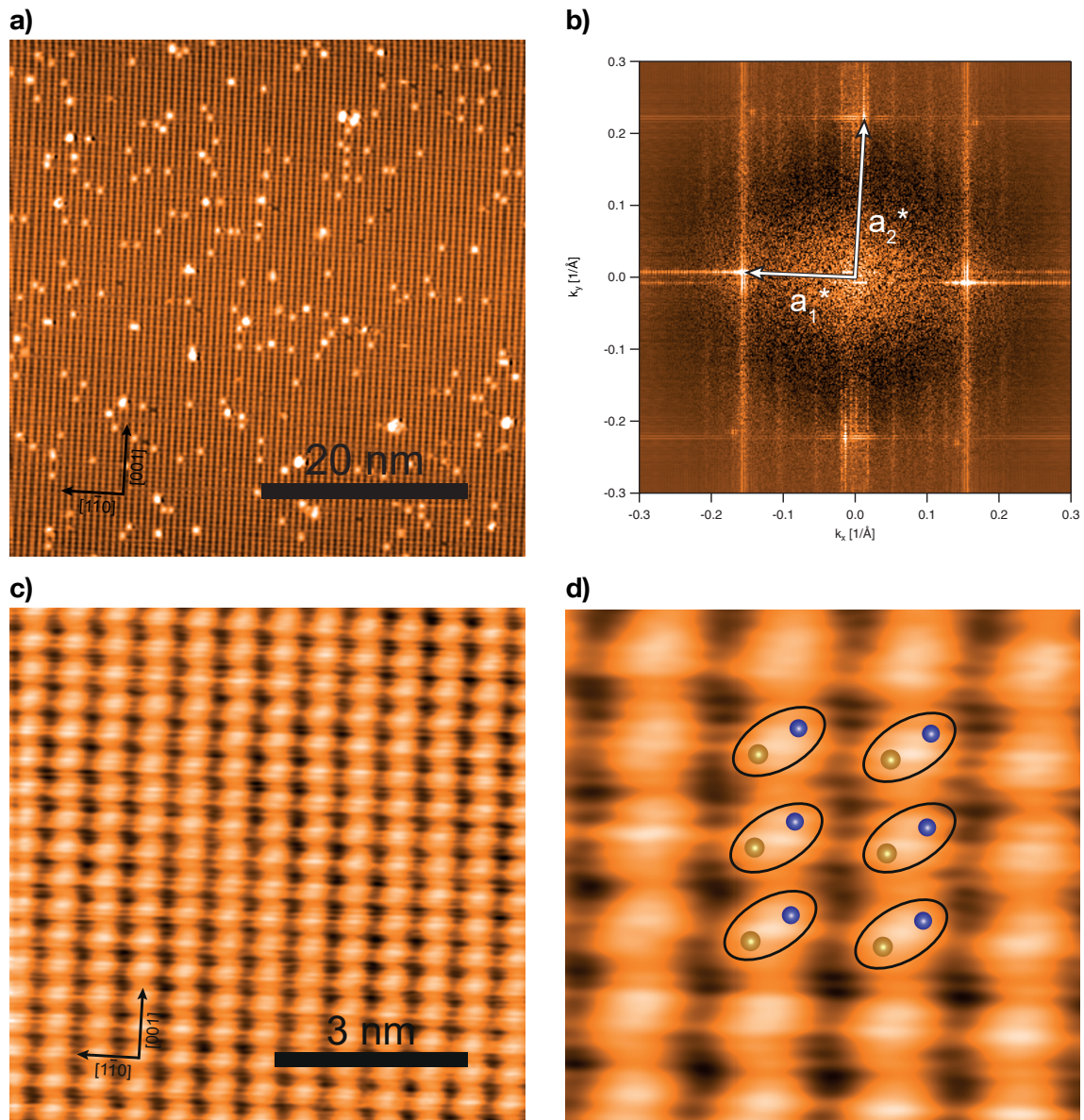


**Figure 6.3.:** **a)** Constant current STM image of the FeSi(110). The singular protrusions are associated with adatoms. ( $I_T = 100$  pA,  $V_B = 1$  V) **b)** FFT of **a)** with the reciprocal lattice vectors marked by arrows. **c)** High resolution STM image on FeSi(110). ( $I_T = 100$  pA,  $V_B = 1$  V) **d)** Enlargement of **c)** with an overlay of a presumed surface termination. Because the protrusions are rather large and oval, two atoms are assumed to correspond to individual protrusions.

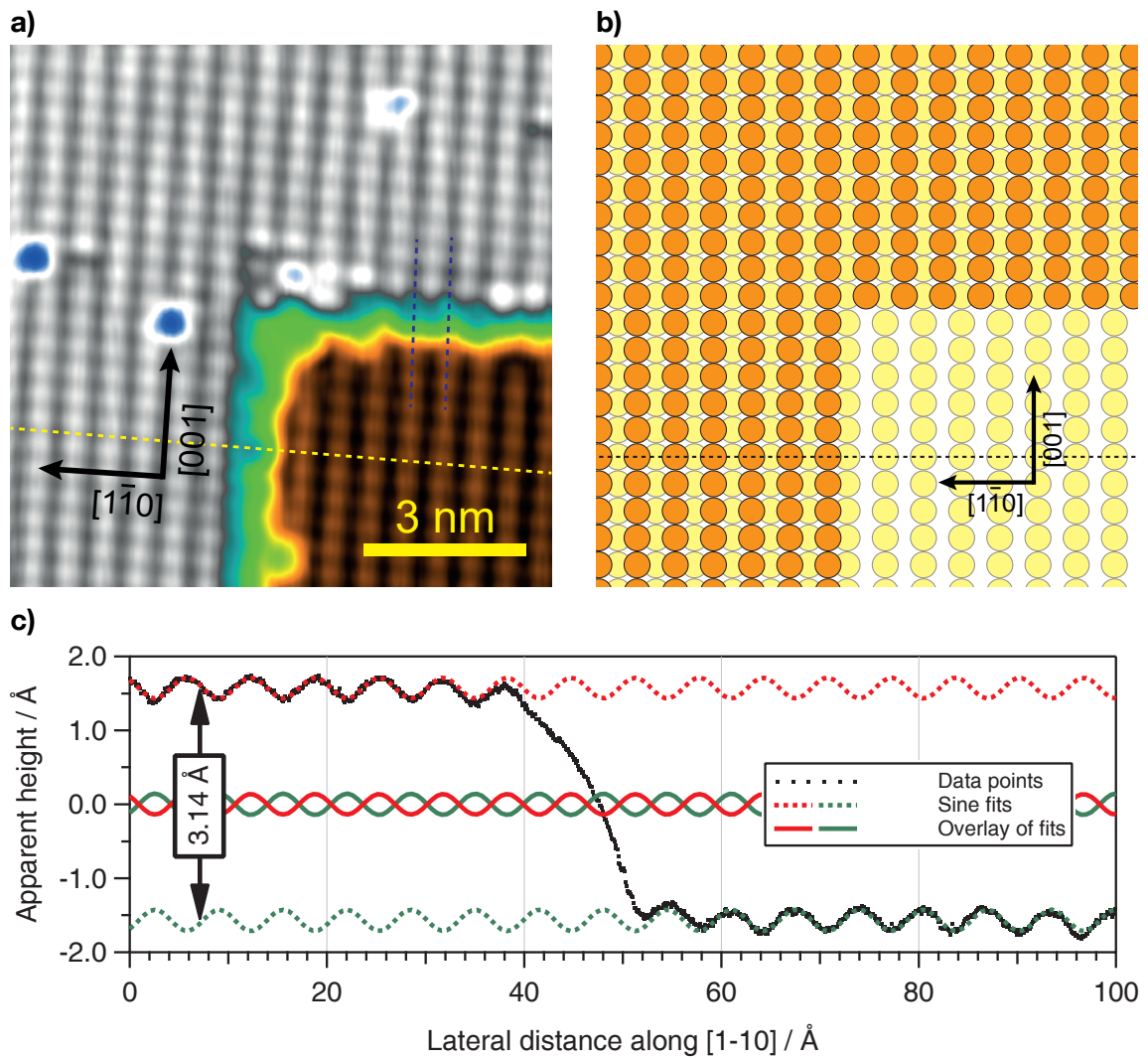


**Figure 6.4:** **a)** Constant current STM image of a step edge on FeSi(110). Printed in pseudo colors to allow good contrast on both terraces. ( $I_T = 1 \text{ nA}$ ,  $V_B = 200 \text{ mV}$ ) **b)** Model of the registry of both terraces. Note that the circles are a representation of the STM contrast, rather than any specific individual atoms. The dashed line indicates a representative spot for the line profile (*cf.* c)) in a). **c)** Line profile from a) (yellow dashed line). The lattice was fitted with sine functions on each terraces to show their shift by half a unit cell.

## 6. Structural and Electronic Properties of the FeSi(110) Surface

---

contains eight atoms, as discussed above. There was no significant change in contrast when going to different bias voltages, especially in the positive regime. STM images acquired at different voltages are shown in the appendix in Figure C.2. We propose the presence of at least two atoms responsible for the contrast, as illustrated by the overlay in Figure 6.3d. As will be discussed later, this is one of the possible terminations of the (110) surface and fits the data nicely.

To gain deeper insight to the surface termination, STM images of adjacent step edges were investigated. Such a step edge is shown in Figure 6.4a. The contrast is in pseudo colors to enhance the visibility of the surface registry on both terraces. The small terrace lies lower than the big one. To visualize the connection between the surface structure of adjacent step edges the line profile in 6.4c was taken from a) along the  $[1\bar{1}0]$  direction, as indicated by the dashed yellow line. There is plenty of information to extract from that: First, the apparent height difference is measured to be  $3.14 \text{ \AA}$ , which is very closely corresponding to the size of half a unit cell along the  $[110]$  direction ( $3.18 \text{ \AA}$ ). Second, the protrusions of the surface show a shift of half a unit cell with respect to each other. To guide the eye both terrace profiles were fitted with sine functions (dashed in red and green) that are additionally printed on top of each other in the middle of the figure (solid red and green) to emphasize the shift. The apparent height of the step edges remains the same, when multiple steps are present as can be seen in the appendix in Figure C.1a.

A close look on the dashed yellow line in a) also shows that the protrusions are collinear along  $[1\bar{1}0]$ . Due to the shift along that direction, the opposite is true for  $[001]$ , as indicated by the dashed blue lines, where the displacement by half a unit cell is clearly visible. For better understanding the extracted information is visualized in Figure 6.4b. The sketch shows a schematic representation of the STM image in a). Though the positions of the circles are in correspondence with the periodic lattice of the (110) surface, they do not represent any specific atom, since the origin of the contrast is still unknown. Nevertheless, the shift by half a unit cell is validated as well as the height distance of half a unit cell in the  $[110]$  direction.

To interpret the data further and assess its relevance for the determination of the surface termination, the individual cleavage possibilities of the (110) surface will be discussed. As before we will use the experimental values for the FeSi single crystal from Watanabe *et al.* [205]. Due to the complex B20 crystal structure (*cf.* section 6.2) and the resulting multitude of possible surface terminations the identity of the outmost surface atoms is a nontrivial question. In the beginning of this discussion we will disregard surface relaxation processes and assume a bulk truncated crystal. Later on, DFT calculations will be presented.

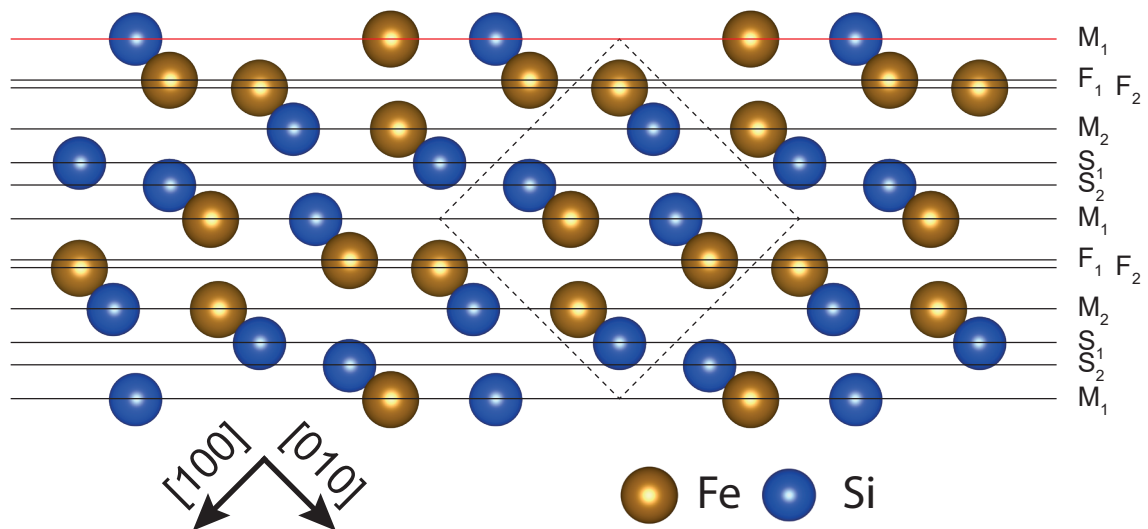


**Figure 6.5.:** Possible surface terminations of FeSi(110). View along [001]. The dashed square indicates the unit cell. The distances are summarized in Table 6.1.

In Figure 6.2b the unit cell of the (110) truncated bulk plane was already shown. The depicted case has two atoms per unit cell on the surface: One Fe and one Si atom, each of species 1 (*cf.* Figure 6.1b). The other possible atoms are shown in shallow colors behind them. LEED will always produce the rectangular reciprocal unit cell for FeSi(110) and the choice of the surface termination in the sketch is therefore completely arbitrary. In STM however, the surface termination will directly influence the LDOS of the surface and hence the STM signal. While Figure 6.2b clearly shows the (110) unit cell, it is a rather bad choice to visualize the specific surface termination. Therefore the lattice planes are shown as a sideview in Figure 6.5, *i.e.* along [001].

For simplicity, the top plane (red line) will be defined as the origin, though going from the bottom to the top would be completely equivalent. Following the nomenclature of Krajčí *et al.*, the planes are labeled according to their composition of either pure iron or silicon ( $F_i, S_i$ ) or a mixture of both elements  $M_i$  [206]. The unit cell is marked by the dashed square and it takes 12 planes to go all the way through it along the [110] diagonal. However, the planes are repeated after the sixth, with the exclusion that they are shifted by  $\vec{a}_1/2$ , *i.e.* 3.18 Å along  $[1\bar{1}0]$ . Otherwise, the planes are completely equivalent, hence their numbering repeats after these six planes. The periodicity of this "reduced" repetition is also 3.18 Å.

This is a strong indication that the terraces of the (110) surface are separated by six individual cleavage planes (*i.e.* surface terminations), because it nicely fits the measured

## 6. Structural and Electronic Properties of the FeSi(110) Surface

Plane	location	distance to next plane	
		higher	lower
M1	0.00	$d_{M1S2} = 0.60$	$d_{M1F1} = 0.73$
F1	0.73	$d_{F1M1} = 0.73$	$d_{F1F2} = 0.14$
F2	0.86	$d_{F2F1} = 0.14$	$d_{F2M2} = 0.73$
M2	1.59	$d_{F1M1} = 0.73$	$d_{F1M1} = 0.60$
S1	2.19	$d_{S1M2} = 0.60$	$d_{S1S2} = 0.39$
S2	2.58	$d_{S2S1} = 0.39$	$d_{S2M1} = 0.60$
M1	3.18	$d_{M1S2} = 0.60$	$d_{M1F1} = 0.73$

**Table 6.1.:** Positions of the FeSi(110) surface terminations along the [110] direction and their distances with respect to each other. Plane labels refer to Figure 6.5. All values in Å.

apparent height of 3.14 Å, as mentioned above. Together with the displacement by half a unit cell along  $[1\bar{1}0]$  the picture becomes even clearer, as only the separation by six planes allow for this shift. The slight mismatch from the bulk distance is most likely due to small piezo calibration errors.

So far we assumed a bulk truncated crystal structure on the surface, but a relaxation of the surface geometry might just as well be present. Unfortunately, studies of B20 single crystal surfaces show very different results for individual systems. For PdGa( $\bar{1}\bar{1}\bar{1}$ ) it was found that the surface termination is completely bulk truncated, but the arising surface terminations strongly depend on the annealing temperature of the surface [212]. On the other hand, on AlPd DFT studies showed a strong change of the interplanar distances, depending on the orientation of the surface [206]. In both studies no surface reconstructions occur. Interestingly, the minimum surface energy was oftentimes obtained for high corrugations, which is assigned to the covalent character of the B20 structure [213]. Since in our study we observed an apparent height that matches our proposed bulk distance for the planes, we rise the assumption of either a bulk truncated (110) surface or rather weak surface relaxations.

The actual surface termination, *i.e.* which plane actually contains the outmost atoms, can not be determined directly from the STM measurements. This is because neither individual atoms are resolved, nor is STM capable to determine their chemical identity in this case, opposing to previous STM studies on alloys [214]. As mentioned before, from our STM measurements we saw rather big protrusions with a slight oval shape. Therefore, we assume more than one atom per unit cell in the termination plane which makes the planes  $M_1$  or  $M_2$  possible candidates. They are very similar to each other, just differing

in the mirrored orientation of the long axis of the Fe-Si pair. But since the protrusions observed in STM have a homogeneous contrast and the type of B20 chirality is unknown they are completely interchangeable without further calculations, as the direct chemical environment can influence relaxation processes and surface energies. The distances of the individual planes are listed in table 6.1, which reveals that the planes  $F_1$  and  $F_2$  are just separated by 14 pm. They could therefore merge into one and represent the surface termination. Because the lateral Fe-Fe distance is rather low compared to Fe-Si, one would expect a rather sharp protrusion in the STM image, which is why we still propose the M planes as the most probable termination planes. To gain more confidence in this matter, we performed DFT calculations for the different surface terminations, which shall be discussed below.

### 6.3.2. DFT calculations

The DFT calculations were provided by Dr. Ari P. Seitsonen<sup>2</sup>. We performed total energy calculations using DFT [215] within the Kohn-Sham formalism and the generalized gradient approximation (DFT+GGA) [216] using the *Quantum ESPRESSO* code [217]. The bulk lattice constant was calculated initially and amounts to 4.4508 Å. We used the same nomenclature as for the STM analysis above (*cf.* Figure 6.5). For the calculations we used a slab of 54 atoms. STM simulations were modeled with the Tersoff-Hamann model (*cf.* section 2.1.2) using an *s*-wave tip [64].

#### Surface energies

In accordance to our considerations in section 6.3.1 we performed calculations on the surface terminations  $M_1$ ,  $M_2$ ,  $F_1$  and  $F_2$  and disregarded the purely Si-terminated cleavage planes. In order to have the same surface terminations on both sides of the slab it has to be non-stoichiometric for the  $M_1$ ,  $M_2$  and  $F_1$  resulting in Fe-Si atomic composition of 26/28, 28/26 and 25/24, respectively. We also calculated a stoichiometric slab of  $M_1$  on one,  $M_2$  on the other side, denoted  $M_1+M_2$ , but the surface energy was averaged from the individual terminations for this case. We discovered that the energy of some terminations is considerably lower if spin-polarization of the electrons is allowed; these calculations

<sup>2</sup>ENS, Paris, [https://www.chimie.ens.fr/?q=pasteur/pct/Ari\\_Paavo\\_Seitsonen/bio](https://www.chimie.ens.fr/?q=pasteur/pct/Ari_Paavo_Seitsonen/bio)

## 6. Structural and Electronic Properties of the FeSi(110) Surface

---

are denoted with "sp". The surface energy  $\gamma$  is defined as

$$\gamma = (E^S - N_{Si}^S \mu_{Si} - N_{Fe}^S \mu_{Fe}),$$

where  $E^S$  is the total energy of the slab,  $N_i^S$  are the number of atom in the slab of species  $i$  and  $\mu_i$  represent the corresponding relative chemical potentials.

In non-stoichiometric cases there is a complication: We do not know the relative chemical potentials  $\mu_{Fe} \leq E_{coh,Fe}$  and  $\mu_{Si} \leq E_{coh,Si}$  of the materials, only that they are smaller than the corresponding cohesive energies and thus we have an unknown parameter in our evaluation. The two are related via  $\mu_{Fe} + \mu_{Si} = E_{coh,FeSi}$ , where  $E_{coh,FeSi}$  is the cohesive energy per formula unit of FeSi. The value depends on the growth conditions, which was already discussed previously for the B20 compound AlPd [206]. Depending of a Si-rich or Fe-rich sample the relative chemical potential will be shifted. We use the  $\mu_{Fe}$  here as the unknown. It is bound by the limiting cases

$$E_{coh,FeSi} - E_{coh,Si} < \mu_{Fe} < E_{coh,Fe}$$

In our case this sets the borders of the relative chemical potential to:

$$-5.88 \text{ eV} < \mu_{Fe} < -4.39 \text{ eV}.$$

In Figure 6.6 the calculated surface energies  $\gamma$  for the different slab terminations are shown. The x-axis shows the relative chemical potential of Fe to account for slight variations in the overall composition, as discussed above. Please notice that the case M1+M2 is calculated only in the non-spin-polarized case. That this line crosses at the same point as the independent calculations M1 and M2 gives us confidence that the slabs (54/58 atoms) are thick enough, as otherwise one would expect a substantially larger deviation. The calculations that allow for spin-polarization of the electrons show a lower surface energy as their non-spin-polarized pendants, especially for the M1 case. Overall, the two sp versions of M1 and M2 are lowest in energy, though depending on the  $\mu_{Fe}$ , one is more energetically favorable than the other.

### Structural models

In the following the DFT calculated structural models are presented. Due to the results from the surface energy analysis we deem the M1sp and M2sp terminations to be most



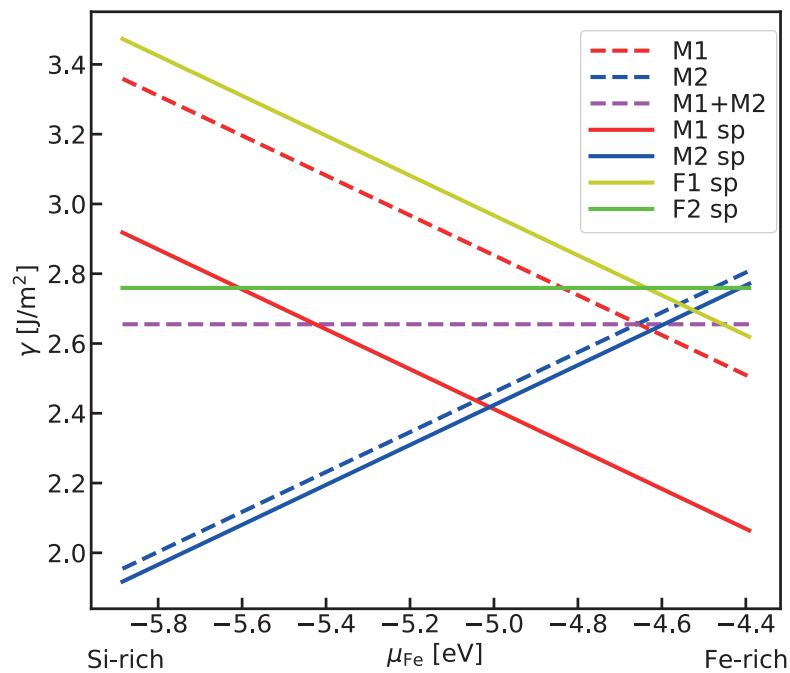


**Figure 6.6.:** Surface energies of the different terminations (cleavage planes) of FeSi(110) in dependence of the relative chemical potential. For some terminations this parameter is unknown due to non-stoichiometric slabs and depends on the growth conditions of the crystal. Calculations including spin polarization are denoted as "sp".

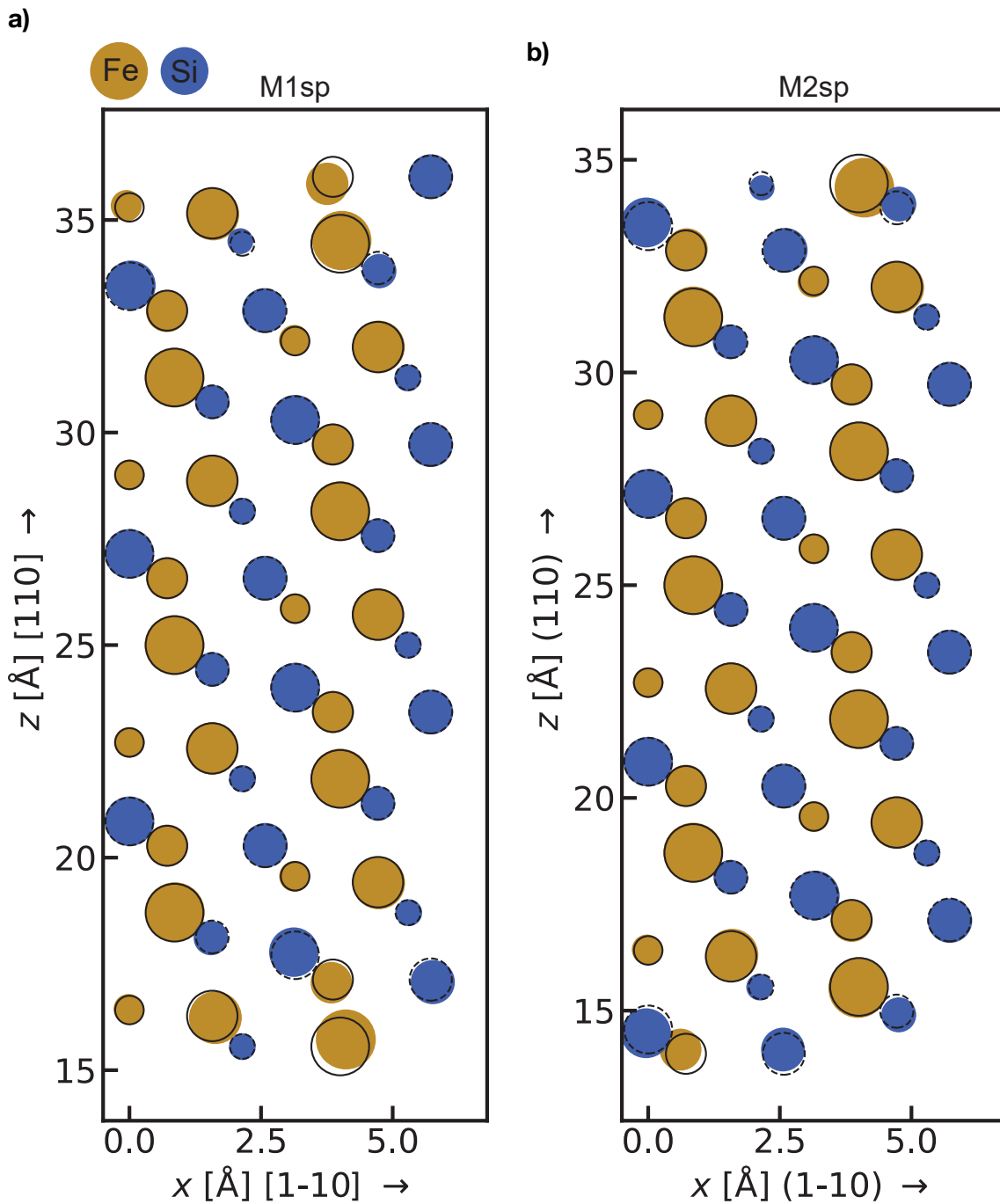


**Figure 6.7.:** Structural models from DFT calculations of different terminations of the FeSi(110) surface (*cf.* Figure 6.5). Spin polarization of electrons was allowed. Black circles represent the unrelaxed positions (solid for Fe, dashed for Si), whereas colored spheres show the relaxed structure and the sizes account for their distance to the viewing plane (100). **a)** M1 **b)** M2

likely present. Structural models of M1, M2 and M1+M2 can be found in the appendix in Figures C.5 and C.7, respectively. Figure 6.7 shows the terminations as a sideview along the [100] direction. Hollow spheres with black contours represent the initial (bulk) positions of the atoms with solid and dashed lines for Fe and Si species, respectively. After relaxation the atoms take the positions indicated by the colored circles using brown for Fe and blue Si as in Figure 6.5. Additional spacial information is presented by the size of the markers indicating their position along the [100] direction. The biggest species are in the paper plane and get smaller the further they lie behind the paper plane in said direction.

The slabs contain 54 atoms and are M1 or M2 terminated on both sides. We notice that with the spin-polarization included the structure changes much less from the bulk-truncated surface than without. The relaxations only take place on the surfaces, so we consider the slab as thick enough. While the Si atoms nearly stay in place, the Fe atoms move a little bit towards subjacent layers. Bearing in mind that Fe has a slightly bigger covalent radius than Si and that the crystal structure of FeSi has a substantially covalent nature (*cf.* 6.2 and ref. [213]) this directly results in a smoother surface. The absolute displacements of the outmost Fe and Si atoms towards the surface amounts to 0.1 Å.

### STM simulations

Further conclusions can be drawn by comparing the contrast observed in our STM measurements with simulations for the two most promising terminations M1<sub>sp</sub> and M2<sub>sp</sub>. Therefore, we calculated constant current STM simulations in the Tersoff-Hamann approximation for positive and negative biases. Figure 6.8 shows both terminations with M1<sub>sp</sub> on the left and M2<sub>sp</sub> on right. All images show a single protrusion per unit cell with slightly different shapes. The STM simulation of the M1 termination shows rather isolated protrusions compared to the M2 termination. Especially at positive bias the M2 termination shows a slight merge of the individual protrusions into rows along the [001] direction, which are oval shaped and rotated by  $\approx 45^\circ$ . The direction in which the protrusions are rotated depends on the chiral species. As illustrated in Figure 6.8e, this contrast strongly resembles the contrast we observed for positive biases. The STM image is shown on the left and the simulation image on the right with a smooth merge in the middle. For better visibility, the two outmost atoms of the M2 termination are shown as spheres. Though the simulation was done for a lower bias the contrast is very similar between simulation and experiment. As mentioned in section 6.3.1, we did not find qualitative changes in the contrast for different positive biases. Since the asymmetric shape of the individual protrusion

## 6. Structural and Electronic Properties of the FeSi(110) Surface

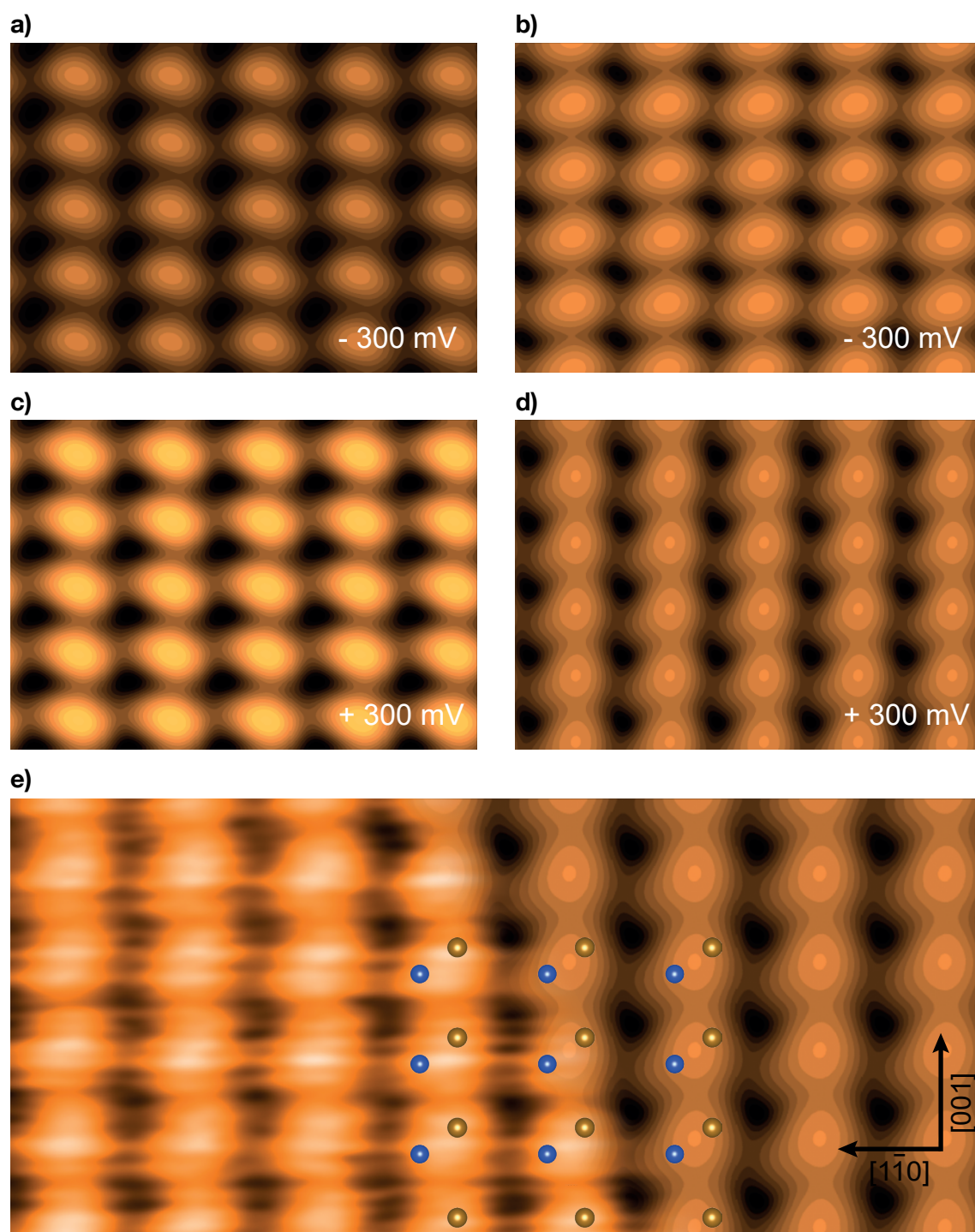


**Figure 6.8.:** STM simulations of the M1sp and M2sp structure at different biases. **a), c)** M1sp. **b), d)** M2sp. **e)** Overlay of STM image (as in Figure 6.3c) and the STM simulation in d).

sions in the simulation matches our STM data, the chiral species present in the sample is most likely of type A (*cf.* end of section 6.2). Would it be Type B, the image appearance should be mirrored along the [001] axis.

The M2 termination shows the lowest surface energy over a wide range of the composition dependent relative chemical potential. Furthermore, an allowance of spin-polarization in the calculations reduces the displacement of atoms during surface relaxation to a very small amount that is confined to the outmost atoms. High resolution STM measurements show one big protrusion per unit cell, which makes the M2 termination with its two top atoms a good candidate. Indeed, our STM simulations perfectly match the experimental observations and we therefore deem the M2 variant to be the preferred surface termination of FeSi(110). Additional information is given by the orientation of the asymmetric protrusions, making the Type A chiral species most likely to be present.

## 6.4. Scanning tunneling spectroscopy investigation of FeSi(110)

### 6.4.1. Tip characterization on Ag(111)

In order to investigate the electronic structure of FeSi(110) we performed scanning tunneling spectroscopy (STS) measurements. As mentioned in section 2.1.3, the tunneling signal is proportional to a convolution of the density of states (DOS) of both tip and sample. Therefore, it is crucial to ensure a metallic tip, with a flat DOS. For this case, the measured differential conductance is directly proportional to the DOS of the sample. In order to ensure this well-defined tip state, the tip was calibrated on a clean Ag(111) surface. Due to its well investigated surface state at  $E_{lit} = -63$  meV [218] it qualifies as an ideal reference system. After repeated cleaning cycles of Ag(111) with  $\text{Ar}^+$  sputtering and annealing at 500 °C tip conditioning was performed and the state of the tip was checked *via* STS. A typical spectrum of the Ag(111) surface is shown in Figure 6.9. The spectrum was recorded at 4.5 K and shows a sharp edge at the position of the onset of the surface state, while the rest of the spectrum shows no significant features and is reasonably flat. The surface state was measured at an energy of  $E_{sts} = -67.3$  meV. This is in reasonable accordance to the literature values [218–220]. To compensate potential offsets between tip and sample, a bias offset was applied to all measurements in a way that the minimum tunneling current is detected at zero bias.

## 6. Structural and Electronic Properties of the FeSi(110) Surface

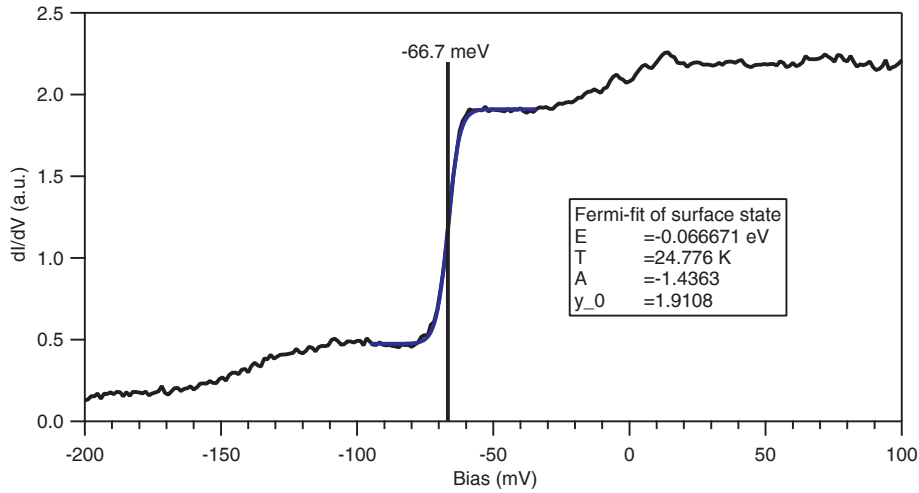


**Figure 6.9.:**  $dI/dV$  spectrum of Ag(111) after tip forming. The surface state is clearly resolved with its characteristic step-wise DOS from a nearly free 2D electron gas.

After the tip apex was confirmed to be metallic in the described way the tip was retracted and the FeSi(110) sample was inserted into the microscope. Subsequently, the tip was carefully approached to the surface to avoid any crash into the surface and maintain the apex state. Spectroscopy experiments on FeSi were then started directly without substantially moving the tip on the surface.

### 6.4.2. Pseudo-gap and in-gap state

As mentioned in section 6.1, FeSi features a so called "pseudo-gap" at low temperatures and the size measurements of the gap produced quite different results. To gain further insight into the nature of the gap, especially on the (110) surface, we performed STS experiments on FeSi(110). The spectra were acquired using the lock-in technique (*cf.* section 2.1.3) with modulation amplitudes (RMS) between 1 mV and 100  $\mu$ V. We identified 500  $\mu$ V to be a good compromise between signal-to-noise ratio (SNR) and energy resolution, as the spectral features did not get significantly sharper below that amplitude. If not mentioned otherwise, the measurements were performed at a temperature of 1.15 K. This results in a theoretical energy resolution of 0.85 meV, where the governing source of outsmearing originates from the 500  $\mu$ V modulation amplitude. Note that the actual energy resolution is also influenced by electronic noise effects of the measurement setup, so the resolution will be slightly smaller than the theoretical value. For further information please refer to section 2.1.3.

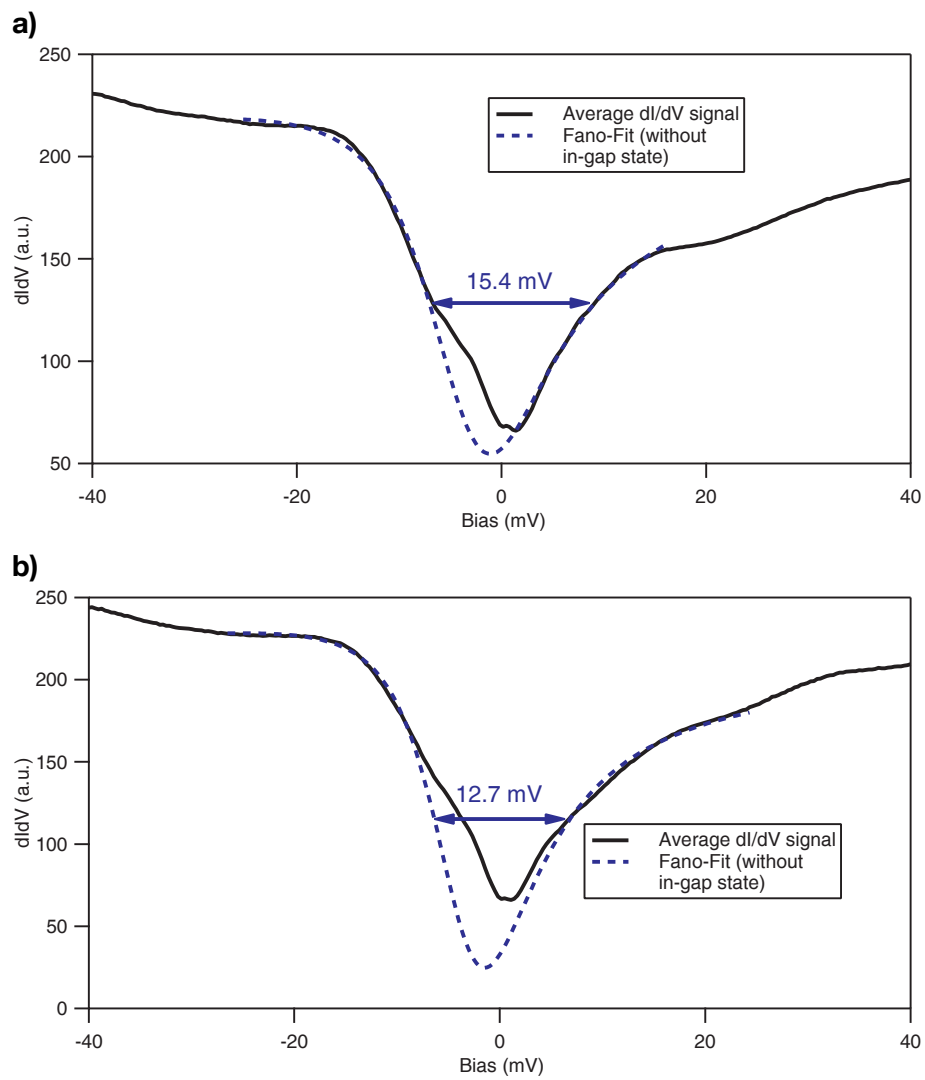


**Figure 6.10.:** **a)** STS of FeSi(110) taken at 4.5 K. The shape of the "pseudo-gap" is fitted with a Fano resonance [221]. The width refers to the  $\Gamma$  parameter in the Fano function. **b)** Same as a) but acquired at 1.15 K.

## 6. Structural and Electronic Properties of the FeSi(110) Surface

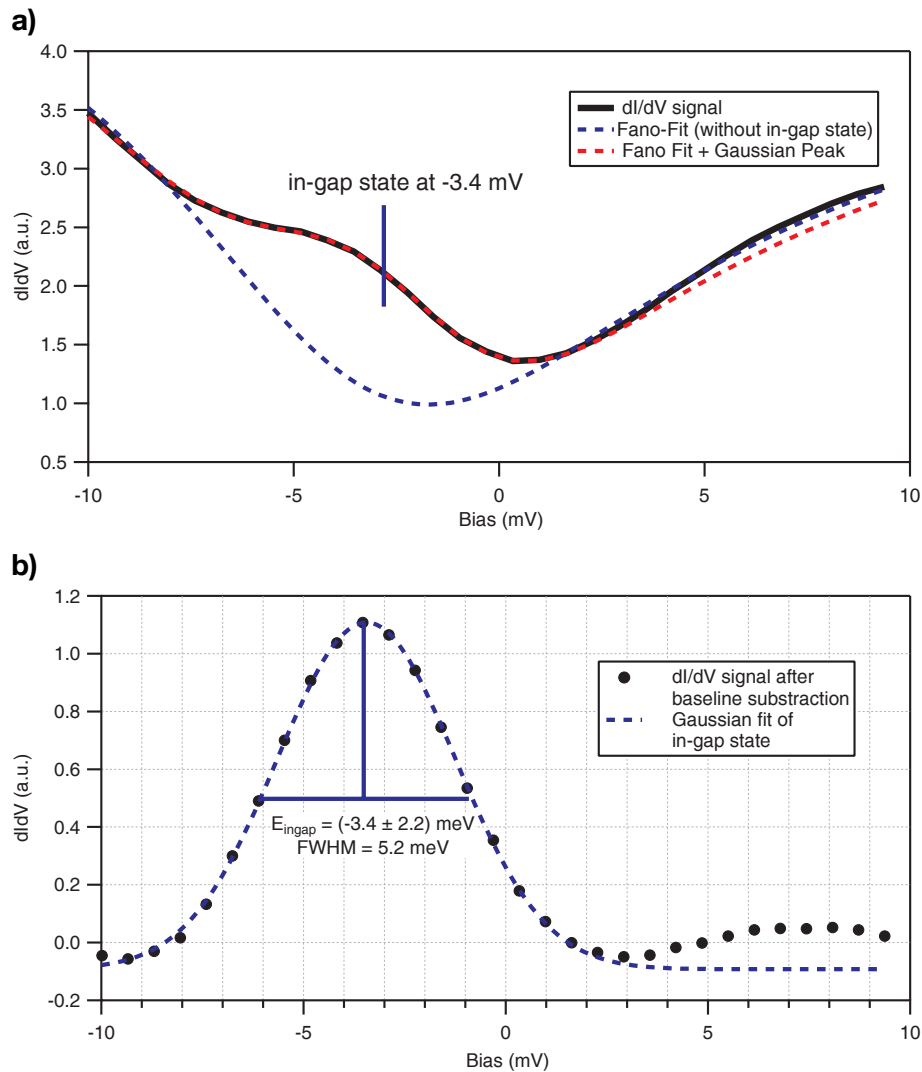


**Figure 6.11.:** **a)** STS of the in-gap state. The fits from 6.10 and b) were used to fit the baseline (dashed blue). **b)** Data points after subtraction of the baseline. A symmetric Gaussian of the in-gap state remains and is fitted in dashed blue. The sum of base-line and peak is shown in a) (dashed red).



## 6.4. Scanning tunneling spectroscopy investigation of FeSi(110)

A ST spectrum is shown in Figure 6.10a and b, being acquired at 4.5 K and 1.15 K, respectively. The spectra clearly resolve the "pseudo-gap" of FeSi(110). We did not find any significant change of the gap-size at the two different temperatures. The gap clearly shows a asymmetric shape, which requires a sophisticated analysis to determine the gap size. Previous photoelectron studies of the gap usually involved the fitting of a peak at the gap edge and multiplying the difference to zero energy [222–224]. Other STS studies either defined arbitrary criteria such as prominent kinks in the signal [225] or employed a Shottky barrier model to subtract a baseline and take the position of the maxima around the gap, though they experienced significant deviations from the model [226]. Our data did not show significant peaks around the gap, nor was the gap symmetric. Therefore we employed a Fano fit [221] to account for the asymmetric gap shape. The fits are indicated by the dashed blue lines. Note that the gap was fitted under exclusion of the in-gap data points below  $E_F$ , where an in-gap state can be observed, which will be discussed later. The fit function obeys the following equation:

$$f(E) = A \times \frac{(q + \epsilon)^2}{1 + \epsilon^2} + y_0 \quad \text{with} \quad \epsilon = \frac{E - E_0}{\Gamma/2}.$$

Here,  $q$  is the asymmetry factor of the Fano resonance,  $\Gamma$  the linewidth and  $E_0$  the center of the resonance.  $A$  is a scaling factor to account for the arbitrary magnitude of the STS signal from the lock-in amplifier and  $y_0$  represents a constant offset, because the DOS inside the "pseudo-gap" does never fully go to zero. The fit function models the flanks on both sides of the gap quite nicely and produces identical values for the asymmetry factor  $q$  for all measured spectra. The width  $\Gamma$  of the gap was measured to be 15.4 meV and 12.7 meV for 4.5 K and 1.15 K, respectively (blue arrows in Figures 6.10a and b). We repeated the measurements and the majority fits produced values around 15 meV for either temperatures. The shown spectrum for 1.15 K was mainly chosen because of the low SNR. Additionally, it has to be mentioned that a variation of the scaling factor  $A$  simultaneously to a change of  $\Gamma$  allows nice data modeling while having very different gap sizes. So due to empirical analysis we deem the 15.4 meV value to be more accurate. This value is significantly smaller than most previous measurements, where it was reported to have a size of 40 - 130 meV [157, 191, 222–232]. With one exception [222], all these studies were performed on *in situ* cleaved crystals, resulting in a multitude of occurring surface orientations. To our knowledge, this study is the first to show data acquired from a single crystal with a well-defined and determined orientation, as well as the first of an FeSi(110) surface. The orientation of the surface could be a reason for a smaller gap size. However,

## 6. Structural and Electronic Properties of the FeSi(110) Surface

---

it has to be noted here that the  $\Gamma$  parameter gives a much smaller value than the width that originates from fitting the gap with two peaks at each side of the gap. We deem a factor of roughly two to be a reasonable conversion constant between our Fano linewidth and the "classical" linewidth. Hence, our measured linewidth would account to around 30 meV in terms of previous findings. A possible explanation for our significantly smaller gap size might origin from the unknown transition in terms of direct or indirect band gap, as well as surface state effects on the (110) facet. Previous studies were either performed on different facets or polycrystalline samples. Band structure calculations were usually performed for the bulk (*cf. e.g. ref. [233]*).

The use of the Fano function is typically employed in Kondo-systems [234], but recent studies on the "Kondo-insulator"  $\text{SmB}_6$  showed that correlated electron effects also produced Fano shaped resonances in STS [177, 235]. Furthermore, studies of FeSi showed signs of correlated electron effects [197, 225, 236, 237]. It might be that similar mechanism are responsible for the agreement with the Fano resonance. We don't give further explanation to the origin of the shape, but rather use the Fano shape as an analytically reproducible tool to characterize the gap-shape and to use it as a baseline function for the fitting of in gap-states, as will be discussed now.

Comparing data and fits in Figure 6.10a and b, the interference of an in-gap state becomes evident. For better resolution the gap was probed from  $-10$  to  $10$  mV with a lock-in time constant of  $0.5$  s. The spectrum is shown in Figure 6.11a, where the solid black line represents the data. The shoulder between  $-5$  and  $0$  mv is clearly visible and gives clear evidence to the existence of an electronic state within the gap. However, it is not obvious where the peak is located exactly, because of the gap-shape as a non-constant background and because the height of the peak is rather low compared to the height of the gap flanks. Hence, a sophisticated baseline subtraction is required. As mentioned above, the Fano fit describes the shape of the gap very accurately. However, the high resolution spectrum in Figure 6.11a does not contain enough data points to allow a reliable gap fit. Therefore we took the values obtained from the gap fittings of the spectra above ( $q, \Gamma, E_0$ ) and only changed the scaling factor and the offset. The latter is necessary to account for the different spectroscopy settings. This fit is shown as the dashed blue line and describes the data very nicely. Note that the linewidth of the in-gap state influences the position of the gap minimum.

To determine the peak position the Fano baseline was subtracted from the data. The baseline corrected spectrum is shown in Figure 6.11b. The black dots represent the individual (processed) data points. Both Lorentzian and Gaussian fits were tried and Gaus-

sians worked best. The gaussian shape is in accordance to the assumptions above that the total energy resolution is limited by apparatus intrinsic noise rather than temperature and modulation effects. The peak is nearly perfectly symmetric and well described by the fitting curve, which is depicted by the dashed blue line. The fit produced an energy of  $-3.4(22)$  meV, where the uncertainty is given by the standard deviation calculated from the full width at half maximum (FWHM) of the fitting function. This was repeated for over 200 spectra, sometimes applying the fits to already averaged spectra. The final result is an energy value of  $E_{in-gap} = -3.50(240)$  meV for the in-gap state, where the uncertainty is calculated from the individually calculated standard deviations. The position and broadness of the peak was highly reproducible, independent to the probed energy range, always producing similar values. It even perfectly matches our preliminary results acquired from a different sample that was cut from the same crystal rod (not shown). The weak spectroscopic feature in the positive bias area in Figure 6.11b was neglected, because it might as well originate from a not perfect match of the Fano fit to the gap. The perfect symmetry of the peak undergirds the validity of the Fano fit for the gap-shape. For better visibility the Fano baseline plus the Gaussian fit is shown as the dashed red line in Figure 6.11a, nicely matching the data. The slight mismatch at the positive bias gap flank originates from the disregarded feature mentioned above. Possible reasons for the appearance of the in-gap state are the existence of a surface state that is located inside the energy gap, maybe even with a topological nature or effect of impurity bands. The latter could exist because of a not perfectly stoichiometric FeSi crystal as well as from impurities from the initial components, where especially Fe is known to have a relatively high concentration of impurity elements. To confirm or rule out any of this, further measurements with different crystals are required.

## 6.5. Conclusions

In conclusion, we produced an in-depth study of the FeSi(110) surface by documenting its structural and electronic properties. Our high resolution low temperature STM measurements gave structural insight to the FeSi(110) surface. The (110) orientation of the surface was confirmed by LEED and STM, which makes this study the first on a well-defined FeSi surface. By supporting DFT calculations we were able to give strong indications for the surface termination of the (110) facet, where the topmost comprise of one Fe and one Si atom. The surface relaxations calculated by DFT are minimal and strictly confined to the

## 6. Structural and Electronic Properties of the FeSi(110) Surface

---

surface. Due to minimal relaxation and a repetition of equivalent surface terminations after half a (110) unit cell, the height of a monoatomic step is identified to be 3.14 Å, according to STM as well as DFT. The atomic rows of adjacent terraces are shifted by half unit cell along  $[1\bar{1}0]$  and remain on top of each other in  $[001]$ .

After the structure was determined, STS measurements produced intriguing new results on the electronic structure around the Fermi level. We found an asymmetric, Fano-shaped gap of about 30 meV, which is substantially smaller than in most previous studies. Additionally, an in-gap state was resolved at an energy of  $E_{in-gap} = -3.50(240)$  meV. We employed a Fano fit for the gap shape, which nicely isolated the in-gap state as symmetric peak. This so far unreported state in the band-gap of FeSi could be the first evidence of a surface state. Nevertheless, further studies regarding the dependence of the state towards magnetic impurities are required to rule out impurity band effects and identify a possible topological nature of the state. Also, the influence of different surface orientations should be checked.

# 7



## Conclusions and Outlook



---

This thesis presented the investigation of metal-organic coordination chemistry on noble metal surfaces and oxide layers. Additionally, unprecedented insight to the structural and electronic properties of FeSi was given. The presented studies were carried out by means of UHV-based surface science utilizing STM and STS, accompanied by complementary approaches such as DFT, XPS and LEED.

In chapter 4, the surface induced self-assembly of TPA-Ho complexes and networks on Ag(100) was shown. By following a DFT assisted STM approach, two different structures were identified and structural models were deduced. They share several common features: Firstly, they are both chiral due to a rotation of the lanthanide-organic superstructure with respect to the substrate and a concerted rotation of  $53^\circ$  of the carboxylates. Secondly, both of them employ TPA molecules in the carboxylate state, which was achieved by surface induced deprotonation of the carboxyl groups. Thirdly, they show an eight-fold coordination to the Ho atoms, exploiting the high coordination number of lanthanides compared to classical metals such as Fe or Cu. The first structure consists of Ho-TPA complexes, where four TPA molecules coordinate to one Ho atom in a cloverleaf shape. The complexes form enantiomorphic islands of high lateral extend and surface coverage. On an increased Ho dosage during preparation, a second structure in form of reticulated metal-organic coordination networks can be fabricated. Here, the TPA molecules are coordinated on both sides to Ho atoms. They show limited lateral extent due to interfacial strain effects, which became apparent through DFT calculations. The results show a very promising attempt to robustly isolate single Ho atoms on the Ag(100) surface and investigate their magnetic properties.

Because Ho atoms showed a greatly enhanced magnetic anisotropy on MgO layers on Ag, chapter 5 presents a first attempt to transfer the supramolecular structures to MgO films on Ag(100). The growth of semi-epitactic MgO films was achieved and investigated by STM. STS experiments were carried out to unequivocally determine the chemical identity and thickness of the MgO layers. The adsorption behavior of pristine TPA on MgO was investigated and surface induced deprotonation was achieved. After the deposition of Ho on the surface the formation of metal-organic complexes at different annealing temperatures was investigated. In contrast to the experiments on the bare Ag(100), notable complex formation took place at a significantly higher temperature of 650 K. The complexes show a high resemblance to the cloverleaf complexes on the bare Ag substrate. From the STM images, a tentative adsorption model was deduced. Again, the complexes render an eight-fold coordinated adsorption scheme. Four TPA molecules in the carboxylate state coordinate to one Ho atom in the center. They are rotated by an angle of  $14.04^\circ$

## 7. Conclusions and Outlook

---

and adsorb with their phenyl rings on bridge sites, as deduced from the model. The experiments on MgO represent a first proof of principle study to show that the fabrication of Ho coordinated complexes on MgO is possible and enable further developments towards extended islands of said complexes. As a further step XMCD measurements of the complexes on Ag(100) as well as on MgO/Ag(100) would give insight to the magnetic properties of the Ho atoms and allow for the comparison with the experiments on isolated single atoms. Chapters 4 and 5 represent another step towards the fabrication of robust assemblies of single atom magnets on surfaces.

In chapter 6 the FeSi(110) surface was investigated by means of STM, STS and DFT. Unprecedented insight to the structural and electronic properties of the monocrystalline atomic flat surface was given. While previous studies provide no information on the atomic surface structure, we were able to fabricate well-defined surfaces of a single orientation. In the first part, the structural properties, especially the surface termination is investigated. We identified six possible surface terminations that repeat after half a unit cell in the [110] direction, *i.e.* 3.18 Å with a shift by half a unit cell along  $(1\bar{1}0)$ . Our assumption of the absence of a surface reconstruction is supported by LEED measurements as well as STM. We clearly observe the repetition of the terminations in the recorded apparent height of step edges and atomic resolution STM data shows the mentioned shift by half a unit cell along  $(1\bar{1}0)$ . We performed DFT calculations for the possible surface terminations and calculated the surface energies. We deem the M2 terminations as most likely, for it has the lowest surface energy for our case and the STM simulation is in excellent agreement with the observed contrast. Surface relaxations appear to be confined to the outmost atoms. After the structural analysis, high resolution STS experiments at 1.2 K were conducted. The "pseudo-gap" of FeSi(110) was clearly resolved, though it appears to be significantly smaller and asymmetric on the (110) facet compared to other FeSi studies. Our measurements show a gap size of about 30 mV. Additionally, we were able to give clear evidence of an in-gap state at  $E_{in-gap} = -3.50(240)$  meV. This state is so far unreported and could be the first proof for the existence of a surface state in FeSi(110). The next step will be to repeat the spectroscopy experiments on crystals with slightly differing stoichiometric compositions to rule out impurity bands as the origin for the state. Additionally we will perform Fourier transform scanning tunneling spectroscopy and look for 2D quasi-particle interference patterns to investigate a possible topological nature of the state.

In conclusion, two complementary approaches for new possibilities in on-surface electronics and spintronics were given. The first part showed the bottom-up fabrication of



---

possible single atom magnets in thermally robust framework on different substrate systems. In the second part, novel insight to astonishing electronic features of FeSi(110) was given, which points it out as a possible candidate for a topological material. By a combination of different techniques, namely STM, STS, LEED, XPS and DFT, a comprehensive scientific approach was conducted in order to give an as complete as possible view on the investigated systems.



## **Appendix A.**

### **TPA-Ho on Ag(110)**



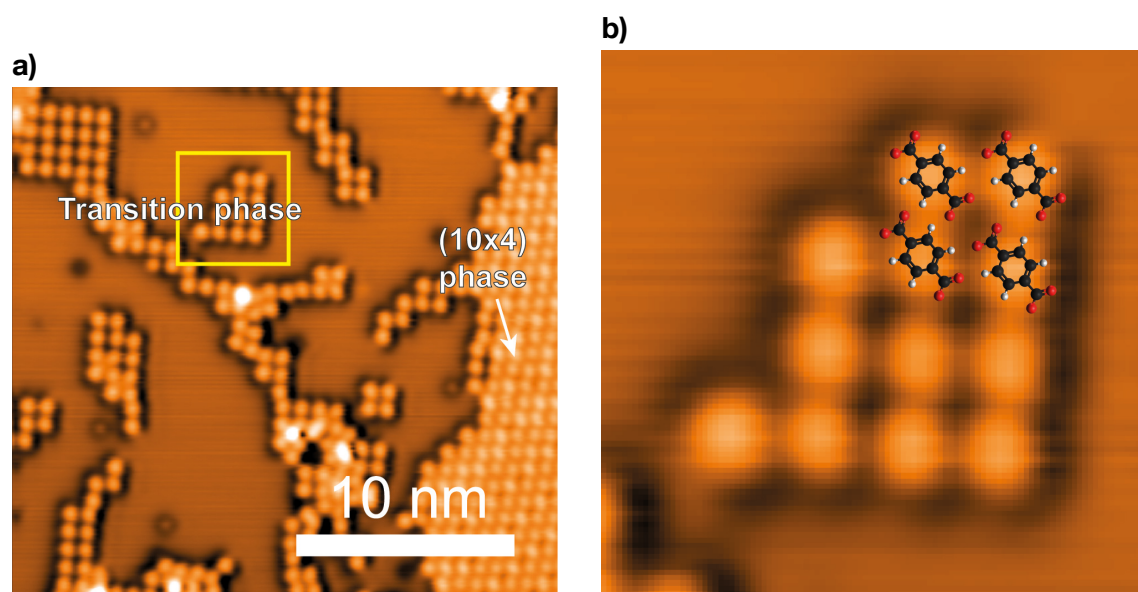
## A.1. Organic transition phase

Figure A.1a shows the organic transition phase that is formed by deprotonated TPA for low coverages. The phase exhibits a nearly quadratic unit cell of  $8.4(1) \text{ \AA} \times 8.2(2) \text{ \AA}$ , measured along the slow and fast scanning axis, respectively. The error is calculated from the standard deviation. The islands have no fixed angle in orientation with respect to the lattice and the distances measured do not show any obvious connection to the lattice vectors. Whilst the difference in the two directions could be drift, it is also likely that the unit cell is indeed not perfectly quadratic. One reason for this is the orientation of the carboxylates, whereby depressions on the edges indicate the deprotonated carboxyl groups (Figure A.1b). Hence, the molecules are all aligned in the same direction as integral TPA does on metal surfaces [128]. Since the deprotonated molecule is shorter compared to pristine TPA, it is more difficult to determine if the unit cell is quadratic or rhombohedral. Secondly, the distances between the molecules differ from case to case (even when measured in the same frame). Thirdly, the phase is growing in chains with a width of two to three molecules rather than extended islands. They also can have slight bends. A strictly defined unit cell would not allow this behavior. The fact that the phase only occurs in these small islands and smoothly connects to the precursor phase (c.f. Figure 4.1 in the manuscript) indicates it as being a transition phase between single molecules on the surface and extended islands of the precursor phase. Compared to inter-molecular interactions, the molecule-substrate interaction plays a more significant role for the formation of the full monolayer precursor phase, where in every other row the molecules turn by roughly  $90^\circ$  forming the T-facing structure of the precursor phase. Hence, the term transition phase is used.

## A.2. Chirality of Ho-TPA<sub>4</sub> complexes

## A.3. Ho-evaporator

The holmium used in the experiments was evaporated via a foil evaporator. A thin Ho foil (purity= 99.9%, Merck) is heated up by applying a high current, high frequency RF voltage. Due to water cooling of the evaporator, only the foil heats up and emits holmium atoms and clusters of high purity.



**Figure A.1.:** **a)** STM image ( $I_T = 100$  pA,  $V_B = 1$  V) of the transition phase (left) next to (10×4) precursor phase (right). The yellow square shows the area enlarged in (b). **b)** Enlargement of (a). The depressions on the molecules indicate the position of the carboxyl groups, revealing a parallel orientation of the molecules.

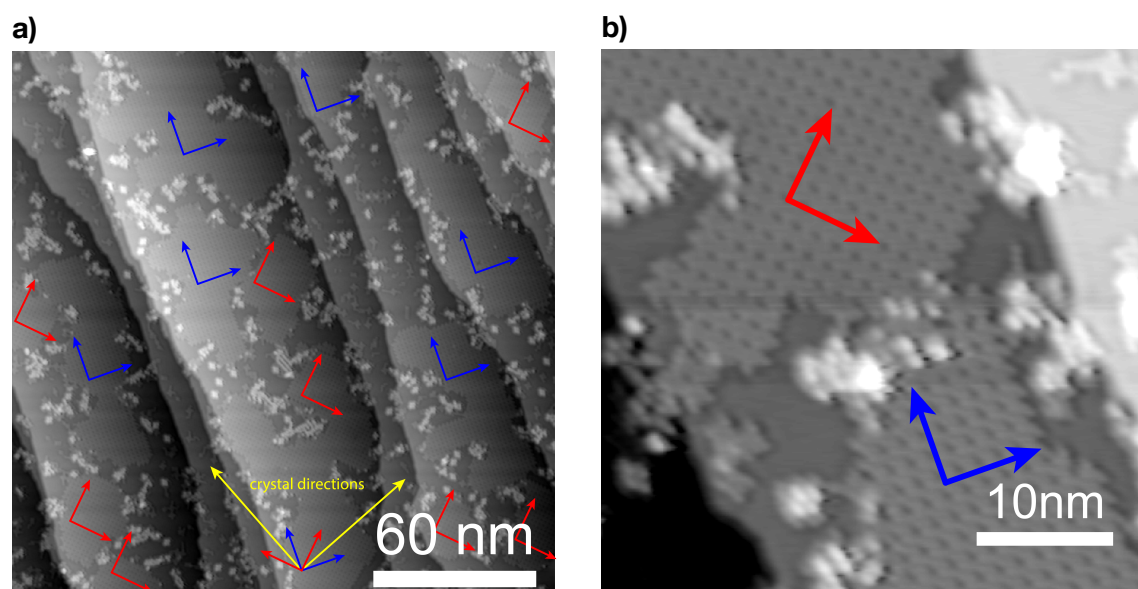


**Figure A.2.:** Constant current STM images showing islands of the cloverleaf phase. There are two directions of growth, indicated by the rectangle arrow pairs in blue or red.

## A.4. Holmium coverage definition

Since Ho is significantly bigger than silver, a full ML of Ho will contain less atoms than a full ML of silver. Additionally, the Ag(100) surface has a quadratic unit cell whilst Ho crystallizes in the hexagonal closed packed structure. This gives a density of 0.652 holmium atoms per silver atoms, assuming a full ML. All Ho coverages in this work refer to a full ML of Ho in the (0001) surface covering the same silver area with a (100) surface. The deposition parameters were calibrated via deposition of holmium on a Ag(111) surface fully covered with Hexakis(trimethylsilyl)ethynylbenzene (HEB), where holmium adsorbs as single atoms on the phenyl rings of the molecule and are easily countable.

## A.5. Drift correction

Since STM data has a slow and a fast scan direction, piezo drift will cause a distortion of the images with different magnitudes to each direction. It is essential to overcome this obstacle especially when measuring unit cell sizes of superstructures without having atomic resolution at the same time. A precise calibration of the piezos is obviously essential for corrected length scales of STM data, but the drift effect will nevertheless remain present at all times. A simple and reliable method is to rotate the scan directions by  $90^\circ$  and compare the distortions. While the calculation of the correction parameters is quite complicated manually, we used the MATLAB script from Ophus, Ciston and Nelson to calculate the corrected images [238].

## A.6. Determination of the U-value

The U-value was determined by optimizing the geometry of  $Ho[OAc]_3$  and determining the energetic difference between the occupied and unoccupied  $4f$  states. Then, the same system was simulated using DFT+U for different values of U and the optimal value determined via a linear fit as shown on the right in Figure A.3.

## A.7. Structural relaxation details

As mentioned in the main manuscript, the checkerboard structure exhibits a large strain as the metal support enforces a cell geometry upon the adsorbate. This is supported by

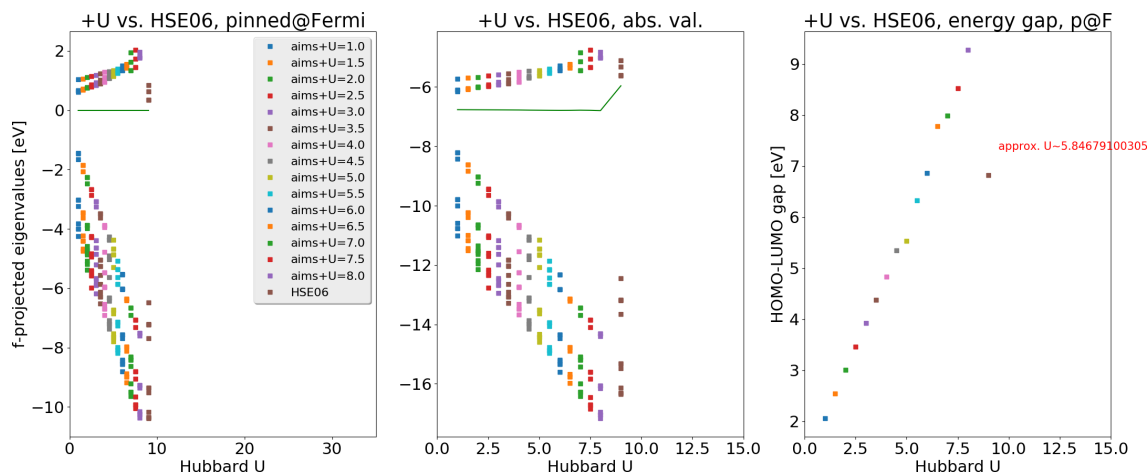


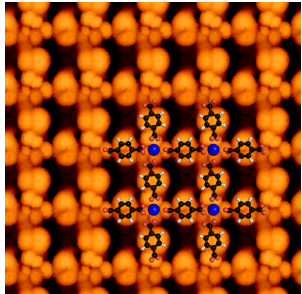
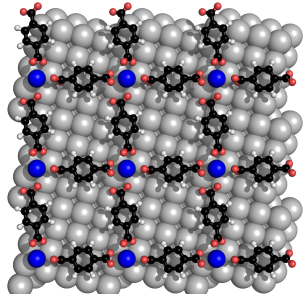
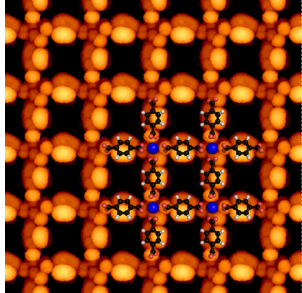
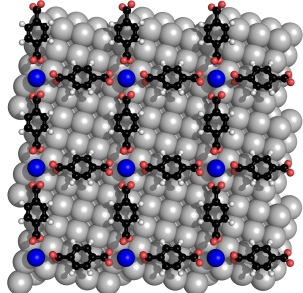
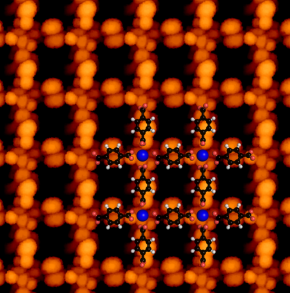
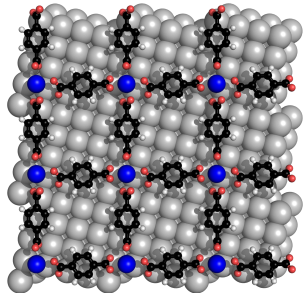
**Figure A.3.:** DFT+U screening for a suitable value to reproduce the energetic splitting between the occupied and unoccupied  $4f$  orbitals in the system. (fltr.: normalized to Fermi-level, absolute values, and the linear fit)

the experimental observation of only small islands and stripes of this particular bonding environment. The theoretical modeling of the geometry focused on two different arrangements, where the holmium-atom was located at the hollow (**H1**,**H2**) and bridge (**B**) site, respectively. Relaxation of the first layer of Ag-atoms was permitted. The main features of the experimental STM signature are reproduced by structural models **H2** and **B**. However, the structural model **H2** does not describe a strain-free structure as the largest forces observed exceed  $60 \text{ meV}/\text{\AA}$ . Furthermore, although only very small differences are present, the formation energy of structural model **B** is higher than the other two, hinting towards increased thermodynamic stability. The difficulty in assigning a structural model to the *checkerboard* structure supports the experimental observation of the preferred formation of the *cloverleaf* structure instead.

## A.8. Node bonding environment

The bonding of the carboxylate linkers to the holmium node follows the same motive as already reported for similar Gd-complexes [107]. Our DFT simulations predict in both observed surface-networks an eight-fold coordination with the carboxylate linker tilted by  $52.4 - 53.9^\circ$  (cloverleaf) and  $40.8 - 105^\circ$  (checkerboard) out-of-plane with respect to the linker backbone. The average bond distance of holmium and oxygen is  $2.4\text{\AA}$  (cloverleaf) and  $2.6\text{\AA}$  (checkerboard). A side-view of the bonding environment is given in Figure 4.5. Also shown in Figure 4.5 are the forces acting on the individual atoms in the non-



STM-simulation & overlay	structure	comments
<p><b>H1</b></p> 		<ul style="list-style-type: none"> <li>• holmium on hollow-site</li> <li>• <math>f_{max} &lt; 0.025 \text{ eV/\AA}</math></li> <li>• <math>\Delta E = 147.7 \text{ meV}</math></li> <li>• one TPA is only linked via one oxygen atom to the holmium-atom, which leads to a non-checkerboard pattern observed in the corresponding Tersoff-Haman signatures</li> </ul>
<p><b>H2</b></p> 		<ul style="list-style-type: none"> <li>• holmium on hollow-site</li> <li>• <math>f_{max} &lt; 0.060 \text{ eV/\AA}</math></li> <li>• <math>\Delta E = 144.3 \text{ meV}</math></li> <li>• In an unstable structure, both TPA molecules would link in a <math>C_4</math> symmetric fashion to the holmium linker atom. The system shown experiences forces of <math>60 \text{ meV/\AA}</math>.</li> </ul>
<p><b>B</b></p> 		<ul style="list-style-type: none"> <li>• holmium on bridge-site</li> <li>• <math>f_{max} &lt; 0.025 \text{ eV/\AA}</math></li> <li>• <math>\Delta E = 147.8 \text{ meV}</math></li> <li>• both TPA molecules are linked in a <math>C_2</math> symmetric fashion to the holmium linker atom. The system experiences remaining forces up to <math>25 \text{ meV/\AA}</math> and the STM signatures correspond to the experimental observation.</li> </ul>

**Figure A.4.:** The different models for the checkerboard structure considered in the DFT simulations.

equilibrium checkerboard-structure **H2** from Figure A.4. The arrows point away from the holmium node, suggesting that an equilibrium would only be reached by detachment from the metal center.

## **Appendix B.**

### **TPA-Ho on MgO/Ag(110)**



## B.1. Single monolayer of MgO

Under low magnesium deposition rates ( $T_{OMBE} = 400\text{ }^{\circ}\text{C}$ ) the growth of a single monolayer *i.e.*  $\approx 200\text{ pm}$  thickness can be observed. Figure B.1a shows a STM image of representative sample. The MgO grows mainly 2 ML thick, but on the edges small areas of 1 ML thickness can be observed. The thickness assumptions are supported by numerical  $dz/dV$  spectra, as can be seen in Figure B.1b. The single layer of MgO only produces a peak at around 2.7 eV, while the bilayer also features the Ag(100)/MgO interface state at around 1.9 eV. This is in accordance with previous findings [154]. The line profile in B.1c shows the thickness of the island as 410 pm and about half that height for the single layer separating the 2 ML island from the silver.

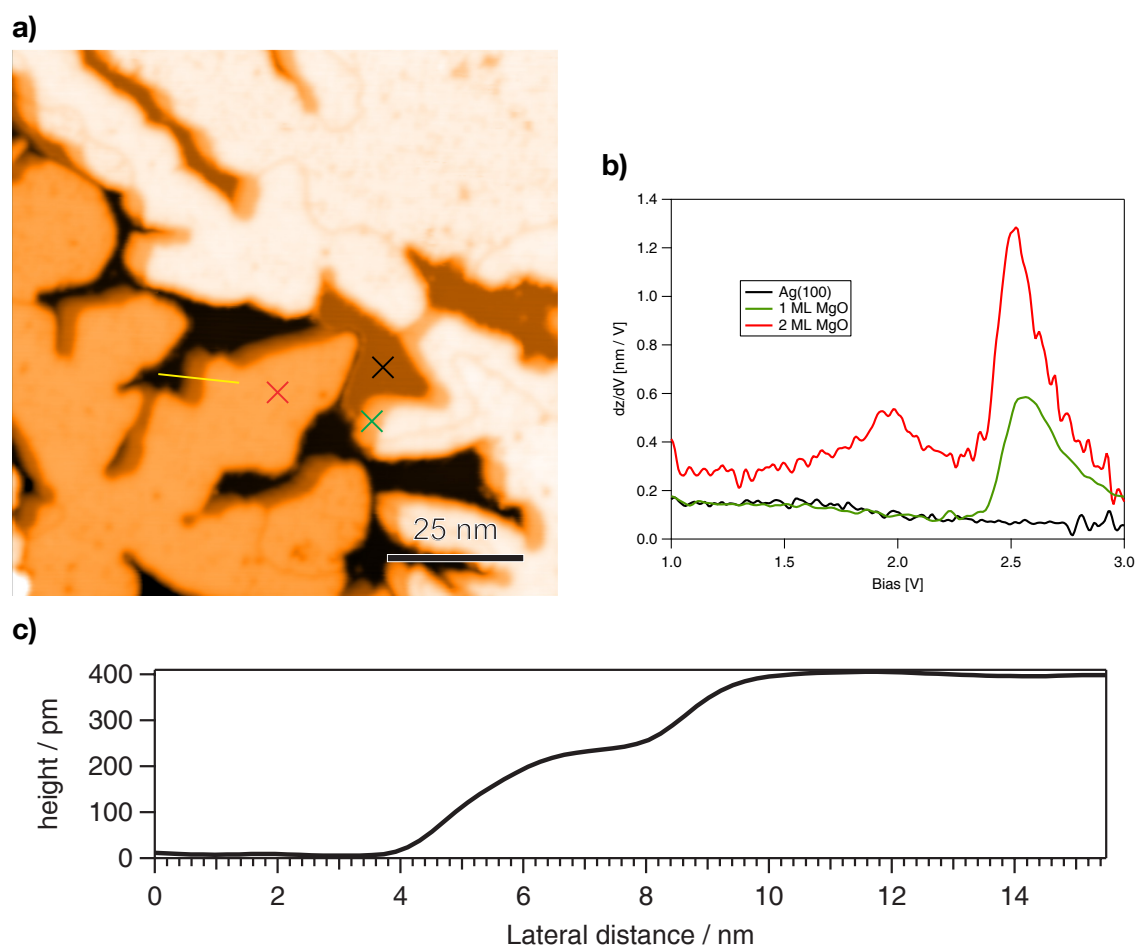


**Figure B.1:** **a)** Constant current STM image of MgO on Ag(100) ( $V = 3$  V). The small intermediate steps at the edges of the MgO are 1 ML MgO films. **b)**  $dI/dV$  spectroscopy at different positions of a), as indicated by the corresponding cross marks. **c)** Line profile along the yellow line in a) showing the thickness of 1 - 2 ML.

## **Appendix C.**

**FeSi**





## C.1. Additional STM data

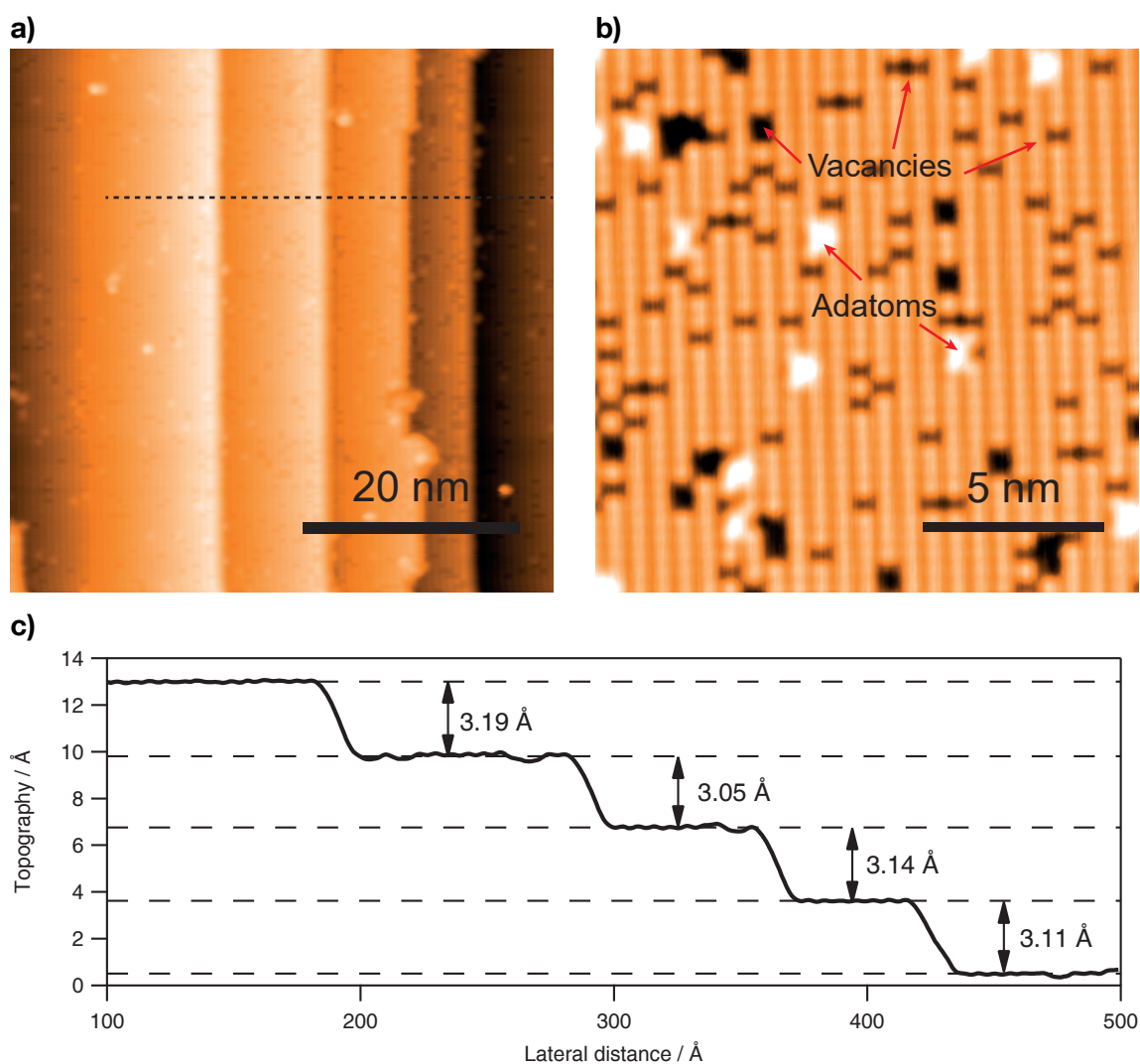


**Figure C.1.:** **a)** Constant current STM image of FeSi, showing multiple step edges. The black dashed line indicates the position of the line profile in **c)**,  $V_B = -1$  V **b)** Close-up constant current STM image of the sample in **a)** showing vacancies and adatoms,  $V_B = -0.5$  V **c)** Line profile containing multiple step edges and the height differences between them.

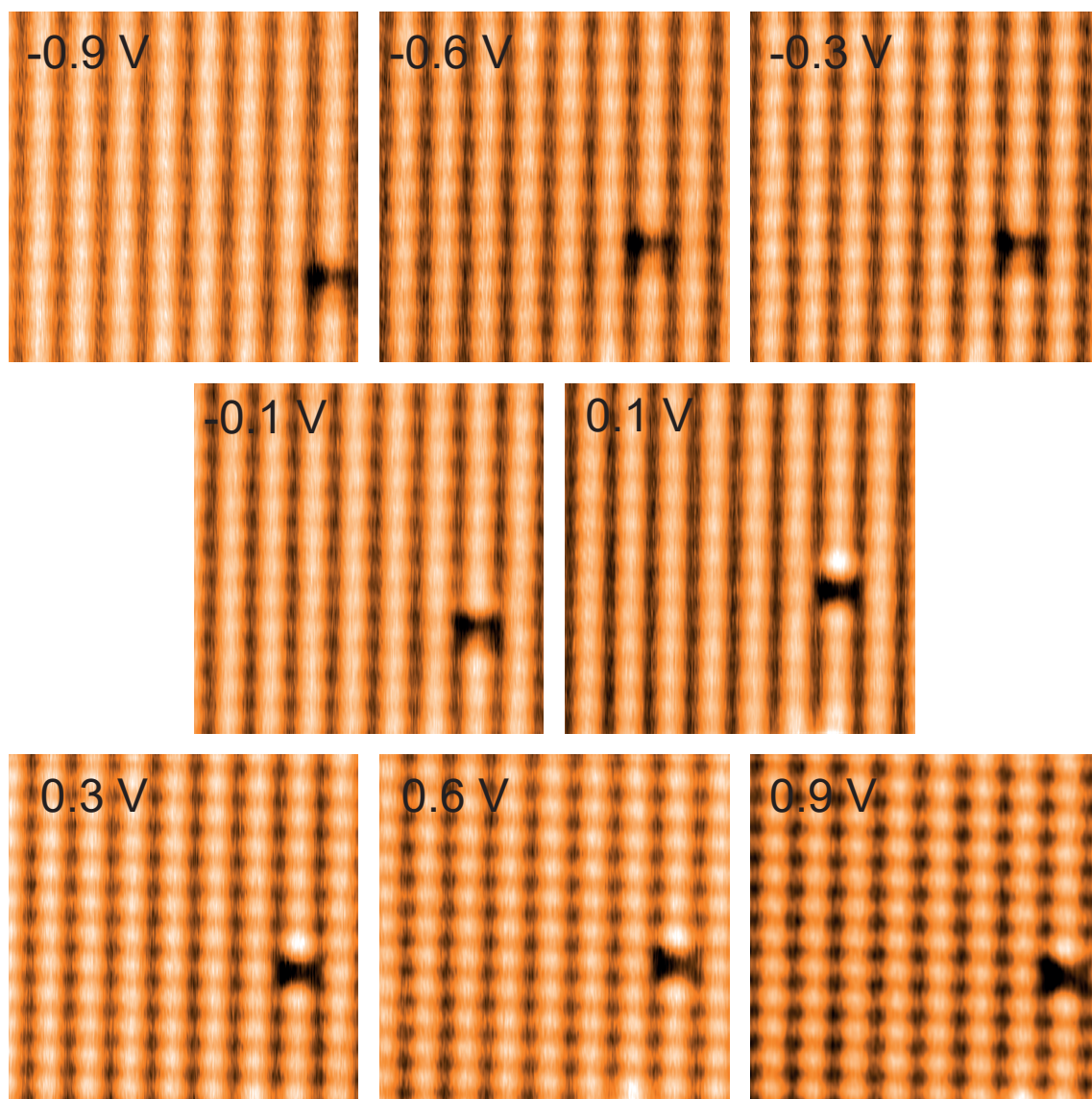


**Figure C.2.:** STM contrast of FeSi(110) at different bias voltages. The contrast looks very similar. Note that small changes in the tip termination have a much bigger influence on the contrast than the applied voltage. All images are 5 nm × 5 nm and recorded at  $I_S = 0.9$  nA

## C.2. XPS

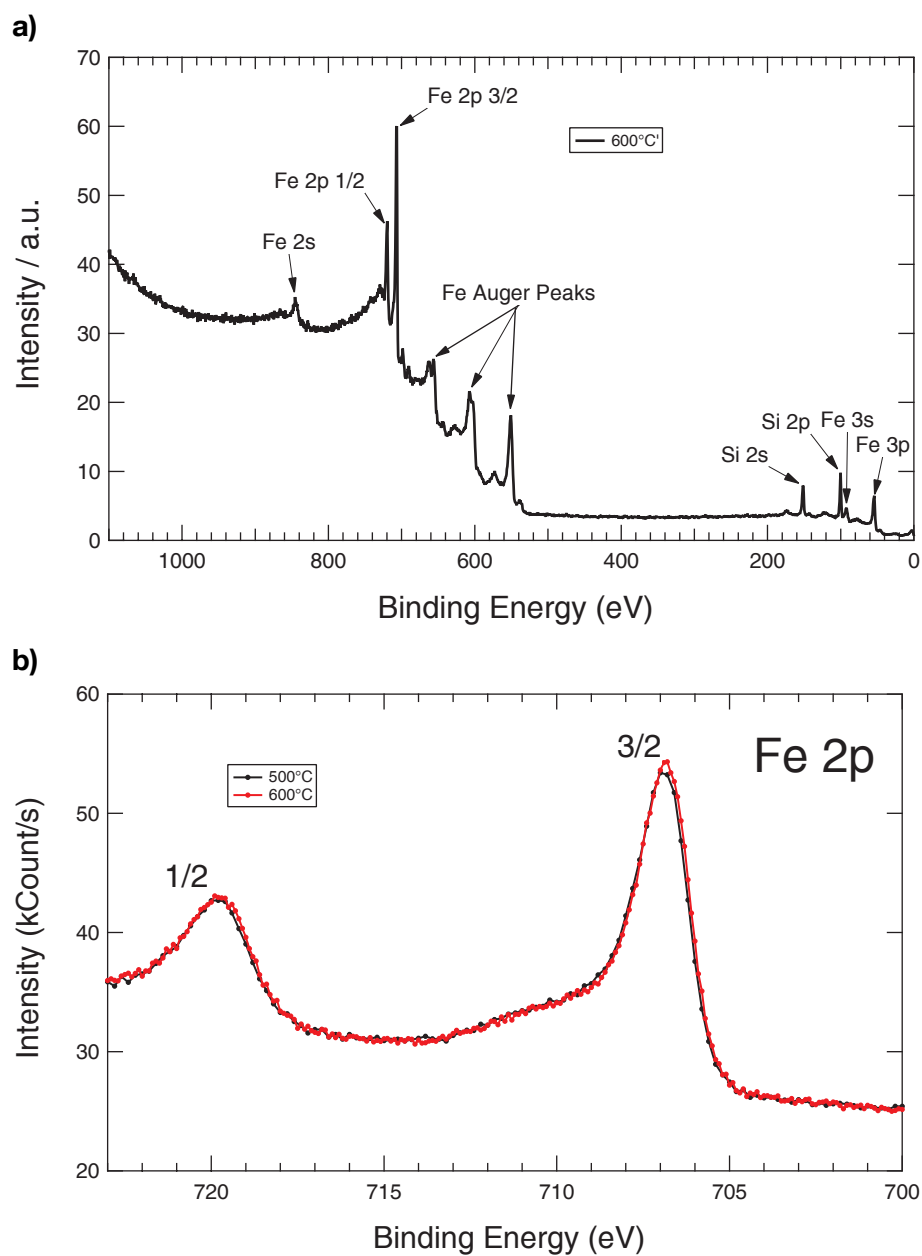


**Figure C.3.:** XPS of FeSi, sputtered and annealed at different temperatures. **a)** overview spectrum **b)** Fe2p peaks.

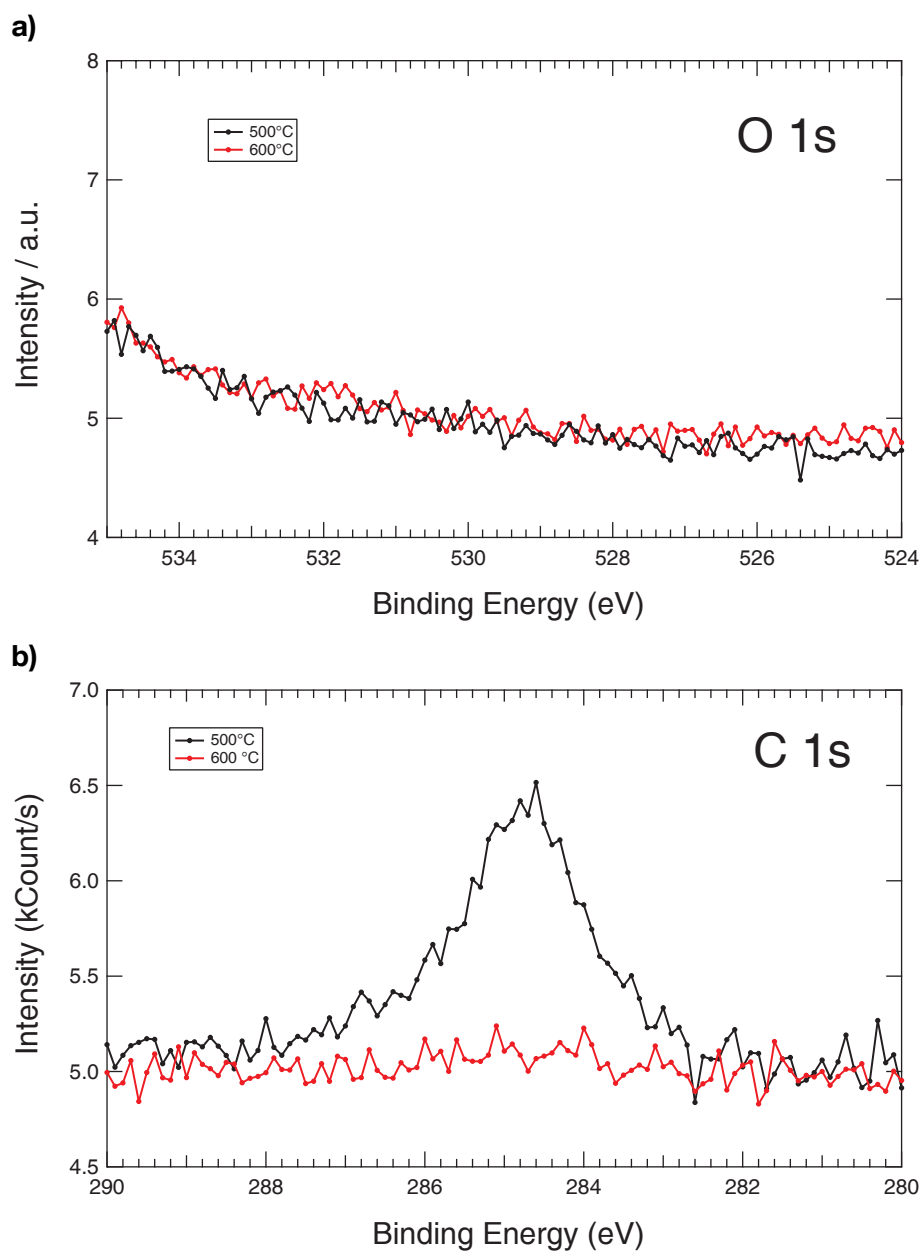


**Figure C.4.:** XPS of FeSi, sputtered and annealed at different temperatures. **a)** O 1s **b)** C 1s

### C.3. Structural models

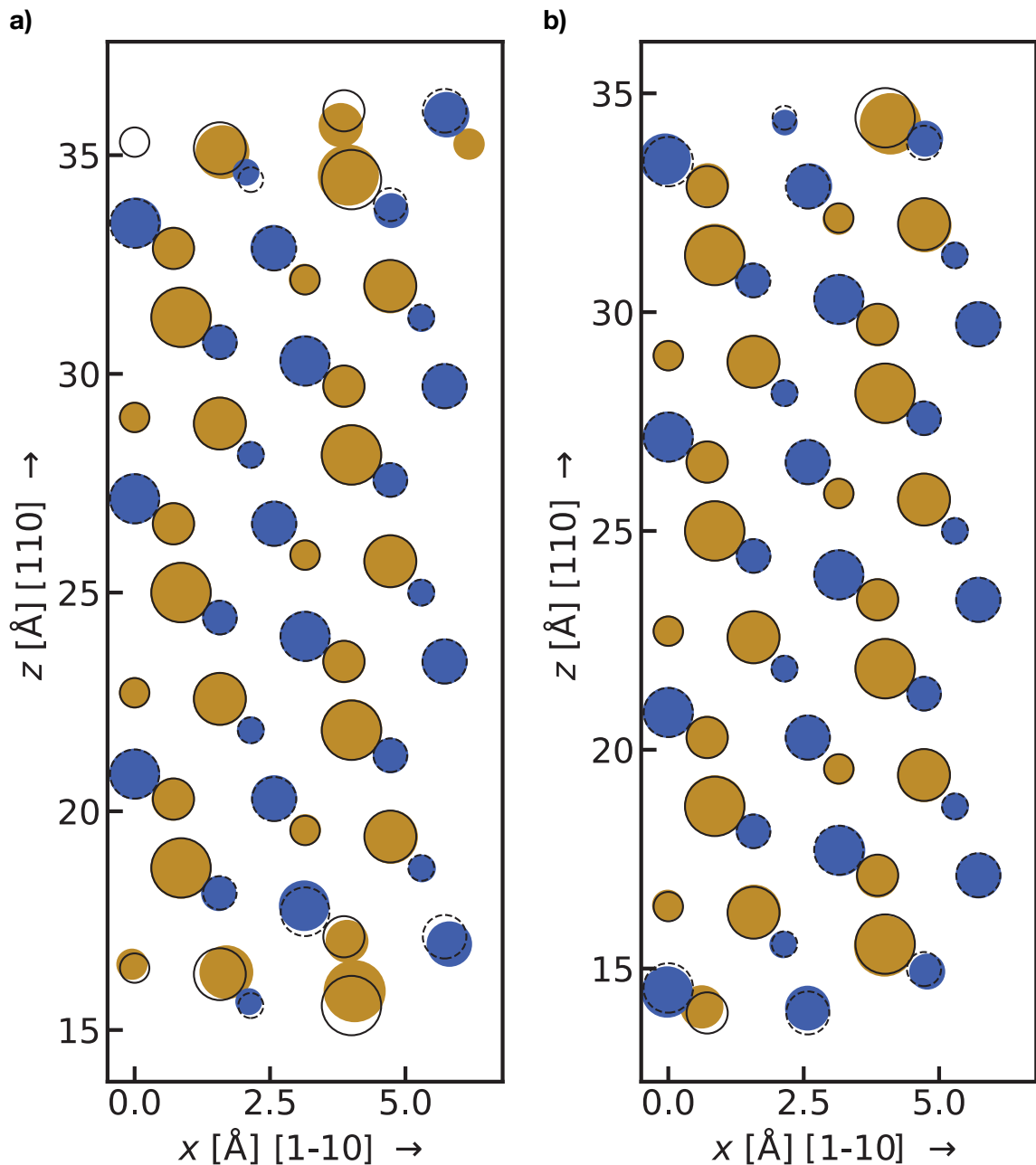


**Figure C.5.:** Structural models from DFT calculations of different terminations of the FeSi(110) surface (*cf.* Figure 6.5). Spin polarization of electrons was neglected. Black circles represent the unrelaxed positions, whereas colored spheres show the relaxed structure and the sizes account for their distance to the viewing plane (100). **a)** M1. **b)** M2.

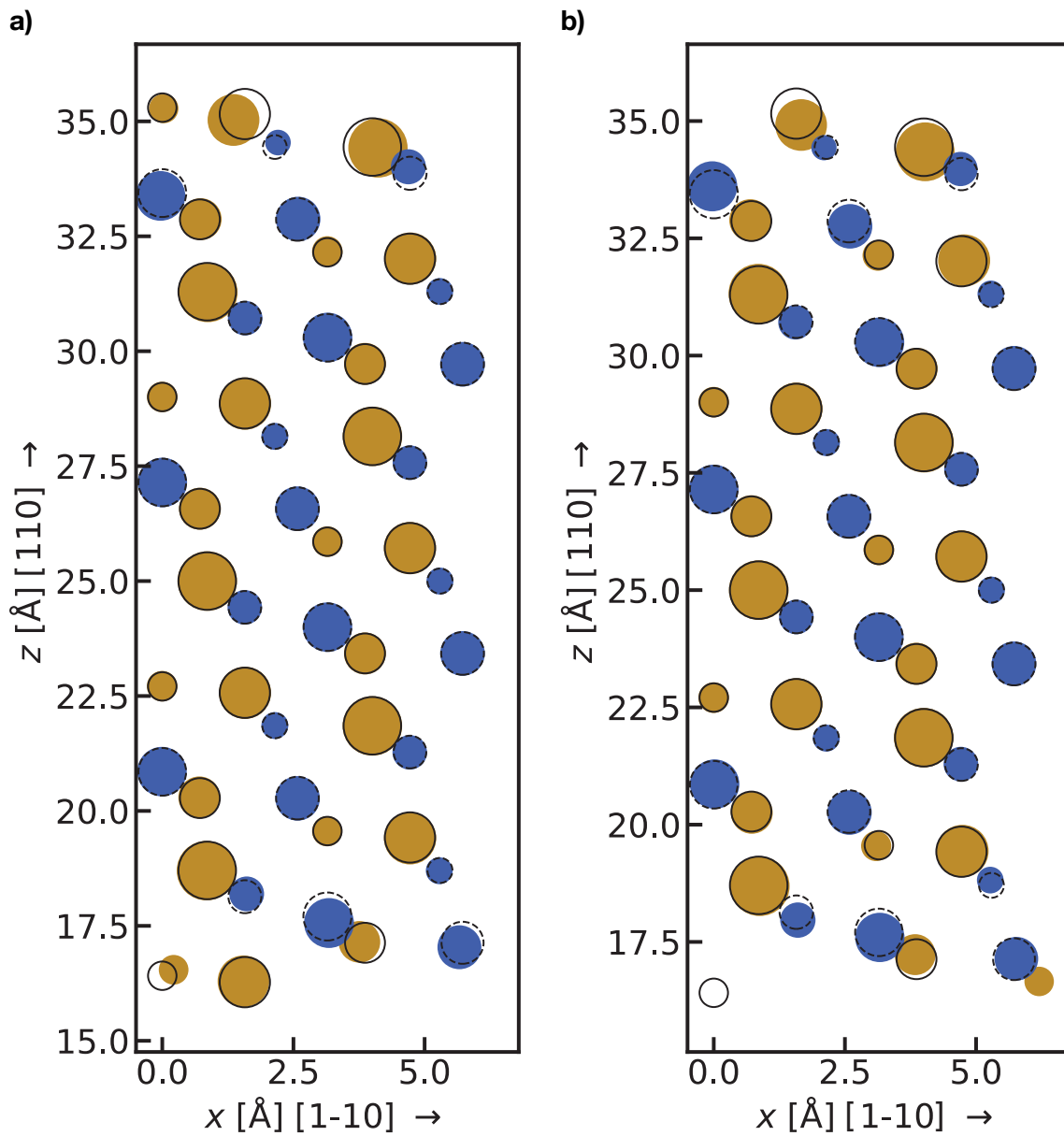


**Figure C.6.:** Structural models from DFT calculations of different terminations of the FeSi(110) surface (*cf.* Figure 6.5). Spin polarization of electrons was allowed. Black circles represent the unrelaxed positions, whereas colored spheres show the relaxed structure and the sizes account for their distance to the viewing plane (100). **a)** F1 **b)** F2

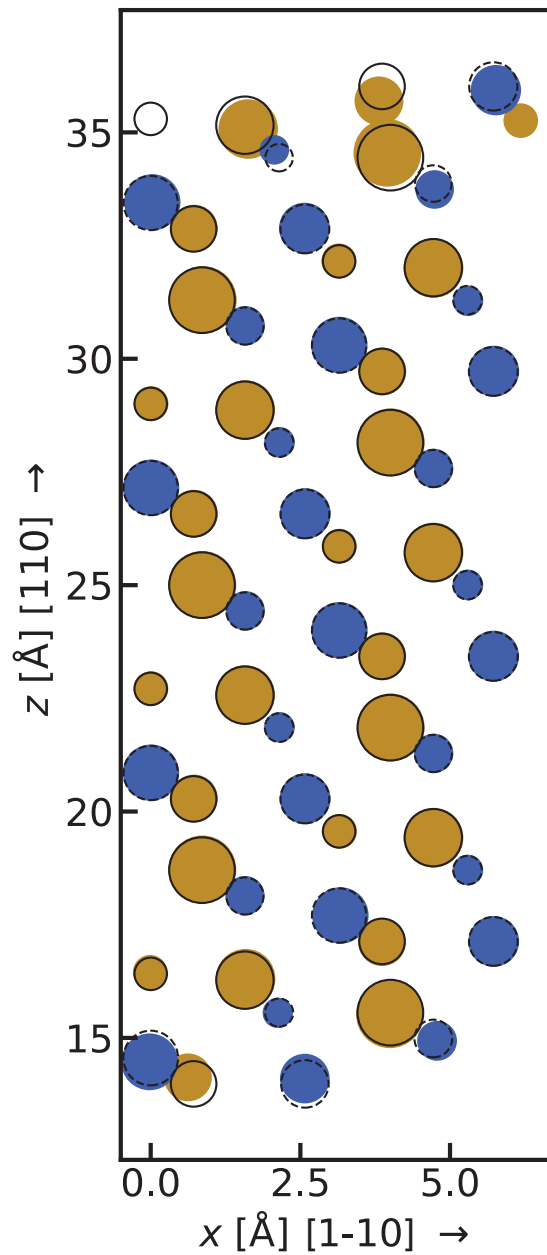


**Figure C.7.:** Structural models from DFT calculations of the M1+M2 of the FeSi(110) surface (*cf.* Figure 6.5). The top of the slab is M1 terminated, the bottom M2 terminated. Spin polarization of electrons was neglected. Black circles represent the unrelaxed positions, whereas colored spheres show the relaxed structure and the sizes account for their distance to the viewing plane (100).





## Bibliography

- [1] C. B. Duke. “The birth and evolution of surface science: Child of the union of science and technology”. *Proceedings of the National Academy of Sciences* **100** (2003), 3858–3864. DOI: 10.1073/pnas.0730358100.
- [2] N. Taniguchi. “On the Basic Concept of Nano-Technology”. *Proceedings of the International Conference on Production Engineering, Tokyo* (1974).
- [3] K. E. Drexler. *Engines of creation - The Coming Era of Nanotechnology (Anchor Library of Science)*. Anchor Books, New York, 1986.
- [4] C. Toumey. “Plenty of room, plenty of history”. en. *Nature Nanotechnology* **4** (2009), 783–784. DOI: 10.1038/nnano.2009.357.
- [5] G. Binnig, H. Rohrer, C. Gerber and E. Weibel. “Tunneling through a controllable vacuum gap”. *Applied Physics Letters* **40** (1982), 178–180. DOI: 10.1063/1.92999.
- [6] G. Binnig, C. F. Quate and C. Gerber. “Atomic Force Microscope”. *Physical Review Letters* **56** (1986), 930–933. DOI: 10.1103/physrevlett.56.930.
- [7] G. E. Moore. “Cramming more components onto integrated circuits”. *Electronics* **38** (1965), 114–117.
- [8] R. K. Cavin, P. Lugli and V. V. Zhirnov. “Science and Engineering Beyond Moore’s Law”. *Proceedings of the IEEE* **100** (2012), 1720–1749. DOI: 10.1109/jproc.2012.2190155.
- [9] “Editorial: The rise of quantum materials”. *Nature Physics* **12** (2016), 105–105. DOI: 10.1038/nphys3668.
- [10] J. H. Burroughes, D. D. C. Bradley, A. R. Brown, R. N. Marks, K. Mackay, R. H. Friend, P. L. Burns and A. B. Holmes. “Light-emitting diodes based on conjugated polymers”. en. *Nature* **347** (1990), 539–541. DOI: 10.1038/347539a0.
- [11] S. Günes, H. Neugebauer and N. S. Sariciftci. “Conjugated Polymer-Based Organic Solar Cells”. *Chem. Rev.* **107** (2007), 1324–1338. DOI: 10.1021/cr050149z.

## Bibliography

---

- [12] B. Meunier. “Metalloporphyrins as versatile catalysts for oxidation reactions and oxidative DNA cleavage”. *Chemical Reviews* **92** (1992), 1411–1456. DOI: 10 . 1021/cr00014a008.
- [13] S. Yoshimoto, A. Tada, K. Suto, R. Narita and K. Itaya. “Adlayer Structure and Electrochemical Reduction of O<sub>2</sub> on Self-Organized Arrays of Cobalt and Copper Tetraphenyl Porphines on a Au(111) Surface”. *Langmuir* **19** (2003), 672–677. DOI: 10 . 1021/la026449i.
- [14] G. A. Somorjai and Y. Li. “Impact of surface chemistry”. en. *Proceedings of the National Academy of Sciences* **108** (2011), 917–924. DOI: 10 . 1073/pnas . 1006669107.
- [15] K. Qadir, S. H. Joo, B. S. Mun, D. R. Butcher, J. R. Renzas, F. Aksoy, Z. Liu, G. A. Somorjai and J. Y. Park. “Intrinsic Relation between Catalytic Activity of CO Oxidation on Ru Nanoparticles and Ru Oxides Uncovered with Ambient Pressure XPS”. *Nano Letters* **12** (2012), 5761–5768. DOI: 10 . 1021/nl303072d.
- [16] J. Liu, F. R. Lucci, M. Yang, S. Lee, M. D. Marcinkowski, A. J. Therrien, C. T. Williams, E. C. H. Sykes and M. Flytzani-Stephanopoulos. “Tackling CO Poisoning with Single-Atom Alloy Catalysts”. *Journal of the American Chemical Society* **138** (2016), 6396–6399. DOI: 10 . 1021/jacs . 6b03339.
- [17] H.-J. Freund. “The Surface Science of Catalysis and More, Using Ultrathin Oxide Films as Templates: A Perspective”. *Journal of the American Chemical Society* **138** (2016), 8985–8996. DOI: 10 . 1021/jacs . 6b05565.
- [18] M. D. Marcinkowski, M. T. Darby, J. Liu, J. M. Wimble, F. R. Lucci, S. Lee, A. Michaelides, M. Flytzani-Stephanopoulos, M. Stamatakis and E. C. H. Sykes. “Pt/Cu single-atom alloys as coke-resistant catalysts for efficient C–H activation”. en. *Nature Chemistry* **10** (2018), 325–332. DOI: 10 . 1038/nchem . 2915.
- [19] M. R. Wasielewski. “Photoinduced electron transfer in supramolecular systems for artificial photosynthesis”. *Chemical Reviews* **92** (1992), 435–461. DOI: 10 . 1021/cr00011a005.
- [20] S. Mathew, A. Yella, P. Gao, R. Humphry-Baker, B. F. E. Curchod, N. Ashari-Astani, I. Tavernelli, U. Rothlisberger, M. K. Nazeeruddin and M. Grätzel. “Dye-sensitized solar cells with 13% efficiency achieved through the molecular engineering of porphyrin sensitizers”. en. *Nature Chemistry* **6** (2014), 242–247. DOI: 10 . 1038/nchem . 1861.

- 
- [21] A. Endo, M. Ogasawara, A. Takahashi, D. Yokoyama, Y. Kato and C. Adachi. “Thermally Activated Delayed Fluorescence from Sn<sup>4+</sup>-Porphyrin Complexes and Their Application to Organic Light Emitting Diodes — A Novel Mechanism for Electroluminescence”. *Advanced Materials* **21** (2009), 4802–4806. DOI: 10.1002/adma.200900983.
- [22] X. W. Sun, J. Z. Huang, J. X. Wang and Z. Xu. “A ZnO Nanorod Inorganic/Organic Heterostructure Light-Emitting Diode Emitting at 342 nm”. *Nano Letters* **8** (2008), 1219–1223. DOI: 10.1021/nl080340z.
- [23] R. Purrello, S. Gurrieri and R. Lauceri. “Porphyrin assemblies as chemical sensors”. *Coordination Chemistry Reviews* **190-192** (1999), 683–706. DOI: 10.1016/S0010-8545(99)00106-X.
- [24] J. Homola, S. S. Yee and G. Gauglitz. “Surface plasmon resonance sensors: review”. *Sensors and Actuators B: Chemical* **54** (1999), 3–15. DOI: 10.1016/S0925-4005(98)00321-9.
- [25] H. Song, M. A. Reed and T. Lee. “Single Molecule Electronic Devices”. en. *Advanced Materials* **23** (2011), 1583–1608. DOI: 10.1002/adma.201004291.
- [26] E. Perrin Mickael L. and Burzurí and H. S. J. van der Zant. “Single-molecule transistors”. en. *Chemical Society Reviews* **44** (2015), 902–919. DOI: 10.1039/C4CS00231H.
- [27] D. M. Eigler and E. K. Schweizer. “Positioning single atoms with a scanning tunnelling microscope”. en. *Nature* **344** (1990), 524–526. DOI: 10.1038/344524a0.
- [28] H. W. Kroto, J. R. Heath, S. C. O’Brien, R. F. Curl and R. E. Smalley. “C<sub>60</sub>: Buckminsterfullerene”. en. *Nature* **318** (1985), 162–163. DOI: 10.1038/318162a0.
- [29] S. Iijima. “Helical microtubules of graphitic carbon”. en. *Nature* **354** (1991), 56–58. DOI: 10.1038/354056a0.
- [30] J. V. Barth, G. Costantini and K. Kern. “Engineering atomic and molecular nanostructures at surfaces”. *Nature* **437** (2005), 671. DOI: 10.1038/nature04166.
- [31] G. Ertl. “Reactions at Surfaces: From Atoms to Complexity (Nobel Lecture)”. *Angewandte Chemie International Edition* **47** (2008), 3524–3535. DOI: 10.1002/anie.200800480.

## Bibliography

---

- [32] K. S. Novoselov, A. K. Geim, S. V. Morozov, D. Jiang, Y. Zhang, S. V. Dubonos, I. V. Grigorieva and A. A. Firsov. “Electric Field Effect in Atomically Thin Carbon Films”. en. *Science* **306** (2004), 666–669. DOI: 10.1126/science.1102896.
- [33] L. Liu, Y. P. Feng and Z. X. Shen. “Structural and electronic properties of h-BN”. *Physical Review B* **68** (2003). DOI: 10.1103/physrevb.68.104102.
- [34] P. Avouris, T. F. Heinz and T. Low, eds. *2D Materials: Properties and Devices*. Cambridge University Press, 2017. DOI: 10.1017/9781316681619.
- [35] P. Ruffieux, S. Wang, B. Yang, C. Sánchez-Sánchez, J. Liu, T. Dienel, L. Talirz, P. Shinde, C. A. Pignedoli, D. Passerone, T. Dumslaff, X. Feng, K. Müllen and R. Fasel. “On-surface synthesis of graphene nanoribbons with zigzag edge topology”. en. *Nature* **531** (2016), 489–492. DOI: 10.1038/nature17151.
- [36] F. Klappenberger, R. Hellwig, P. Du, T. Paintner, M. Uphoff, L. Zhang, T. Lin, B. A. Moghanaki, M. Paszkiewicz, I. Vobornik, J. Fujii, O. Fuhr, Y.-Q. Zhang, F. Allegretti, M. Ruben and J. V. Barth. “Functionalized Graphdiyne Nanowires: On-Surface Synthesis and Assessment of Band Structure, Flexibility, and Information Storage Potential”. *Small* **14** (2018), 1704321. DOI: 10.1002/smll.201704321.
- [37] J. V. Barth. “Molecular Architectonic on Metal Surfaces”. *Annual Review of Physical Chemistry* **58** (2007), 375–407. DOI: 10.1146/annurev.physchem.56.092503.141259.
- [38] J.-C. G. Bünzli. “Review: Lanthanide coordination chemistry: from old concepts to coordination polymers”. *Journal of Coordination Chemistry* **67** (2014), 3706–3733. DOI: 10.1080/00958972.2014.957201.
- [39] R. M. White. “Opportunities in Magnetic Materials”. en. *Science* **229** (1985), 11–15. DOI: 10.1126/science.229.4708.11.
- [40] V. R. Sastri, J. R. Perumareddi, V. R. Rao, G. V. S. Rayudu and J.-C. Bünzli. *Modern Aspects of Rare Earths and Their Complexes*. en. Elsevier, 2003. DOI: 10.1016/B978-0-444-51010-5.X5014-7.
- [41] L. Bogani and W. Wernsdorfer. “Molecular spintronics using single-molecule magnets”. *Nature Materials* **7** (2008), 179–186. DOI: 10.1038/nmat2133.
- [42] S. T. Liddle and J. van Slageren. “Improving f-element single molecule magnets”. *Chemical Society Reviews* **44** (19 2015), 6655–6669. DOI: 10.1039/C5CS00222B.

- 
- [43] D. Ćija, J. I. Urgel, A. P. Seitsonen, W. Auwärter and J. V. Barth. “Lanthanide-Directed Assembly of Interfacial Coordination Architectures—From Complex Networks to Functional Nanosystems”. *Accounts of Chemical Research* **51** (2018), 365–375. DOI: 10.1021/acs.accounts.7b00379.
- [44] F. Donati, S. Rusponi, S. Stepanow, C. Wäckerlin, A. Singha, L. Persichetti, R. Baltic, K. Diller, F. Patthey, E. Fernandes, J. Dreiser, Ž. Šljivančanin, K. Kummer, C. Nistor, P. Gambardella and H. Brune. “Magnetic remanence in single atoms”. *Science* **352** (2016), 318–321. DOI: 10.1126/science.aad9898.
- [45] P. Gambardella, S. Stepanow, A. Dmitriev, J. Honolka, F. M. F. de Groot, M. Lingenfelder, S. S. Gupta, D. D. Sarma, P. Bencok, S. Stanescu, S. Clair, S. Pons, N. Lin, A. P. Seitsonen, H. Brune, J. V. Barth and K. Kern. “Supramolecular control of the magnetic anisotropy in two-dimensional high-spin Fe arrays at a metal interface”. *Nature Materials* **8** (2009), 189–193. DOI: 10.1038/nmat2376.
- [46] P. S. Riseborough. “Heavy fermion semiconductors”. *Advances in Physics* **49** (2000), 257–320. DOI: 10.1080/000187300243345.
- [47] G. Aeppli and Z. Fisk. “Kondo Insulators”. *Comments on Condensed Matter Physics* **16** (1992).
- [48] W. Tian, W. Yu, J. Shi and Y. Wang. “The Property, Preparation and Application of Topological Insulators: A Review”. *Materials* **10** (2017), 814. DOI: 10.3390/ma10070814.
- [49] M. Dzero, J. Xia, V. Galitski and P. Coleman. “Topological Kondo Insulators”. *Annual Review of Condensed Matter Physics* **7** (2016), 249–280. DOI: 10.1146/annurev-conmatphys-031214-014749.
- [50] M. Wagner, R. Korntner, A. Bauer and C. Pfleiderer. “Emergence of high-mobility surface conduction in FeSi at low temperatures (*private communication*)”. 2017.
- [51] E. W. Müller. “Das Feldionenmikroskop”. *Zeitschrift für Physik* **131** (1951), 136–142. DOI: 10.1007/BF01329651.
- [52] J. C. H. Spence. *High-Resolution Electron Microscopy*. OUP Oxford, 2017. 432 pp.
- [53] G. Binnig, H. Rohrer, C. Gerber and E. Weibel. “Surface Studies by Scanning Tunneling Microscopy”. *Physical Review Letters* **49** (1982), 57–61. DOI: 10.1103/physrevlett.49.57.

## Bibliography

---

- [54] G. Binnig, H. Rohrer, C. Gerber and E. Weibel. “ $7 \times 7$  Reconstruction on Si(111) Resolved in Real Space”. *Physical Review Letters* **50** (1983), 120–123. DOI: 10.1103/physrevlett.50.120.
- [55] D. W. Pohl, W. Denk and M. Lanz. “Optical stethoscopy: Image recording with resolution  $/20$ ”. *Applied Physics Letters* **44** (1984), 651–653. DOI: 10.1063/1.94865.
- [56] G. Gamow. “Zur Quantentheorie des Atomkernes”. *Zeitschrift für Physik* **51** (1928), 204–212. DOI: 10.1007/BF01343196.
- [57] J. Frenkel. “On the Electrical Resistance of Contacts between Solid Conductors”. *Physical Review* **36** (1930), 1604–1618. DOI: 10.1103/physrev.36.1604.
- [58] I. Giaever. “Energy Gap in Superconductors Measured by Electron Tunneling”. *Physical Review Letters* **5** (1960), 147–148. DOI: 10.1103/physrevlett.5.147.
- [59] R. H. Fowler and L. Nordheim. “Electron Emission in Intense Electric Fields”. *Proceedings of the Royal Society A: Mathematical, Physical and Engineering Sciences* **119** (1928), 173–181. DOI: 10.1098/rspa.1928.0091.
- [60] C. J. Chen. *Introduction to Scanning Tunneling Microscopy*. Oxford University Press, 2007. DOI: 10.1093/acprof:oso/9780199211500.001.0001.
- [61] W. Nolting. *Grundkurs Theoretische Physik 5/2*. Springer Berlin Heidelberg, 2015. DOI: 10.1007/978-3-662-44230-2.
- [62] J. Bardeen. “Tunnelling from a Many-Particle Point of View”. *Physical Review Letters* **6** (1961), 57–59. DOI: 10.1103/physrevlett.6.57.
- [63] J. Tersoff and D. R. Hamann. “Theory and Application for the Scanning Tunneling Microscope”. *Physical Review Letters* **50** (1983), 1998–2001. DOI: 10.1103/physrevlett.50.1998.
- [64] J. Tersoff and D. R. Hamann. “Theory of the scanning tunneling microscope”. *Physical Review B* **31** (1985), 805–813. DOI: 10.1103/physrevb.31.805.
- [65] A. Selloni, P. Carnevali, E. Tosatti and C. D. Chen. “Voltage-dependent scanning-tunneling microscopy of a crystal surface: Graphite”. *Physical Review B* **31** (1985), 2602–2605. DOI: 10.1103/physrevb.31.2602.

- 
- [66] G. Binnig, K. H. Frank, H. Fuchs, N. Garcia, B. Reihl, H. Rohrer, F. Salvan and A. R. Williams. “Tunneling Spectroscopy and Inverse Photoemission: Image and Field States”. *Physical Review Letters* **55** (1985), 991–994. DOI: 10.1103/physrevlett.55.991.
- [67] M. F. Crommie, C. P. Lutz and D. M. Eigler. “Confinement of Electrons to Quantum Corrals on a Metal Surface”. *Science* **262** (1993), 218–220. DOI: 10.1126/science.262.5131.218.
- [68] M. F. Crommie, C. P. Lutz and D. M. Eigler. “Imaging standing waves in a two-dimensional electron gas”. *Nature* **363** (1993), 524–527. DOI: 10.1038/363524a0.
- [69] A. Biedermann, O. Genser, W. Hebenstreit, M. Schmid, J. Redinger, R. Podloucky and P. Varga. “Scanning Tunneling Spectroscopy of One-Dimensional Surface States on a Metal Surface”. *Physical Review Letters* **76** (1996), 4179–4182. DOI: 10.1103/physrevlett.76.4179.
- [70] W. Auwärter, A. Weber-Bargioni, S. Brink, A. Riemann, A. Schiffrin, M. Ruben and J. V. Barth. “Controlled Metalation of Self-Assembled Porphyrin Nanoarrays in Two Dimensions”. *ChemPhysChem* **8** (2007), 250–254. DOI: 10.1002/cphc.200600675.
- [71] Y. Pennec, W. Auwärter, A. Schiffrin, A. Weber-Bargioni, A. Riemann and J. V. Barth. “Supramolecular gratings for tuneable confinement of electrons on metal surfaces”. *Nature Nanotechnology* **2** (2007), 99–103. DOI: 10.1038/nnano.2006.212.
- [72] A. Weber-Bargioni, W. Auwärter, F. Klappenberger, J. Reichert, S. Lefrançois, T. Strunskus, C. Wöll, A. Schiffrin, Y. Pennec and J. V. Barth. “Visualizing the Frontier Orbitals of a Conformationally Adapted Metalloporphyrin”. *ChemPhysChem* **9** (2008), 89–94. DOI: 10.1002/cphc.200700600.
- [73] W. Krenner, D. Kühne, F. Klappenberger and J. V. Barth. “Assessment of Scanning Tunneling Spectroscopy Modes Inspecting Electron Confinement in Surface-Confined Supramolecular Networks”. *Scientific Reports* **3** (2013), 1454. DOI: 10.1038/srep01454.
- [74] J. Klein, A. Léger, M. Belin, D. Défourneau and M. J. L. Sangster. “Inelastic-Electron-Tunneling Spectroscopy of Metal-Insulator-Metal Junctions”. *Physical Review B* **7** (1973), 2336–2348. DOI: 10.1103/physrevb.7.2336.

## Bibliography

---

- [75] B. C. Stipe. “Single-Molecule Vibrational Spectroscopy and Microscopy”. *Science* **280** (1998), 1732–1735. DOI: 10.1126/science.280.5370.1732.
- [76] W. Ho. “Single-molecule chemistry”. *The Journal of Chemical Physics* **117** (2002), 11033–11061. DOI: 10.1063/1.1521153.
- [77] S. R. Burema, K. Seufert, W. Auwärter, J. V. Barth and M.-L. Bocquet. “Probing Nitrosyl Ligation of Surface-Confined Metalloporphyrins by Inelastic Electron Tunneling Spectroscopy”. *ACS Nano* **7** (2013), 5273–5281. DOI: 10.1021/nn4010582.
- [78] M. Bode, O. Pietzsch, A. Kubetzka, S. Heinze and R. Wiesendanger. “Experimental Evidence for Intra-Atomic Noncollinear Magnetism at Thin Film Probe Tips”. *Physical Review Letters* **86** (2001), 2142–2145. DOI: 10.1103/physrevlett.86.2142.
- [79] O. Pietzsch. “Observation of Magnetic Hysteresis at the Nanometer Scale by Spin-Polarized Scanning Tunneling Spectroscopy”. *Science* **292** (2001), 2053–2056. DOI: 10.1126/science.1060513.
- [80] A. Garcia-Lekue, T. Balashov, M. Olle, G. Ceballos, A. Arnau, P. Gambardella, D. Sanchez-Portal and A. Mugarza. “Spin-Dependent Electron Scattering at Graphene Edges on Ni(111)”. *Physical Review Letters* **112** (2014), 066802. DOI: 10.1103/physrevlett.112.066802.
- [81] M. Ternes. “Scanning tunneling spectroscopy at the single atom scale”. PhD thesis. École Polytechnique Fédérale de Lausanne, 2006.
- [82] J. Kröger, L. Limot, H. Jensen, R. Berndt, S. Crampin and E. Pehlke. “Surface state electron dynamics of clean and adsorbate-covered metal surfaces studied with the scanning tunnelling microscope”. *Progress in Surface Science* **80** (2005), 26–48. DOI: 10.1016/j.progsurf.2005.10.002.
- [83] C. Davisson and L. H. Germer. “Diffraction of Electrons by a Crystal of Nickel”. *Physical Review* **30** (1927), 705–740. DOI: 10.1103/physrev.30.705.
- [84] C. Davisson and L. H. Germer. “The Scattering of Electrons by a Single Crystal of Nickel”. *Nature* **119** (1927), 558–560. DOI: 10.1038/119558a0.
- [85] G. P. Thomson and A. Reid. “Diffraction of Cathode Rays by a Thin Film”. *Nature* **119** (1927), 890–890. DOI: 10.1038/119890a0.



- 
- [86] L. de Broglie. “Recherches sur la théorie des Quanta”. *Annales de Physique* **10** (1925), 22–128. DOI: 10.1051/anphys/192510030022.
- [87] M. Henzler and W. Göpel. *Oberflächenphysik des Festkörpers*. Vieweg + Teubner Verlag, 1994. DOI: 10.1007/978-3-322-84875-8.
- [88] H. Lüth. *Solid Surfaces, Interfaces and Thin Films*. Springer Berlin Heidelberg, 2010. DOI: 10.1007/978-3-642-13592-7.
- [89] K. Oura, M. Katayama, A. V. Zotov, V. G. Lifshits and A. A. Saranin. *Surface Science*. Springer Berlin Heidelberg, 2003. DOI: 10.1007/978-3-662-05179-5.
- [90] D. P. Woodruff and T. A. Delchar. *Modern Techniques of Surface Science*. Cambridge University Press, 1994. DOI: 10.1017/cbo9780511623172.
- [91] P. P. Ewald. “Zur Theorie der Interferenzen der Röntgenstrahlen in Kristallen”. *Physikalische Zeitschrift* **14** (1913), 465–472.
- [92] L. Zhang, T. Miyamachi, T. Tomanić, R. Dehm and W. Wulfhekel. “A compact sub-Kelvin ultrahigh vacuum scanning tunneling microscope with high energy resolution and high stability”. *Review of Scientific Instruments* **82** (2011), 103702. DOI: 10.1063/1.3646468.
- [93] M. Uphoff, G. S. Michelitsch, R. Hellwig, K. Reuter, H. Brune, F. Klappenberger and J. V. Barth. “Assembly of Robust Holmium-Directed 2D Metal–Organic Coordination Complexes and Networks on the Ag(100) Surface”. *ACS Nano* **12** (2018), 11552–11560. DOI: 10.1021/acsnano.8b06704.
- [94] T. M. Reineke, M. Eddaoudi, M. Fehr, D. Kelley and O. M. Yaghi. “From Condensed Lanthanide Coordination Solids to Microporous Frameworks Having Accessible Metal Sites”. *Journal of the American Chemical Society* **121** (1999), 1651–1657. DOI: 10.1021/ja983577d.
- [95] L. Pan, K. M. Adams, H. E. Hernandez, X. Wang, C. Zheng, Y. Hattori and K. Kaneko. “Porous Lanthanide–Organic Frameworks: Synthesis, Characterization, and Unprecedented Gas Adsorption Properties”. *Journal of the American Chemical Society* **125** (2003), 3062–3067. DOI: 10.1021/ja028996w.
- [96] C. Qin, X.-L. Wang, E.-B. Wang and Z.-M. Su. “A Series of Three-Dimensional Lanthanide Coordination Polymers with Rutile and Unprecedented Rutile-Related Topologies”. *Inorganic Chemistry* **44** (2005), 7122–7129. DOI: 10.1021/ic050906b.

- [97] D.-L. Long, A. J. Blake, N. R. Champness, C. Wilson and M. Schröder. “Lanthanum Coordination Networks Based on Unusual Five-Connected Topologies”. *Journal of the American Chemical Society* **123** (2001), 3401–3402. DOI: 10.1021/ja0030461.
- [98] D.-L. Long, R. J. Hill, A. J. Blake, N. R. Champness, P. Hubberstey, D. M. Proserpio, C. Wilson and M. Schröder. “Non-Natural Eight-Connected Solid-State Materials: A New Coordination Chemistry”. *Angewandte Chemie International Edition* **43** (2004), 1851–1854. DOI: 10.1002/anie.200352625.
- [99] D.-L. Long, A. J. Blake, N. R. Champness, C. Wilson and M. Schröder. “Unprecedented Seven- and Eight-Connected Lanthanide Coordination Networks”. *Angewandte Chemie International Edition* **40** (2001), 2443–2447. DOI: 10.1002/1521-3773(20010702)40:13<2443::AID-ANIE2443>3.0.CO;2-C.
- [100] D. Écija, W. Auwärter, S. Vijayaraghavan, K. Seufert, F. Bischoff, K. Tashiro and J. V. Barth. “Assembly and Manipulation of Rotatable Cerium Porphyrinato Sandwich Complexes on a Surface”. *Angewandte Chemie International Edition* **50** (2011), 3872–3877. DOI: 10.1002/anie.201007370.
- [101] B. Cirera, J. Björk, R. Otero, J. M. Gallego, R. Miranda and D. Ecija. “Efficient Lanthanide Catalyzed Debromination and Oligomeric Length-Controlled Ullmann Coupling of Aryl Halides”. *The Journal of Physical Chemistry C* **121** (2017), 8033–8041. DOI: 10.1021/acs.jpcc.7b02172.
- [102] F. Bischoff, K. Seufert, W. Auwärter, A. P. Seitsonen, D. Heim and J. V. Barth. “Metalation of Porphyrins by Lanthanide Atoms at Interfaces: Direct Observation and Stimulation of Cerium Coordination to 2H-TPP/Ag(111)”. *The Journal of Physical Chemistry C* **122** (2018), 5083–5092. DOI: 10.1021/acs.jpcc.7b10363.
- [103] R. Hellwig, M. Uphoff, T. Paintner, J. Björk, M. Ruben, F. Klappenberger and J. V. Barth. “Ho-Mediated alkyne reactions at low temperatures on Ag(111)”. *Chemistry - A European Journal* **24** (2018), 16126–16135. DOI: 10.1002/chem.201803102.
- [104] D. Écija, J. I. Urgel, A. C. Papageorgiou, S. Joshi, W. Auwärter, A. P. Seitsonen, S. Klyatskaya, M. Ruben, S. Fischer, S. Vijayaraghavan, J. Reichert and J. V. Barth. “Five-vertex Archimedean surface tessellation by lanthanide-directed

- 
- molecular self-assembly”. *Proceedings of the National Academy of Sciences* **110** (2013), 6678–6681. DOI: 10.1073/pnas.1222713110.
- [105] J. I. Urgel, D. Ecija, W. Auwärter and J. V. Barth. “Controlled Manipulation of Gadolinium-Coordinated Supramolecules by Low-Temperature Scanning Tunneling Microscopy”. *Nano Letters* **14** (2014), 1369–1373. DOI: 10.1021/nl4044339.
- [106] J. I. Urgel, D. Ecija, W. Auwärter, A. C. Papageorgiou, A. P. Seitsonen, S. Vijayaraghavan, S. Joshi, S. Fischer, J. Reichert and J. V. Barth. “Five-Vertex Lanthanide Coordination on Surfaces: A Route to Sophisticated Nanoarchitectures and Tessellations”. *The Journal of Physical Chemistry C* **118** (2014), 12908–12915. DOI: 10.1021/jp502901z.
- [107] J. I. Urgel, B. Cirera, Y. Wang, W. Auwärter, R. Otero, J. M. Gallego, M. Alcamí, S. Klyatskaya, M. Ruben, F. Martín, R. Miranda, D. Ecija and J. V. Barth. “Surface-Supported Robust 2D Lanthanide-Carboxylate Coordination Networks”. *Small* **11** (2015), 6358–6364. DOI: 10.1002/smll.201502761.
- [108] N. Ishikawa, M. Sugita, T. Ishikawa, S.-y. Koshihara and Y. Kaizu. “Lanthanide Double-Decker Complexes Functioning as Magnets at the Single-Molecular Level”. *Journal of the American Chemical Society* **125** (2003), 8694–8695. DOI: 10.1021/ja029629n.
- [109] R. S. Dante Gatteschi and J. Villain. *Molecular Nanomagnets*. Oxford University, 2006. DOI: 10.1093/acprof:oso/9780198567530.001.0001.
- [110] S. Kyatskaya, J. R. Galán Mascarós, L. Bogani, F. Hennrich, M. Kappes, W. Wernsdorfer and M. Ruben. “Anchoring of Rare-Earth-Based Single-Molecule Magnets on Single-Walled Carbon Nanotubes”. *Journal of the American Chemical Society* **131** (2009), 15143–15151. DOI: 10.1021/ja906165e.
- [111] J. D. Rinehart and J. R. Long. “Exploiting single-ion anisotropy in the design of f-element single-molecule magnets”. *Chemical Science* **2** (11 2011), 2078–2085. DOI: 10.1039/C1SC00513H.
- [112] R. Westerström, J. Dreiser, C. Piamonteze, M. Muntwiler, S. Weyeneth, H. Brune, S. Rusponi, F. Nolting, A. Popov, S. Yang, L. Dunsch and T. Greber. “An Endohedral Single-Molecule Magnet with Long Relaxation Times: DySc<sub>2</sub>N@C<sub>80</sub>”. *Journal of the American Chemical Society* **134** (2012), 9840–9843. DOI: 10.1021/ja301044p.

## Bibliography

---

- [113] R. A. Layfield. “Organometallic Single-Molecule Magnets”. *Organometallics* **33** (2014), 1084–1099. DOI: 10.1021/om401107f.
- [114] F. D. Natterer, K. Yang, W. Paul, P. Willke, T. Choi, T. Greber, A. J. Heinrich and C. P. Lutz. “Reading and writing single-atom magnets”. *Nature* **543** (2017), 226–228. DOI: 10.1038/nature21371.
- [115] F. D. Natterer, F. Donati, F. Patthey and H. Brune. “Thermal and Magnetic-Field Stability of Holmium Single-Atom Magnets”. *Physical Review Letters* **121** (2018), 027201. DOI: 10.1103/physrevlett.121.027201.
- [116] K. J. Franke, G. Schulze and J. I. Pascual. “Competition of Superconducting Phenomena and Kondo Screening at the Nanoscale”. *Science* **332** (2011), 940–944. DOI: 10.1126/science.1202204.
- [117] J. V. Barth. “Fresh perspectives for surface coordination chemistry”. *Surface Science* **603** (2009). Special Issue of Surface Science dedicated to Prof. Dr. Dr. h.c. mult. Gerhard Ertl, Nobel-Laureate in Chemistry 2007, 1533–1541. DOI: 10.1016/j.susc.2008.09.049.
- [118] T. Suzuki, T. Lutz, D. Payer, N. Lin, S. L. Tait, G. Costantini and K. Kern. “Substrate effect on supramolecular self-assembly: from semiconductors to metals”. *Physical Chemistry Chemical Physics* **11** (30 2009), 6498–6504. DOI: 10.1039/B905125B.
- [119] B. Cirera, L. Đorđević, R. Otero, J. M. Gallego, D. Bonifazi, R. Miranda and D. Ecija. “Dysprosium-carboxylate nanomeshes with tunable cavity size and assembly motif through ionic interactions”. *Chemical Communications* **52** (2016), 11227–11230. DOI: 10.1039/c6cc04874a.
- [120] S. Stepanow, T. Strunskus, M. Lingenfelder, A. Dmitriev, H. Spillmann, N. Lin, J. V. Barth, C. Wöll and K. Kern. “Deprotonation-Driven Phase Transformations in Terephthalic Acid Self-Assembly on Cu(100)”. *The Journal of Physical Chemistry B* **108** (2004), 19392–19397. DOI: 10.1021/jp046766t.
- [121] C. Wäckerlin, F. Donati, A. Singha, R. Baltic, S. Rusponi, K. Diller, F. Patthey, M. Pivetta, Y. Lan, S. Klyatskaya, M. Ruben, H. Brune and J. Dreiser. “Giant Hysteresis of Single-Molecule Magnets Adsorbed on a Nonmagnetic Insulator”. *Advanced Materials* **28** (2016), 5195–5199. DOI: 10.1002/adma.201506305.

- 
- [122] A. Dmitriev, H. Spillmann, N. Lin, J. V. Barth and K. Kern. “Modular Assembly of Two-Dimensional Metal–Organic Coordination Networks at a Metal Surface”. *Angewandte Chemie International Edition* **115** (2003), 2774–2777. DOI: 10.1002/ange.200250610.
- [123] M. A. Lingenfelder, H. Spillmann, A. Dmitriev, S. Stepanow, N. Lin, J. V. Barth and K. Kern. “Towards Surface-Supported Supramolecular Architectures: Tailored Coordination Assembly of 1,4-Benzenedicarboxylate and Fe on Cu(100)”. *Chemistry - A European Journal* **10** (2004), 1913–1919. DOI: 10.1002/chem.200305589.
- [124] D. Payer, A. Comisso, A. Dmitriev, T. Strunskus, N. Lin, C. Wöll, A. DeVita, J. V. Barth and K. Kern. “Ionic Hydrogen Bonds Controlling Two-Dimensional Supramolecular Systems at a Metal Surface”. *Chemistry - A European Journal* **13** (2007), 3900–3906. DOI: 10.1002/chem.200601325.
- [125] F. Klappenberger, E. Arras, A. P. Seitsonen and J. V. Barth. “Nature of the attractive interaction between proton acceptors and organic ring systems”. *Physical Chemistry Chemical Physics* **14** (46 2012), 15995–16001. DOI: 10.1039/C2CP42293J.
- [126] G. A. Jeffrey. *An Introduction to Hydrogen Bonding*. Oxford University Press, 1997.
- [127] M. E. Cañas-Ventura, F. Klappenberger, S. Clair, S. Pons, K. Kern, H. Brune, T. Strunskus, C. Wöll, R. Fasel and J. V. Barth. “Coexistence of one- and two-dimensional supramolecular assemblies of terephthalic acid on Pd(111) due to self-limiting deprotonation”. *The Journal of Chemical Physics* **125** (2006), 184710. DOI: 10.1063/1.2364478.
- [128] S. Clair, S. Pons, A. P. Seitsonen, H. Brune, K. Kern and J. V. Barth. “STM Study of Terephthalic Acid Self-Assembly on Au(111): Hydrogen-Bonded Sheets on an Inhomogeneous Substrate†”. *The Journal of Physical Chemistry B* **108** (2004), 14585–14590. DOI: 10.1021/jp049501n.
- [129] N. Lin, A. Dmitriev, J. Weckesser, J. V. Barth and K. Kern. “Real-Time Single-Molecule Imaging of the Formation and Dynamics of Coordination Compounds”. *Angewandte Chemie International Edition* **41** (2002), 4779–4783. DOI: 10.1002/anie.200290046.

## Bibliography

---

- [130] P. Messina, A. Dmitriev, N. Lin, H. Spillmann, M. Abel, J. V. Barth and K. Kern. “Direct Observation of Chiral Metal-Organic Complexes Assembled on a Cu(100) Surface”. *Journal of the American Chemical Society* **124** (2002), 14000–14001. DOI: 10.1021/ja028553s.
- [131] A. Mugarza, N. Lorente, P. Ordejón, C. Krull, S. Stepanow, M.-L. Bocquet, J. Fraxedas, G. Ceballos and P. Gambardella. “Orbital Specific Chirality and Homochiral Self-Assembly of Achiral Molecules Induced by Charge Transfer and Spontaneous Symmetry Breaking”. *Physical Review Letters* **105** (2010), 027201. DOI: 10.1103/physrevlett.105.115702.
- [132] C. Liu, J. Cohen, J. Adams and A. Voter. “EAM study of surface self-diffusion of single adatoms of fcc metals Ni, Cu, Al, Ag, Au, Pd, and Pt”. *Surface Science* **253** (1991), 334–344. DOI: 10.1016/0039-6028(91)90604-Q.
- [133] S. Clair, S. Pons, S. Fabris, S. Baroni, H. Brune, K. Kern and J. V. Barth. “Monitoring Two-Dimensional Coordination Reactions: Directed Assembly of Co-Terephthalate Nanosystems on Au(111)”. *The Journal of Physical Chemistry B* **110** (2006), 5627–5632. DOI: 10.1021/jp057239s.
- [134] S. Stepanow, N. Lin, D. Payer, U. Schlickum, F. Klappenberger, G. Zoppellaro, M. Ruben, H. Brune, J. V. Barth and K. Kern. “Surface-Assisted Assembly of 2D Metal–Organic Networks That Exhibit Unusual Threefold Coordination Symmetry”. *Angewandte Chemie International Edition* **46** (2007), 710–713. DOI: 10.1002/anie.200603644.
- [135] V. M. Hallmark, S. Chiang, K.-P. Meinhart and K. Hafner. “Observation and calculation of internal structure in scanning tunneling microscopy images of related molecules”. *Physical Review Letters* **70** (24 1993), 3740–3743. DOI: 10.1103/PhysRevLett.70.3740.
- [136] S. Chiang. “Scanning Tunneling Microscopy Imaging of Small Adsorbed Molecules on Metal Surfaces in an Ultrahigh Vacuum Environment”. *Chemical Reviews* **97** (1997), 1083–1096. DOI: 10.1021/cr940555a.
- [137] A. F. Lee, R. M. Lambert, A. Goldoni, A. Baraldi and G. Paolucci. “On the Coverage - Dependent Adsorption Geometry of Benzene Adsorbed on Pd111: A Study by Fast XPS and NEXAFS”. *The Journal of Physical Chemistry B* **104** (2000), 11729–11733. DOI: 10.1021/jp002635q.

- 
- [138] M. Robledo, G. Pacchioni, F. Martín, M. Alcamí and S. Díaz-Tendero. “Adsorption of Benzene on Cu(100) and on Cu(100) Covered with an Ultrathin NaCl Film: Molecule–Substrate Interaction and Decoupling”. *The Journal of Physical Chemistry C* **119** (2015), 4062–4071. DOI: 10.1021/jp5106604.
- [139] S. Cotton. *Lanthanide and Actinide Chemistry*. John Wiley and Sons, Ltd., 2006.
- [140] A. P. Seitsonen, M. Lingenfelder, H. Spillmann, A. Dmitriev, S. Stepanow, N. Lin, K. Kern and J. V. Barth. “Density Functional Theory Analysis of Carboxylate-Bridged Diiron Units in Two-Dimensional Metal–Organic Grids”. *Journal of the American Chemical Society* **128** (2006), 5634–5635. DOI: 10.1021/ja060180y.
- [141] J. P. Perdew, K. Burke and M. Ernzerhof. “Generalized Gradient Approximation Made Simple”. *Physical Review Letters* **77** (18 1996), 3865–3868. DOI: 10.1103/PhysRevLett.77.3865.
- [142] M.-C. Wu, C. A. Estrada, J. S. Corneille and D. W. Goodman. “Model surface studies of metal oxides: Adsorption of water and methanol on ultrathin MgO films on Mo(100)”. *The Journal of Chemical Physics* **96** (1992), 3892–3900. DOI: 10.1063/1.461893.
- [143] M. Gallagher, M. Fyfield, J. Cowin and S. Joyce. “Imaging insulating oxides: scanning tunneling microscopy of ultrathin MgO films on Mo(001)”. *Surface Science* **339** (1995), L909–L913. DOI: 10.1016/0039-6028(95)80056-5.
- [144] H. L. Meyerheim, R. Popescu, J. Kirschner, N. Jedrecy, M. Sauvage-Simkin, B. Heinrich and R. Pinchaux. “Geometrical and Compositional Structure at Metal-Oxide Interfaces: MgO on Fe(001)”. *Physical Review Letters* **87** (2001), 076102. DOI: 10.1103/physrevlett.87.076102.
- [145] S. Altieri, L. H. Tjeng and G. A. Sawatzky. “Electronic structure and chemical reactivity of oxide-metal interfaces: MgO(100)/Ag(100)”. *Physical Review B* **61** (2000), 16948–16955. DOI: 10.1103/physrevb.61.16948.
- [146] S. Schintke, S. Messerli, M. Pivetta, F. Patthey, L. Libioulle, M. Stengel, A. D. Vita and W.-D. Schneider. “Insulator at the Ultrathin Limit: MgO on Ag(001)”. *Physical Review Letters* **87** (2001), 276801. DOI: 10.1103/physrevlett.87.276801.
- [147] S. Valeri, S. Altieri, U. del Pennino, A. di Bona, P. Luches and A. Rota. “Scanning tunnelling microscopy of MgO ultrathin films on Ag(001)”. *Physical Review B* **65** (2002), 245410. DOI: 10.1103/physrevb.65.245410.

## Bibliography

---

- [148] M. Kiguchi, T. Goto, K. Saiki, T. Sasaki, Y. Iwasawa and A. Koma. “Atomic and electronic structures of MgO/Ag(100) heterointerface”. *Surface Science* **512** (2002), 97–106. DOI: 10.1016/s0039-6028(02)01577-7.
- [149] S. Schintke and W.-D. Schneider. “Insulators at the ultrathin limit: electronic structure studied by scanning tunnelling microscopy and scanning tunnelling spectroscopy”. *Journal of Physics: Condensed Matter* **16** (2004), R49.
- [150] J. Pal, M. Smerieri, E. Celasco, L. Savio, L. Vattuone and M. Rocca. “Morphology of Monolayer MgO Films on Ag(100): Switching from Corrugated Islands to Extended Flat Terraces”. *Physical Review Letters* **112** (12 2014), 126102. DOI: 10.1103/PhysRevLett.112.126102.
- [151] S. Baumann, I. G. Rau, S. Loth, C. P. Lutz and A. J. Heinrich. “Measuring the Three-Dimensional Structure of Ultrathin Insulating Films at the Atomic Scale”. *ACS Nano* **8** (2014), 1739–1744. DOI: 10.1021/nn4061034.
- [152] V. E. H. P. Cox. *The Surface Science of Metal Oxides*. Cambridge University Press, 1996.
- [153] W. P. Davey. “Precision Measurements of the Lattice Constants of Twelve Common Metals”. *Physical Review* **25** (1925), 753–761. DOI: 10.1103/physrev.25.753.
- [154] W. Paul, K. Yang, S. Baumann, N. Romming, T. Choi, C. P. Lutz and A. J. Heinrich. “Control of the millisecond spin lifetime of an electrically probed atom”. *Nature Physics* **13** (2016), 403–407. DOI: 10.1038/nphys3965.
- [155] S. Schintke, S. Messerli, K. Morgenstern, J. Nieminen and W.-D. Schneider. “Far-ranged transient motion of “hot” oxygen atoms upon dissociation”. *The Journal of Chemical Physics* **114** (2001), 4206–4209. DOI: 10.1063/1.1346687.
- [156] E. Fernandes, F. Donati, F. Patthey, S. Stavrić, Ž. Šljivančanin and H. Brune. “Adsorption sites of individual metal atoms on ultrathin MgO(100) films”. *Physical Review B* **96** (2017), 045419. DOI: 10.1103/physrevb.96.045419.
- [157] V. Jaccarino, G. K. Wertheim, J. H. Wernick, L. R. Walker and S. Arajs. “Paramagnetic Excited State of FeSi”. *Physical Review* **160** (1967), 476–482. DOI: 10.1103/physrev.160.476.



- 
- [158] R. Missman and P. Handler. “Hall mobility of a cleaned germanium surface”. *Journal of Physics and Chemistry of Solids* **8** (1959), 109–111. DOI: 10.1016/0022-3697(59)90287-2.
- [159] A. Many, N. Grover, Y. Goldstein and E. Harnik. “Surface mobility measurements in germanium”. *Journal of Physics and Chemistry of Solids* **14** (1960), 186–192. DOI: 10.1016/0022-3697(60)90228-6.
- [160] N. Grover and R. Oren. “Majority-carrier mobility on germanium surfaces”. *Journal of Physics and Chemistry of Solids* **24** (1963), 693–697. DOI: 10.1016/s0022-3697(63)80012-8.
- [161] R. F. Greene. “Surface electron transport”. *C R C Critical Reviews in Solid State Sciences* **4** (1973), 477–497. DOI: 10.1080/10408437308245839.
- [162] L. Fu, C. L. Kane and E. J. Mele. “Topological Insulators in Three Dimensions”. *Physical Review Letters* **98** (2007), 106803. DOI: 10.1103/physrevlett.98.106803.
- [163] J. E. Moore. “The birth of topological insulators”. *Nature* **464** (2010), 194–198. DOI: 10.1038/nature08916.
- [164] M. Z. Hasan and C. L. Kane. “Colloquium: Topological insulators”. *Reviews of Modern Physics* **82** (2010), 3045–3067. DOI: 10.1103/revmodphys.82.3045.
- [165] X.-L. Qi and S.-C. Zhang. “Topological insulators and superconductors”. *Reviews of Modern Physics* **83** (2011), 1057–1110. DOI: 10.1103/revmodphys.83.1057.
- [166] P. Coleman. “Heavy Fermions: electrons at the edge of magnetism”. *Handbook of Magnetism and Advanced Magnetic Materials. Edited by Helmut Kronmuller and Stuart Parkin. Vol 1: Fundamentals and Theory. John Wiley and Sons, 95-148 (2007).* (2006).
- [167] M. Dzero, K. Sun, V. Galitski and P. Coleman. “Topological Kondo Insulators”. *Physical Review Letters* **104** (2010), 106408. DOI: 10.1103/physrevlett.104.106408.
- [168] D. J. Kim, T. Grant and Z. Fisk. “Limit Cycle and Anomalous Capacitance in the Kondo Insulator SmB<sub>6</sub>”. *Physical Review Letters* **109** (2012), 096601. DOI: 10.1103/physrevlett.109.096601.

## Bibliography

---

- [169] X. Zhang, N. P. Butch, P. Syers, S. Ziemak, R. L. Greene and J. Paglione. “Hybridization, Inter-Ion Correlation, and Surface States in the Kondo Insulator  $\text{SmB}_6$ ”. *Physical Review X* **3** (2013), 011011. DOI: 10.1103/physrevx.3.011011.
- [170] S. Wolgast, Ç. Kurdak, K. Sun, J. W. Allen, D.-J. Kim and Z. Fisk. “Low-temperature surface conduction in the Kondo insulator  $\text{SmB}_6$ ”. *Physical Review B* **88** (2013), 180405. DOI: 10.1103/physrevb.88.180405.
- [171] D. J. Kim, S. Thomas, T. Grant, J. Botimer, Z. Fisk and J. Xia. “Surface Hall Effect and Nonlocal Transport in  $\text{SmB}_6$ : Evidence for Surface Conduction”. *Scientific Reports* **3** (2013), 3150. DOI: 10.1038/srep03150.
- [172] W. A. Phelan, S. M. Koochpayeh, P. Cottingham, J. W. Freeland, J. C. Leiner, C. L. Broholm and T. M. McQueen. “Correlation between Bulk Thermodynamic Measurements and the Low-Temperature-Resistance Plateau in  $\text{SmB}_6$ ”. *Physical Review X* **4** (2014), 031012. DOI: 10.1103/physrevx.4.031012.
- [173] F. Chen, C. Shang, Z. Jin, D. Zhao, Y. P. Wu, Z. J. Xiang, Z. C. Xia, A. F. Wang, X. G. Luo, T. Wu and X. H. Chen. “Magnetoresistance evidence of a surface state and a field-dependent insulating state in the Kondo insulator  $\text{SmB}_6$ ”. *Physical Review B* **91** (2015), 205133. DOI: 10.1103/physrevb.91.205133.
- [174] P. Syers, D. Kim, M. S. Fuhrer and J. Paglione. “Tuning Bulk and Surface Conduction in the Proposed Topological Kondo Insulator  $\text{SmB}_6$ ”. *Physical Review Letters* **114** (2015), 096601. DOI: 10.1103/physrevlett.114.096601.
- [175] S. Wolgast, Y. S. Eo, T. Öztürk, G. Li, Z. Xiang, C. Tinsman, T. Asaba, B. Lawson, F. Yu, J. W. Allen, K. Sun, L. Li, Ç. Kurdak, D.-J. Kim and Z. Fisk. “Magnetotransport measurements of the surface states of samarium hexaboride using Corbino structures”. *Physical Review B* **92** (2015), 115110. DOI: 10.1103/physrevb.92.115110.
- [176] M. Neupane, N. Alidoust, S.-Y. Xu, T. Kondo, Y. Ishida, D. J. Kim, C. Liu, I. Belopolski, Y. J. Jo, T.-R. Chang, H.-T. Jeng, T. Durakiewicz, L. Balicas, H. Lin, A. Bansil, S. Shin, Z. Fisk and M. Z. Hasan. “Surface electronic structure of the topological Kondo-insulator candidate correlated electron system  $\text{SmB}_6$ ”. *Nature Communications* **4** (2013), 2991. DOI: 10.1038/ncomms3991.
- [177] F. Lu, J. Zhao, H. Weng, Z. Fang and X. Dai. “Correlated Topological Insulators with Mixed Valence”. *Physical Review Letters* **110** (2013), 096401. DOI: 10.1103/physrevlett.110.096401.

- 
- [178] N. Xu, X. Shi, P. K. Biswas, C. E. Matt, R. S. Dhaka, Y. Huang, N. C. Plumb, M. Radović, J. H. Dil, E. Pomjakushina, K. Conder, A. Amato, Z. Salman, D. M. Paul, J. Mesot, H. Ding and M. Shi. “Surface and bulk electronic structure of the strongly correlated system  $\text{SmB}_6$  and implications for a topological Kondo insulator”. *Physical Review B* **88** (2013), 121102. DOI: 10.1103/physrevb.88.121102.
- [179] Z.-H. Zhu, A. Nicolaou, G. Levy, N. P. Butch, P. Syers, X. F. Wang, J. Paglione, G. A. Sawatzky, I. S. Elfimov and A. Damascelli. “Polarity-Driven Surface Metallicity in  $\text{SmB}_6$ ”. *Physical Review Letters* **111** (2013), 216402. DOI: 10.1103/physrevlett.111.216402.
- [180] N. Xu, P. K. Biswas, J. H. Dil, R. S. Dhaka, G. Landolt, S. Muff, C. E. Matt, X. Shi, N. C. Plumb, M. Radović, E. Pomjakushina, K. Conder, A. Amato, S. V. Borisenko, R. Yu, H.-M. Weng, Z. Fang, X. Dai, J. Mesot, H. Ding and M. Shi. “Direct observation of the spin texture in  $\text{SmB}_6$  as evidence of the topological Kondo insulator”. *Nature Communications* **5** (2014), 4566. DOI: 10.1038/ncomms5566.
- [181] G. Li, Z. Xiang, F. Yu, T. Asaba, B. Lawson, P. Cai, C. Tinsman, A. Berkley, S. Wolgast, Y. S. Eo, D.-J. Kim, C. Kurdak, J. W. Allen, K. Sun, X. H. Chen, Y. Y. Wang, Z. Fisk and L. Li. “Two-dimensional Fermi surfaces in Kondo insulator  $\text{SmB}_6$ ”. *Science* **346** (2014), 1208–1212. DOI: 10.1126/science.1250366.
- [182] P. Hlawenka, K. Siemensmeyer, E. Weschke, A. Varykhalov, J. Sánchez-Barriga, N. Y. Shitsevalova, A. V. Dukhnenko, V. B. Filipov, S. Gabáni, K. Flachbart, O. Rader and E. D. L. Rienks. “Samarium hexaboride is a trivial surface conductor”. *Nature Communications* **9** (2018), 517. DOI: 10.1038/s41467-018-02908-7.
- [183] B. S. Tan, Y.-T. Hsu, B. Zeng, M. C. Hatnean, N. Harrison, Z. Zhu, M. Hartstein, M. Kiourlappou, A. Srivastava, M. D. Johannes, T. P. Murphy, J.-H. Park, L. Balicas, G. G. Lonzarich, G. Balakrishnan and S. E. Sebastian. “Unconventional Fermi surface in an insulating state”. *Science* **349** (2015), 287–290. DOI: 10.1126/science.aaa7974.
- [184] O. Erten, P.-Y. Chang, P. Coleman and A. M. Tsvelik. “Skyrme Insulators: Insulators at the Brink of Superconductivity”. *Physical Review Letters* **119** (2017), 057603. DOI: 10.1103/physrevlett.119.057603.

## Bibliography

---

- [185] M. Kasaya, F. Iga, K. Negishi, S. Nakai and T. Kasuya. “A new and typical valence fluctuating system,  $\text{YbB}_{12}$ ”. *Journal of Magnetism and Magnetic Materials* **31-34** (1983), 437–438. DOI: 10.1016/0304-8853(83)90312-8.
- [186] G. P. Meisner, M. S. Torikachvili, K. N. Yang, M. B. Maple and R. P. Guertin. “ $\text{UFe}_4\text{P}_{12}$  and  $\text{CeFe}_4\text{P}_{12}$ : Nonmetallic isotypes of superconducting  $\text{LaFe}_4\text{P}_{12}$ ”. *Journal of Applied Physics* **57** (1985), 3073–3075. DOI: 10.1063/1.335217.
- [187] M. F. Hundley, P. C. Canfield, J. D. Thompson, Z. Fisk and J. M. Lawrence. “Hybridization gap in  $\text{Ce}_3\text{Bi}_4\text{Pt}_3$ ”. *Physical Review B* **42** (1990), 6842–6845. DOI: 10.1103/physrevb.42.6842.
- [188] T. Takabatake, F. Teshima, H. Fujii, S. Nishigori, T. Suzuki, T. Fujita, Y. Yamaguchi, J. Sakurai and D. Jaccard. “Formation of an anisotropic energy gap in the valence-fluctuating system of  $\text{CeNiSn}$ ”. *Physical Review B* **41** (1990), 9607–9610. DOI: 10.1103/physrevb.41.9607.
- [189] T. E. Mason, G. Aeppli, A. P. Ramirez, K. N. Clausen, C. Broholm, N. Stücheli, E. Bucher and T. T. M. Palstra. “Spin gap and antiferromagnetic correlations in the Kondo insulator  $\text{CeNiSn}$ ”. *Physical Review Letters* **69** (1992), 490–493. DOI: 10.1103/physrevlett.69.490.
- [190] S. Takagi, H. Yasuoka, S. Ogawa and J. H. Wernick. “ $^{29}\text{Si}$  NMR Studies of an “Unusual” Paramagnet  $\text{FeSi}$  - Anderson Localized State Model -”. *Journal of the Physical Society of Japan* **50** (1981), 2539–2546. DOI: 10.1143/jpsj.50.2539.
- [191] Z. Schlesinger, Z. Fisk, H.-T. Zhang, M. B. Maple, J. DiTusa and G. Aeppli. “Unconventional charge gap formation in  $\text{FeSi}$ ”. *Physical Review Letters* **71** (1993), 1748–1751. DOI: 10.1103/physrevlett.71.1748.
- [192] M. B. Hunt, M. A. Chernikov, E. Felder, H. R. Ott, Z. Fisk and P. Canfield. “Low-temperature magnetic, thermal, and transport properties of  $\text{FeSi}$ ”. *Physical Review B* **50** (1994), 14933–14941. DOI: 10.1103/physrevb.50.14933.
- [193] J. F. DiTusa, K. Friemelt, E. Bucher, G. Aeppli and A. P. Ramirez. “Metal-Insulator Transitions in the Kondo Insulator  $\text{FeSi}$  and Classic Semiconductors Are Similar”. *Physical Review Letters* **78** (1997), 2831–2834. DOI: 10.1103/physrevlett.78.2831.

- 
- [194] S. Paschen, E. Felder, M. A. Chernikov, L. Degiorgi, H. Schwer, H. R. Ott, D. P. Young, J. L. Sarrao and Z. Fisk. “Low-temperature transport, thermodynamic, and optical properties of FeSi”. *Physical Review B* **56** (1997), 12916–12930. DOI: 10.1103/physrevb.56.12916.
- [195] N. E. Sluchanko, V. V. Glushkov, S. V. Demishev, M. V. Kondrin, V. Y. Ivanov, K. M. Petukhov, N. A. Samarin, A. A. Menovsky and V. V. Moshchalkov. “Ground state formation in a strong hubbard correlation regime in iron monosilicide”. *Journal of Experimental and Theoretical Physics* **92** (2001), 312–325. DOI: 10.1134/1.1354689.
- [196] N. E. Sluchanko, V. V. Glushkov, S. V. Demishev, A. A. Menovsky, L. Weckhuyssen and V. V. Moshchalkov. “Crossover in magnetic properties of FeSi”. *Physical Review B* **65** (2002), 064404. DOI: 10.1103/physrevb.65.064404.
- [197] J. M. Tomczak, K. Haule and G. Kotliar. “Signatures of electronic correlations in iron silicide”. *Proceedings of the National Academy of Sciences* **109** (2012), 3243–3246. DOI: 10.1073/pnas.1118371109.
- [198] R. Ritz, M. Halder, C. Franz, A. Bauer, M. Wagner, R. Bamler, A. Rosch and C. Pfleiderer. “Giant generic topological Hall resistivity of MnSi under pressure”. *Physical Review B* **87** (2013), 134424. DOI: 10.1103/physrevb.87.134424.
- [199] P. Lunkenheimer, G. Knebel, R. Viana and A. Loidl. “Hopping conductivity in FeSi”. *Solid State Communications* **93** (1995), 891–895. DOI: 10.1016/0038-1098(94)00895-7.
- [200] L. Degiorgi, M. Hunt, H. Ott and Z. Fisk. “Transport and optical properties of FeSi”. *Physica B: Condensed Matter* **206-207** (1995), 810–812. DOI: 10.1016/0921-4526(94)00592-j.
- [201] G. Phragmen. “Om järn-kisellegeringarnas byggnad”. *Jernkontorets Annaler* **107** (1923), 121–131.
- [202] P. Villars and L. Calvert. *Pearson’s Handbook of Crystallographic Data for Intermetallic Phases*. American Society for Metals, 1985.
- [203] L. Pauling and A. M. Soldate. “The nature of the bonds in the iron silicide, FeSi, and related crystals”. *Acta Crystallographica* **1** (1948), 212–216. DOI: 10.1107/s0365110x48000570.

## Bibliography

---

- [204] K. Momma and F. Izumi. “VESTA3 for three-dimensional visualization of crystal, volumetric and morphology data”. *Journal of Applied Crystallography* **44** (2011), 1272–1276. DOI: 10.1107/s0021889811038970.
- [205] H. Watanabe, H. Yamamoto and K.-i. Ito. “Neutron Diffraction Study of the Intermetallic Compound FeSi”. *Journal of the Physical Society of Japan* **18** (1963), 995–999. DOI: 10.1143/jpsj.18.995.
- [206] M. Krajčí and J. Hafner. “Surfaces of intermetallic compounds: An ab initio DFT study for B20-type AlPd”. *Physical Review B* **87** (2013), 035436. DOI: 10.1103/physrevb.87.035436.
- [207] M. Armbrüster, H. Borrmann, M. Wedel, Y. Prots, R. Giedigkeit and P. Gille. “Refinement of the crystal structure of palladium gallium (1:1), PdGa”. *Zeitschrift für Kristallographie - New Crystal Structures* **225** (2010). DOI: 10.1524/ncrs.2010.0269.
- [208] J. Kübler, B. Yan and C. Felser. “Non-vanishing Berry phase in chiral insulators”. *Europhysics Letters* **104** (2013), 30001. DOI: 10.1209/0295-5075/104/30001.
- [209] A. Neubauer, J. Boeuf, A. Bauer, B. Russ, H. v. Löhneysen and C. Pfleiderer. “Ultra-high vacuum compatible image furnace”. *Review of Scientific Instruments* **82** (2011), 013902. DOI: 10.1063/1.3523056.
- [210] M. Klein, D. Menzel, K. Doll, M. Neef, D. Zur, I. Jursic, J. Schoenes and F. Reinert. “Photoemission spectroscopy across the semiconductor-to-metal transition in FeSi”. *New Journal of Physics* **11** (2009), 023026. DOI: 10.1088/1367-2630/11/2/023026.
- [211] L. Vočadlo, K. S. Knight, G. D. Price and I. G. Wood. “Thermal expansion and crystal structure of FeSi between 4 and 1173 K determined by time-of-flight neutron powder diffraction”. *Physics and Chemistry of Minerals* **29** (2002), 132–139. DOI: 10.1007/s002690100202.
- [212] D. Rosenthal, R. Widmer, R. Wagner, P. Gille, M. Armbrüster, Y. Grin, R. Schlögl and O. Gröning. “Surface Investigation of Intermetallic PdGa(III)”. *Langmuir* **28** (2012), 6848–6856. DOI: 10.1021/la2050509.
- [213] J. Hafner and M. Krajčí. “Surfaces of Complex Intermetallic Compounds: Insights from Density Functional Calculations”. *Accounts of Chemical Research* **47** (2014), 3378–3384. DOI: 10.1021/ar500043z.

- 
- [214] M. Schmid, H. Stadler and P. Varga. “Direct observation of surface chemical order by scanning tunneling microscopy”. *Phys. Rev. Lett.* **70** (10 1993), 1441–1444. DOI: 10.1103/PhysRevLett.70.1441.
- [215] P. Hohenberg and W. Kohn. “Inhomogeneous Electron Gas”. *Physical Review* **136** (1964), B864–B871. DOI: 10.1103/physrev.136.b864.
- [216] W. Kohn and L. J. Sham. “Self-Consistent Equations Including Exchange and Correlation Effects”. *Physical Review* **140** (1965), A1133–A1138. DOI: 10.1103/physrev.140.a1133.
- [217] P. Giannozzi *et al.* “QUANTUM ESPRESSO: a modular and open-source software project for quantum simulations of materials”. *Journal of Physics: Condensed Matter* **21** (2009), 395502. DOI: 10.1088/0953-8984/21/39/395502.
- [218] F. Reinert, G. Nicolay, S. Schmidt, D. Ehm and S. Hüfner. “Direct measurements of the L-gap surface states on the (111) face of noble metals by photoelectron spectroscopy”. *Physical Review B* **63** (2001), 115415. DOI: 10.1103/physrevb.63.115415.
- [219] J. Li, W.-D. Schneider and R. Berndt. “Local density of states from spectroscopic scanning-tunneling-microscope images: Ag(111)”. *Physical Review B* **56** (1997), 7656–7659. DOI: 10.1103/PhysRevB.56.7656.
- [220] L. Limot, E. Pehlke, J. Kröger and R. Berndt. “Surface-State Localization at Adatoms”. *Physical Review Letters* **94** (2005), 036805. DOI: 10.1103/PhysRevLett.94.036805.
- [221] U. Fano. “Effects of Configuration Interaction on Intensities and Phase Shifts”. *Physical Review* **124** (1961), 1866–1878. DOI: 10.1103/physrev.124.1866.
- [222] K. Breuer, S. Messerli, D. Purdie, M. Garnier, M. Hengsberger, Y. Baer and M. Mihalik. “Observation of a gap opening in FeSi with photoelectron spectroscopy”. *Physical Review B* **56** (1997), R7061–R7064. DOI: 10.1103/physrevb.56.r7061.
- [223] T. Susaki, T. Mizokawa, A. Fujimori, A. Ohno, T. Tonogai and H. Takagi. “Temperature and substitution dependence of the photoemission spectra of FeSi”. *Physical Review B* **58** (1998), 1197–1200. DOI: 10.1103/physrevb.58.1197.

## Bibliography

---

- [224] K. Ishizaka, T. Kiss, T. Shimojima, T. Yokoya, T. Togashi, S. Watanabe, C. Q. Zhang, C. T. Chen, Y. Onose, Y. Tokura and S. Shin. “Ultraviolet laser photoemission spectroscopy of FeSi: Observation of a gap opening in density of states”. *Physical Review B* **72** (2005), 233202. DOI: 10.1103/physrevb.72.233202.
- [225] J. Aarts and A. Volodin. “Tunneling spectroscopy on correlated electron systems”. *Physica B: Condensed Matter* **206-207** (1995), 43–48. DOI: 10.1016/0921-4526(94)00363-z.
- [226] M. Fäth, J. Aarts, A. A. Menovsky, G. J. Nieuwenhuys and J. A. Mydosh. “Tunneling spectroscopy on the correlation effects in FeSi”. *Physical Review B* **58** (1998), 15483–15490. DOI: 10.1103/physrevb.58.15483.
- [227] A. Lacerda, H. Zhang, P. Canfield, M. Hundley, Z. Fisk, J. Thompson, C. Seaman, M. Maple and G. Aeppli. “Narrow-gap signature of Fe<sub>x</sub>Co<sub>1-x</sub>Si single crystals”. *Physica B: Condensed Matter* **186-188** (1993), 1043–1045. DOI: 10.1016/0921-4526(93)90780-a.
- [228] P. Samuely, P. Szabó, M. Mihalik, N. Hudáková and A. Menovsky. “Gap formation in Kondo insulator FeSi: Point contact spectroscopy”. *Physica B: Condensed Matter* **218** (1996), 185–188. DOI: 10.1016/0921-4526(95)00589-7.
- [229] B. C. Sales, E. C. Jones, B. C. Chakoumakos, J. A. Fernandez-Baca, H. E. Harmon, J. W. Sharp and E. H. Volckmann. “Magnetic, transport, and structural properties of Fe<sub>1-x</sub>IrxSi”. *Physical Review B* **50** (1994), 8207–8213. DOI: 10.1103/physrevb.50.8207.
- [230] A. Damascelli, K. Schulte, D. van der Marel and A. A. Menovsky. “Infrared spectroscopic study of phonons coupled to charge excitations in FeSi”. *Physical Review B* **55** (1997), R4863–R4866. DOI: 10.1103/physrevb.55.r4863.
- [231] M. Bat’ková, I. Bat’ko and M. Mihalik. “Evidence for direct and indirect gap in FeSi from electron tunneling spectroscopy”. *Solid State Communications* **141** (2007), 412–415. DOI: 10.1016/j.ssc.2006.11.014.
- [232] Y. Fang, S. Ran, W. Xie and M. B. Maple. “Observation of transition from semiconducting to metallic ground state in high-quality single crystalline FeSi”. *ArXiv e-prints* (2018), arXiv:1804.02036.
- [233] L. F. Mattheiss and D. R. Hamann. “Band structure and semiconducting properties of FeSi”. *Physical Review B* **47** (1993), 13114–13119. DOI: 10.1103/physrevb.47.13114.



- 
- [234] V. Madhavan. “Tunneling into a Single Magnetic Atom: Spectroscopic Evidence of the Kondo Resonance”. *Science* **280** (1998), 567–569. DOI: 10.1126/science.280.5363.567.
- [235] S. Rößler, T.-H. Jang, D.-J. Kim, L. H. Tjeng, Z. Fisk, F. Steglich and S. Wirth. “Hybridization gap and Fano resonance in SmB<sub>6</sub>”. *Proceedings of the National Academy of Sciences* **111** (2014), 4798–4802. DOI: 10.1073/pnas.1402643111.
- [236] V. V. Glushkov, B. P. Gorshunov, E. S. Zhukova, S. V. Demishev, A. A. Pronin, N. E. Sluchanko, S. Kaiser and M. Dressel. “Spin excitations of the correlated semiconductor FeSi probed by THz radiation”. *Physical Review B* **84** (2011), 073108. DOI: 10.1103/physrevb.84.073108.
- [237] S. Khmelevskiy, G. Kresse and P. Mohn. “Correlated excited states in the narrow band gap semiconductor FeSi and antiferromagnetic screening of local spin moments”. *Physical Review B* **98** (2018), 125205. DOI: 10.1103/physrevb.98.125205.
- [238] C. Ophus, J. Ciston and C. T. Nelson. “Correcting nonlinear drift distortion of scanning probe and scanning transmission electron microscopies from image pairs with orthogonal scan directions”. *Ultramicroscopy* **162** (2016), 1–9. DOI: 10.1016/j.ultramic.2015.12.002.



## List of Publications

- A. Timmer, H. Mönig, M. Uphoff, O. D. Arado, S. Amirjalayer and H. Fuchs. “Site-Specific Adsorption of Aromatic Molecules on a Metal/Metal Oxide Phase Boundary”. *Nano Letters* **18** (2018), 4123–4129. DOI: 10.1021/acs.nanolett.8b00855.
- M. Uphoff, G. S. Michelitsch, R. Hellwig, K. Reuter, H. Brune, F. Klappenberger and J. V. Barth. “Assembly of Robust Holmium-Directed 2D Metal–Organic Coordination Complexes and Networks on the Ag(100) Surface”. *ACS Nano* **12** (2018), 11552–11560. DOI: 10.1021/acsnano.8b06704.
- F. Klappenberger, R. Hellwig, P. Du, T. Paintner, M. Uphoff, L. Zhang, T. Lin, B. A. Moghanaki, M. Paszkiewicz, I. Vobornik, J. Fujii, O. Fuhr, Y.-Q. Zhang, F. Allegretti, M. Ruben and J. V. Barth. “Functionalized Graphdiyne Nanowires: On-Surface Synthesis and Assessment of Band Structure, Flexibility, and Information Storage Potential”. *Small* **14** (2018), 1704321. DOI: 10.1002/smll.201704321.
- R. Hellwig, M. Uphoff, T. Paintner, J. Björk, M. Ruben, F. Klappenberger and J. V. Barth. “Ho-Mediated alkyne reactions at low temperatures on Ag(111)”. *Chemistry - A European Journal* **24** (2018), 16126–16135. DOI: 10.1002/chem.201803102.
- T. Paintner, J. Björk, P. Du, S. Klyatskaya, M. Paszkiewicz, R. Hellwig, M. Uphoff, M. A. Öner, E. Cuniberto, P. S. Deimel, Y.-Q. Zhang, C.-A. Palma, F. Allegretti, M. Ruben, J. V. Barth and F. Klappenberger. “Quantum Tunneling-Mediated Interfacial Synthesis of a Benzofuran Derivative”. *Angewandte Chemie International Edition* (2019). DOI: 10.1002/anie.201904030.



# Acknowledgements

This work was made possible by a lot of different people, so I would like to express my gratitude towards them. First of all I would like to thank my supervisor Prof. Johannes V. Barth, for giving me the opportunity to work as a PhD candidate at his chair, as well as his expert scientific guidance he provided throughout the project. Secondly, I would like to thank Dr. Florian Klappenberger for his supervision and the refreshing scientific discussions on our projects. He guided me especially at the start of my PhD project. He was always offering expert advice on scientific writing and showed me a lot in that field. The high degree of independence entrusted to me by Johannes and Florian made the research at E20 a delightful experience. I also want to thank Prof. Harald Brune from the EPFL in Lausanne for his guiding and scientific support with the Ho-TPA project.

Next, I want to express my gratitude to Prof. Peter Feulner, whose seemingly fathomless depth of knowledge in the field of physics and electrical engineering made tricky problems disappear for a lot of times. His help with the development of new components for the UHV system and the intriguing scientific discussions are priceless. Also, I would like to thank our technician Karl Eberle, who made everyday life a lot easier with his decades of expertise, always offering his help whenever it was needed. The same accounts for our electronics engineer Reinhold Schneider, whose magic at the soldering station saved us a lot of times. Last but not least, I would like to thank our secretary Viktoria Blaschek, who was always helpful. It makes all the difference to have administrative support like Viktoria provides it.

I also want to thank Dr. Yiqi Zhang and Dr. Biao Yang, who worked on the iron silicide project with me. Special thanks to Yiqi and Dr. Joachim Reichert for looking through the manuscript and giving me advice. I also thank my former fellow PhD students Dr. Raphael Hellwig and Dr. Tobias Paintner who ran the JT lab together with me and always helped out. I would also like to thank Dr. Knud Seufert and Dr. Alexander Riss from the Auwärter group who always lent an ear whenever cracking some scientific nuts. I thank Dr. Hartmut Schlichting and Andreas Walz for their advice and help on technical problems of all sorts. I also want to thank Alexander Timmer from my old work group in

## Acknowledgements

---

Münster for giving me suggestions on my thesis.

An experimentalist needs his theoretician, so I would give special thanks to two people here. First to Dr. Georg S. Michelitsch who did the calculations for the Ho-TPA structures on Ag(100) and to Dr. Ari P. Seitsonen, who stepped in on short notice and gave crucial computational input to the FeSi project.

General thanks goes to all the E20 staff, especially Mathias Pörtner, Andreas Walz, Dr. Tobias Paintner, Dr. Jacob Ducke, Sabine Synkule and Dr. Peter Deimel. They played a significant role in making my time at E20 a thrilling experience. This involves scientific communication as well as the multitude of social activities we did in the group. Special thanks to Dr. Peter Deimel and Dr. Ignacio Piquero-Zulaica for proof reading my thesis.

I want to express my biggest gratitude towards my family. They always supported me in pursuing my academic pathway and helped me out whenever problems occurred. And finally I want to thank my girlfriend Esther for her never ending support, always standing by my side whenever times were tough.